Turbulent channel flow with stable stratification beyond the Oberbeck-Boussinesq assumptions

A DNS study

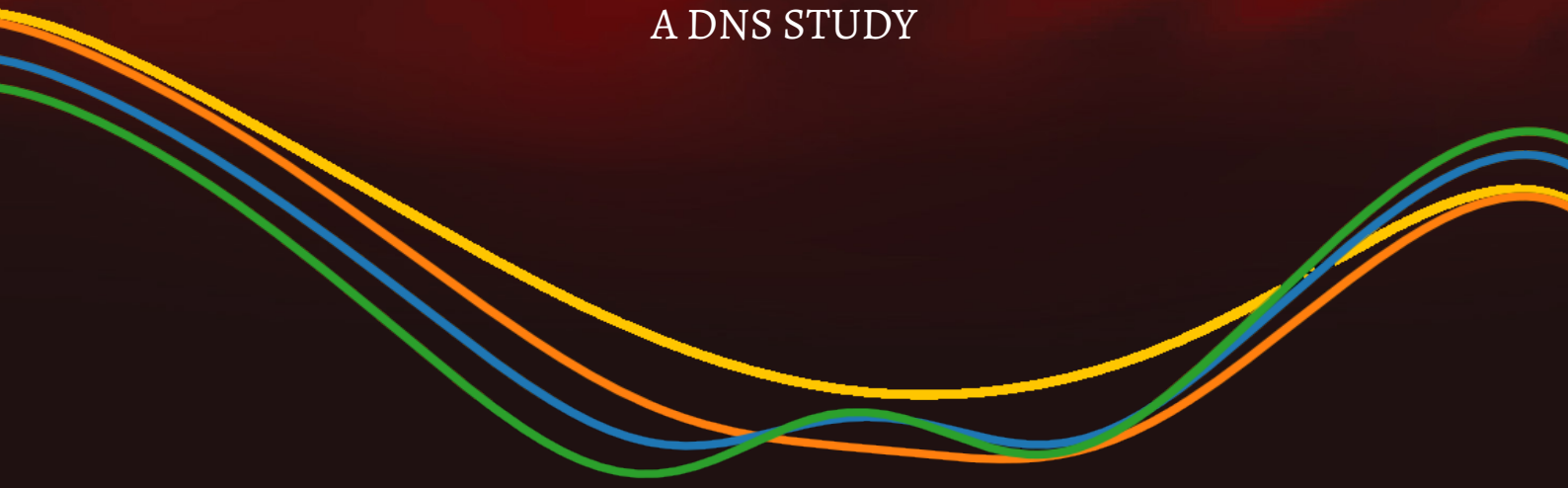

SANATH K.

Supervisors: Prof. Rene Pecnik | Dr. Pedro Costa

TU Delft

Turbulent channel flow with stable stratification beyond the Oberbeck-Boussinesq assumptions

A DNS study

by

Sanath Kottursheṭtar

to obtain the degree of Master of Science

at the Delft University of Technology,

to be defended publicly on Thursday, July 27, 2023, at 15:00 hrs.

Student number:	5218136	
Project duration:	October 6, 2022 - July 27, 2023	
Thesis committee:	Prof. dr. Rene Pecnik,	TU Delft, supervisor
	Dr. Pedro Costa,	TU Delft, supervisor
	Dr. Ir. Jurriaan Peeters,	TU Delft, committee member
	Prof. dr. Gabriel Weymouth,	TU Delft, committee member

This thesis is confidential and cannot be made public until July 27, 2023.

TU Delft

M. Sc. Thesis

Turbulent channel flow with stable stratification beyond the Oberbeck-Boussinesq assumptions

Energy, Process and Flow Technology- 3ME
TU Delft

Sanath K.

July 21, 2023

Abstract

Stratified turbulent flows abound in environmental and industrial settings. Examples are atmospheric boundary layer flows, the transport of nutrients and organisms and the mixing of heat and salinity in the oceans, fluid flow in heat exchangers, and the transport of reactants and products in chemical reactions. These examples and many others consider stratified wall-bounded turbulence, in which the creation of turbulence by mechanical processes contends with its dissipation due to buoyancy effects. These flows are said to be stably stratified as these are inherently stable flows and are averse to mixing. The buoyancy effects alter the structure of the flow, and consequently the dynamics of mass, heat, and momentum transport. As density fluctuations become more severe, the Oberbeck-Boussinesq approximation becomes inaccurate and the resulting dynamics are not correctly predicted. In the current work, we developed and validated a numerical solver for direct numerical simulations (DNS) of turbulent flows featuring strong property variations. More precisely, we solve the Navier-Stokes equations in the limit of vanishing Mach number (so-called low-Mach number limit), with the fluid density given by the ideal gas law, and the dynamic viscosity and thermal conductivity also expressed as functions of temperature.

Our numerical solver is used to study stably-stratified turbulent channel flow under non-Oberbeck-Boussinesq conditions. A comparison between the available studies to the current study is shown in the table below.

	$\rho(T), \mu(T), \lambda(T)$	$\mu(T), \beta(T)$
$Ri_\tau = 0$	Patel et al. (2015),	Zonta et al. (2012a)
$Ri_\tau > 0$	Current Work	Zonta et al. (2012b)

Table 1: Description of the research gap the current work aims to fill.

The simulations are carried out at $Re_\tau = 180$, $Pr = 0.71$ and $Ri_\tau = \mathcal{O}(10)$, where Re_τ, Pr and Ri_τ are governing parameters (specifically, the friction Reynolds, Prandtl, and friction Richardson numbers) defined based on the prescribed pressure drop and properties of the fluid at the reference temperature. Stratification is achieved by imposing constant temperature boundary conditions, with a high upper-to-lower wall temperature ratio (larger than 2), resulting in strong density variations in the flow. We will vary the temperature ratios and adjust gravity to maintain a similar Richardson number between cases, thereby isolating the effects of strong property variations in the flow dynamics. We will analyze the dynamics of heat and momentum transport under strong stratification for these conditions, also in light of DNS data of the same system under the Oberbeck-Boussinesq regime.

Acknowledgements

My two years at TU Delft, it's been like going skydiving for the first time. You know what's coming, so you are terrified yet excited before taking the leap, adapting and calming yourself during the fall, and feeling a myriad of emotions as the feet slowly regain control on the ground. I am living the final part of this beautiful experience as I write this section of my thesis. And of the countless emotions, the most overwhelming one is the feeling of gratitude. It's humbling to sit down and think of the people that you are indebted when you finish a journey like this. So, in the next few paragraphs, there will be no numbers or equations or citations, just words expressing my heartfelt gratitude to all the people who propelled me through this adventure.

I would like to thank my supervisors, Prof.dr. Rene Pecnik and Dr. Pedro Costa, for their invaluable input over the course of the thesis. Prof.dr. Rene Pecnik was ever-willing to engage with me in discussions. His curiosity and passion for research inspired me to work earnestly and persistently in the pursuit to find answers to all kinds of questions. His guidance and feedback have been instrumental over the past nine months and I am grateful for his contribution to my academic and personal growth. I am not only incredibly fortunate to have had Dr. Pedro Costa as my co-supervisor but also incredibly grateful to him. He was ever so patient and kind despite my innumerable consultations. He has been actively involved since running my first DNS cases, to analyzing the last set of results. His humility, optimism, and cheerfulness are all qualities I would love to imbibe in my life. I thank both of my supervisors for trusting me to deliver on this project and shaping the direction of this work.

I am also grateful to the entire research group of Prof.dr. Rene Pecnik for being inclined to hear me out when called upon and provide useful feedback. I am thankful to TU Delft, the faculty members of Process and Energy, and all my teachers for the lectures, assignments, and discussions that not only helped me understand the topics better but also made me more reflective and rational. And a special thanks to the DelftBlue High-Performance Computing Centre for providing me with the resources to work on this thesis.

I am extremely grateful to the wonderful group of peers who contributed significantly during my time at Delft. To you guys - thank you for accepting me in your lives, for cooking some great food, for the discussions - regardless of them being insightful or futile, and most of all thank you for being my friends. I wish only the best for every one of you and cannot wait to witness you all become the finest and the most amazing versions of yourselves in the coming years.

I also have to mention my friends from back home because, one, I don't think life would have been this fun without them, and two, this section would be incomplete otherwise. It's astonishing how time passes by when you are having fun.

And finally, I am indebted to the ones that are the dearest in my life. To my parents, sister, and the entire family back home - Thank you for everything. I cannot thank you enough for not just letting me live my life on my terms but also supporting and encouraging it. I owe everything that I am today to the people at home who raised me and am grateful for all the values, good-bad-ugly, instilled in me. And finally finally, to my grandfather, I know he would have been immensely happy with not just this piece of report but my journey as a whole. I've always wanted to be half as hard-working as he was and hope to get there one day.

When there's all this help around, even the teeniest bit of effort is enough to get things right. And the thesis is a byproduct of that effort.

Delft University of Technology
July 2023

Sanath

Contents

List of Tables **V**

List of Figures **VII**

1 Introduction **1**

1.1 Outline 2

2 Literature Review **3**

2.1 Length scales 3

2.2 Wall-bounded stratified turbulent flows 4

2.3 Oberbeck-Boussinesq approximation 5

2.3.1 Numerical studies 6

2.4 Non-Oberbeck Boussinesq effects 8

2.5 Internal gravity waves (IGW) 10

2.6 Influence of stratification on macroscopic heat and momentum transfer rates 10

2.7 Discussion 12

3 Objective and Scope of Thesis **13**

4 Governing Equations **14**

4.1 Low-Mach number approximation 14

4.2 Governing equations 15

4.2.1 Thermophysical properties 16

5 Implementation **18**

5.1 Discretization schemes 18

5.2 Pressure-splitting 20
5.3 Validation 21

6 Numerical Simulations **25**

6.1 Computational details 25
6.2 Cases 26
6.3 Transient evolution of the flow 27

7 Results **30**

7.1 Qualitative description of the flow 30
7.2 Fluid velocity and temperature statistics 31
7.2.1 Case A vs. Case B 36
7.2.2 Comparison between cases B0, B1, B2 and B3 46
7.3 Internal gravity waves 50
7.3.1 Buoyancy frequency 51
7.4 Macroscopic quantities of the flow 56
7.5 Mean kinetic energy 57
7.6 Spanwise vorticity 58

8 Conclusion **63**

9 Discussion **65**

A Low-Mach Number Equations **67**

A.1 Derivation of the low-Mach approximation 67
A.2 Derivation of the rate of change of thermodynamic pressure and divergence of velocity 68

B WENO Scheme **71**

C Derivation of MKE and TKE Equations **73**

D Comparison of Case C with Cases A and B **75**

List of Tables

1 Description of the research gap the current work aims to fill. I

5.1 Validation of macroscopic quantities obtained in the present code with Nicoud (2000). 24

6.1 Macroscopic quantities obtained from the simulations for different cases. 27

6.2 Mesh details with respect to the viscous length scale at both walls. 28

7.1 The distance of the zero stress plane from the cold wall in turbulent channel flows for $Ri_\tau = 0,\ 18,\ 36,\ 60$ at $T_2/T_1 = 1.01$ and $T_2/T_1 = 2$. 43

7.2 Comparison of the effect of stratification on macroscopic quantities for the constant property flow. 56

7.3 Comparison of the effect of stratification on macroscopic quantities for the variable property flow. 56

7.4 Comparison of the macroscopic quantities for the constant and variable property flow at a given Richardson number. 57

List of Figures

2.1 Variation of Ozmidov and Kolmogorov length scales with respect to the length scale of large eddies in wall-normal direction. 5

2.2 A parameter space $(\Delta T, h)$ of wall-bounded stratified turbulence with the different numerical approach that can be used for its description. 6

2.3 A parameter space (Re_τ, Ri_τ) of wall-bounded stratified turbulence depicting the current state of research. 7

2.4 The structure of wall-bounded stably stratified turbulence. 10

2.5 Contours of instantaneous fluctuations of density and wall-normal velocity. 11

2.6 Variation of friction factor and Nusselt number with Ri_τ. 11

5.1 Validation of DNS results obtained using the numerical method described in the present work with Franck (1998) for the case $T_2/T_1 = 1.01$. 22

5.2 Validation of DNS results obtained using the numerical method described in the present work with Franck (1998) for the case $T_2/T_1 = 2$. 23

5.3 Validation of DNS results obtained using the numerical method described in the present work with Nicoud (2000) for the case $T_2/T_1 = 2,\ 4$. 24

6.1 Computational domain for the present work. 26

6.2 Evolution of mean velocity with time for different Richardson numbers for Case B. 28

7.1 Instantaneous temperature contours on $x - z$ cross-section of the channel located at $y = L_y/2$ 32

7.2 Instantaneous temperature contours on a $x - z$ cross-section of the channel located at $y = L_y/2$ for Case B. (a) $Ri_\tau = 0$. (b) $Ri_\tau = 18$. (c) $Ri_\tau = 36$. (d) $Ri_\tau = 60$. . . 33

7.3 Instantaneous velocity contours on a $x - z$ cross-section of the channel located at $y = L_y/2$ for Case A. (a) $Ri_\tau = 0$. (b) $Ri_\tau = 18$. (c) $Ri_\tau = 36$. (d) $Ri_\tau = 60$. . . . 34

7.4 Instantaneous velocity contours on a $x - z$ cross-section of the channel located at $y = L_y/2$ for Case B. (a) $Ri_\tau = 0$. (b) $Ri_\tau = 18$. (c) $Ri_\tau = 36$. (d) $Ri_\tau = 60$. 35

7.5 Variation of density and dynamic viscosity in the hot and cold sides of the channel for Case A and Case B. 37

7.6 Mean velocity and mean temperature profiles comparing Cases A and B. 38

7.7 Variance of velocity fluctuations for $Ri_\tau = 0,\ 18,\ 36,\ 60$ for Case A and B. 39

7.8 Semi-locally scaled variance of velocity fluctuations at $Ri_\tau = 0,\ 18,\ 36,\ 60$ for Case A and B. 40

7.9 Turbulent kinetic energy for $Ri_\tau = 0,\ 18,\ 36,\ 60$ comparing the $T_2/T_1 = 1.01$ case with $T_2/T_1 = 2$ case. 41

7.10 RMS values of temperature fluctuations for $Ri_\tau = 0,\ 18,\ 36,\ 60$ comparing the $T_2/T_1 = 1.01$ case with $T_2/T_1 = 2$ case. 42

7.11 Total stress profile for $Ri_\tau = 0,\ 18,\ 36,\ 60$ to illustrate the shift in the region of zero stress for the $T_2/T_1 = 2$ case in comparison to the $T_2/T_1 = 1.01$ case. 44

7.12 Variation of turbulent momentum flux for $Ri_\tau = 0,\ 18,\ 36,\ 60$ comparing $T_2/T_1 = 2$ case to the $T_2/T_1 = 1.01$ case. 44

7.13 Turbulent heat flux for different Richardson numbers comparing Cases A and B. . . 45

7.14 Mean velocity profiles for $Ri_\tau = 0,\ 18,\ 36,\ 60$ at $T_2/T_1 = 2$. 46

7.15 Mean temperature profiles for $Ri_\tau = 0,\ 18,\ 36,\ 60$ at $T_2/T_1 = 2$. 47

7.16 RMS values of temperature fluctuations and velocity fluctuations for $Ri_\tau = 0,\ 18,\ 36,\ 60$ at $T_2/T_1 = 2$ 48

7.17 TKE intensities for $Ri_\tau = 0,\ 18,\ 36,\ 60$ at $T_2/T_1 = 2$. 49

7.18 Stress budgets in the cold and hot regions for $Ri_\tau = 0,\ 18,\ 36,\ 60$ at $T_2/T_1 = 2$. . . 50

7.19 Turbulent and diffusive heat flux normalized with the wall heat flux in the channel for $Ri_\tau = 0,\ 18,\ 36,\ 60$ comparing cases B0, B1, B2, and B3. 51

7.20 Density gradient $(\partial\rho/\partial z)$ in the channel for Case A, a representative case for Boussinesq approximation. 52

7.21 Density gradient $(\partial\rho/\partial z)$ in the channel for Case B accounting for the NOB effects. 53

7.22 Variation of Brunt-Väisälä frequency in the channel with the distance from the wall. 54

7.23 Variation of gradient Richardson number in the bottom and top halves of the channel. 55

7.24 MKE budget for Cases A and B at $Ri_\tau = 0,\ 18,\ 36,\ 60$. 59

7.25 Spanwise vorticity profiles for Cases A and B for $Ri_\tau = 0,\ 18,\ 36,\ 60$. 60

7.26 Baroclinic torque production for $Ri_\tau = 0,\ 18,\ 36,\ 60$ at $T_2/T_1 = 1.01$ and at $T_2/T_1 = 2$. 61

7.27 Vortex stretching distribution in the entire channel for the neutrally buoyant case. . 62

7.28 Close up of the vortex stretching distribution in the vicinity of IGWs comparing Cases A and B. 62

B.1 Computational grid in the present work. 71

D.1 Mean velocity and mean temperature profiles comparing Cases A, B and C. 76

D.2 Variance of velocity fluctuations for $Ri_\tau = 0,\ 18$ for Cases A, B and C. 76

D.3 Semi-locally scaled variance of velocity fluctuations at $Ri_\tau = 0,\ 18$ for Case A, B and C. 77

D.4 RMS of temperature fluctuation values for $Ri_\tau = 0,\ 18$ comparing Cases A, B and C. 77

D.5 Variation of turbulent momentum flux for $Ri_\tau = 0,\ 18$ comparing Cases A, B and C. 77

D.6 Turbulent heat flux for different Richardson numbers comparing Cases A, B and C. 78

1

Introduction

A horizontal flow that is influenced by density variations in the vertical direction in the presence of gravity is called a stratified flow. If, in addition, the flow is turbulent, then there is a complex interplay between stratification and turbulence. The study of stratified turbulent flows is important to several applications in industrial processes as well as geophysical flows. Stratified turbulent flows are encountered in industrial processes like fluid motion in heat transfer equipment, combustion, transport of petroleum and natural gas, and cooling of nuclear reactors. They are also common in nature, as Earth's atmosphere and the oceans feature stratification. Indeed, atmospheric winds, ocean currents, mixing in rivers, and the transport of organic species in the ocean are examples of turbulent flows influenced by stratification.

Stratified turbulent flows are characterized by the relative importance of buoyancy and shear in the production or destruction of turbulence. The buoyancy forces can enhance or suppress turbulence depending on the nature and strength of stratification. These effects can be characterized by the so-called Richardson number Ri, with $Ri > 0$ corresponding to stable stratification and $Ri < 0$ to unstable stratification. For unstably stratified flows ($Ri < 0$), gravity enhances turbulent mixing as in Raleigh-Bénard convection. Conversely, for stably stratified flows ($Ri > 0$), turbulent fluctuations are damped by buoyancy. This reduction is the result of inhibiting the vertical fluctuation of velocity components by buoyancy. As turbulence tends to isotropy, the other two fluctuating components are suppressed as well. Therefore, buoyancy acts to suppress turbulence for flows with positive values of Richardson numbers. These flows have been of interest to scientists and engineers as they result in intriguing flow structures within the domain owing to the interplay between the density gradients, gravity, and turbulence itself.

Early research in the field of stratified turbulence mostly dealt with unbounded, homogeneous flows. Stillinger et al. (1983) and Itsweire et al. (1986) were among the first to carry out experiments on decaying grid-generated turbulence. Some of the direct numerical simulations(DNS) studies on homogeneous stratified turbulence include Métais and Herring (1989), Gerz and Yamazaki (1993), Staquet and Godeferd (1998) and Riley and DeBruynkops (2003). These studies identified an internal wavefield and observed a decay in the vertical velocity field as the flow evolved. These systems may be representative of the flow in the stratosphere or that in the deep ocean.

Turbulent stratified flows often feature a background shear, which in many cases can be considered to be uniform to the first approximation. Winds in certain regions of the atmospheric boundary layer are an example of this kind of flow. The behavior of stably stratified turbulent flows under homogeneous shear was investigated experimentally by Rohr et al. (1988). This study showed that turbulent kinetic energy is enhanced at lower stratification levels and turbulence decays at higher stratification levels. Several numerical studies of this type of system using direct numerical simulations(DNS) (Gerz et al. (1989), Holt et al. (1992), Jacobitz et al. (1997) and Shih et al. (2000)) and large eddy simulations (LES) (Kaltenbach et al. (1994)) have followed.

In the present work, turbulent stratified flows of interest are the ones that occur in the proximity of the walls. They are sheared and wall-bounded flows, i.e., stratified turbulence is forced by an applied shear in the presence of solid boundaries. These flows have also been studied extensively to better understand the physics of our atmosphere and oceans; see Mahrt (2014) for a review on stably stratified atmospheric boundary layers. In wall-bounded flows, the distribution of shear and stratification is inhomogeneous and varies with the distance from the wall. Therefore, different regimes can be identified within the flow with distinctive features. One such feature of these flows is the presence of non-turbulent internal gravity waves at the interface of lighter and denser fluids. These types of systems have been object of many numerical studies, especially in pressure-driven turbulent plane channel flow. Garg et al. (2000) and Armenio and Sarkar (2002) performed LES while Iida et al. (2002), Moestam and Davidson (2005) carried out DNS on stratified channel flows at different levels of stratification; Garcia-Villalba and Del Alamo (2011) also carried out DNS for higher friction Reynolds number. These studies are discussed in further detail in the next chapter.

Despite the breadth of numerical studies described above, almost all of them are carried out under the so-called Oberbeck-Boussinesq (OB) approximation, wherein the effects of variable inertia and viscosity are neglected. However, these assumptions are valid only if the fluid is incompressible and has constant thermophysical properties for a range of temperatures. For applications with large temperature differences, the variable inertia effects and other non-Oberbeck Boussinesq (NOB) effects are strong and can influence the flow structure, thereby yielding inaccurate results with the OB approximation. For instance, most of the stratified flows in industrial applications are variable-property flows, as they involve gases and supercritical fluids (Pitla et al., 1998; Dostal et al., 2006). Combustion chambers are also examples where the property variations can be significant. We know that stratification suppresses turbulence and it would be interesting to identify the impact of variable inertia effects on this deterioration. It is important to study wall-bounded stratified turbulent flows accounting for strong property variations in order to have a detailed understanding that would ultimately allow us to, for instance, develop more energy-efficient systems.

1.1 Outline

The outline of this thesis is presented below:

Chapter 2 introduces the OB approximation and presents an extensive review of the research on wall-bounded stably stratified turbulent flows.

Chapter 3 presents the research objectives of the present thesis that can be arrived at from the literature review.

Chapter 4 presents the low-Mach number approximation of the Navier-Stokes equations which are used in the present work to account for the NOB effects.

Chapter 5 describes the implementation of the low-Mach equations within the framework of an incompressible, constant-properties Navier-Stokes solver. The validation of the numerical methods is also presented.

Chapter 6 will elaborate on the numerical simulations carried out in the present work.

Chapter 7 discusses the results obtained in the current thesis.

2

Literature Review

Turbulent flows are characterized by chaotic motions of eddies of varying length scales. The large eddies are unstable and break into eddies of smaller scales and continue to do so until they are small enough to dissipate the kinetic energy as heat through viscous friction. This mechanism occurring across length scales would be affected by the presence of buoyancy forces and density gradients. In stably stratified cases, buoyancy forces contribute to the dissipation of turbulence through the transformation of turbulent kinetic energy into mechanical potential energy. In the present work, we will be focusing on stratified turbulent flows in the presence of walls. More precisely, we will be looking at stratified turbulent channel flows driven by a mean pressure gradient in the presence of gravity. In this chapter, we will discuss the characteristic length scales and non-dimensional numbers in stably stratified turbulent flows. The OB approximation will be reviewed, and subsequently, different studies carried out using this approximation are explored. Further, we will briefly discuss some studies accounting for NOB effects and finally look at the structure of these flows and their characteristics.

2.1 Length scales

Turbulent flows, in general, are comprised of energy exchanges between the large and small eddies through inviscid mechanisms, and eventually, the small eddies dissipate through viscous means. This interplay between inertial and viscous forces may be affected when gravity is active. It is of interest to identify the length scales at which the buoyancy forces dominate, just like how the viscous forces act only on the smallest scale of eddies.

Monin and Obukhov (1954) were among the first to study stratified turbulent flows. In their work, empirical data of temperature fluctuations and vertical wind velocity under various conditions of temperature stratifications were analyzed to show that the variation of mean flow and turbulence characteristics depend on friction velocity, buoyancy flux, and height. A self-similarity theory was derived that would describe the turbulent regime in an inhomogeneous temperature medium with a minimum number of parameters. A length scale, L_{MO}, is defined that corresponds to the height of the layer within which turbulence is predominantly shear-driven, or, in other words, the distance from the wall above which buoyancy starts affecting the flow. This parameter reads,

$$L_{\mathrm{MO}} = \frac{\rho_0 u_\tau^3}{C_k g q_w}, \tag{2.1.1}$$

with ρ_0 the density of the fluid, u_τ the friction velocity, C_k the Von-Kármán constant and q_w the mean wall heat flux. This quantity can be related to another important parameter, the shear Richardson number, (Ri_τ). L_{MO} gives an estimate for the distance from a boundary at which turbulence generation by buoyancy is of the same order as the turbulence generation by shear.

However, the self-similarity theory used to derive this length scale specifically applies to atmospheric boundary layers.

Ozmidov (1965) suggested an estimate for the smallest length scale, L_{O}, influenced by buoyancy. Buoyant effects influence eddies whose length scale is larger than the Ozmidov scale. This behavior of buoyancy places an upper bound for the length scale of large eddies in the turbulent flow. The Ozimdov scale is given as

$$L_{\mathrm{O}} = \left(\frac{\epsilon}{N^3}\right)^{1/2}, \tag{2.1.2}$$

where ϵ is the turbulent kinetic energy dissipation rate and N is the buoyancy frequency or the frequency at which a vertically displaced particle will oscillate in a statistically stable environment.

In addition to these length scales, the smallest eddies are given by the Kolmogorov length scale η (Pope, 2000) at which turbulence dissipation as heat by viscosity occurs. At high Reynolds numbers, there is a wide separation of scales between η and the largest flow scales (typically set by the flow geometry). The Kolmogorov length scale is given by,

$$\eta = \left(\frac{\nu_0^3}{\epsilon}\right)^{1/4}, \tag{2.1.3}$$

where ν_0 is the kinematic viscosity of the fluid.

The eddies in the wall region scale with the distance from the wall and in the core region scale with the dimensions of the channel. The largest size of eddies, locally, in a turbulent flow field can be given by the distance of the location from the nearest boundary, L_z. Having defined all these length scales, the dominant balances in these flows can be visualized by sketching qualitatively, the variation of L_{O}, η, and L_z in the wall-normal direction as shown in Fig. 2.1. In the region close to the wall, the largest eddies are smaller than the Kolmogorov scales and, therefore, are acted upon by the viscous forces and dissipated into heat. At a certain distance away from the wall, the eddies are larger than the Kolmogorov scales but smaller than the Ozmidov scales and therefore are not directly affected by viscous and buoyancy forces. In this region, buoyancy forces act neither on large-scale eddies nor small-scale eddies. The Ozmidov scale decreases in wall-normal direction until reaching that of the large eddies at that location. From this point onward, the buoyancy effects directly influence the large-scale motions, while smaller eddies are still unaffected. Finally, when the Ozmidov scale is smaller than the smallest eddy scale, the flow is completely dominated by buoyancy.

As will be shown later in this thesis, this analysis of dominant balances can be recast in terms of non-dimensional parameters, which will inform us about the extent of the regions shown in Fig. 2.1. In the next section, we present the basic non-dimensional flow governing parameters.

2.2 Wall-bounded stratified turbulent flows

Turbulent flow wherein the lighter fluid flows over the heavier fluid is called a stably stratified turbulent flow. The flow is driven by a constant mean pressure difference and stratification is achieved by subjecting the walls of the channel to different temperature boundary conditions. The Navier-Stokes equations for wall-bounded stratified flows can be greatly simplified by the introduction of the Oberbeck-Boussinesq (OB) approximation. Although this approximation has a narrow range of validity and cannot account for non-Oberbeck Boussinesq (NOB) effects, it provides valuable insights into the physics that would be encountered in the problem. In the next section, we will discuss the OB approximation and also review the research on wall-bounded stably stratified turbulent flows using the OB approximation.

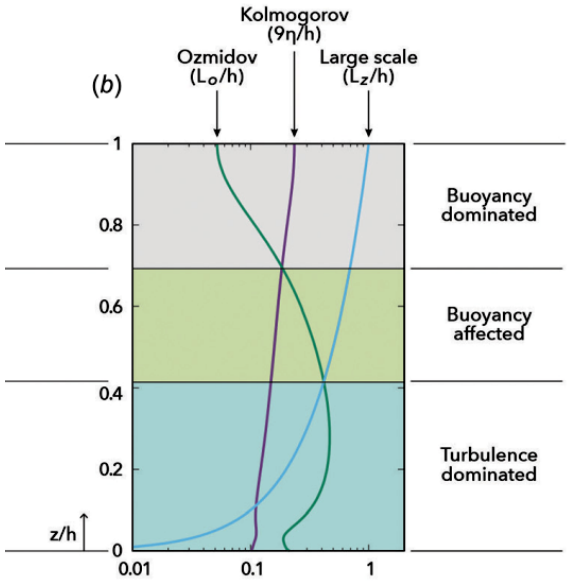

Figure 2.1: Variation of Ozmidov and Kolmogorov length scales with respect to the length scale of large eddies in wall-normal direction. The figure is taken from Zonta and Soldati (2018). Note that h is the half-channel height.

2.3 Oberbeck-Boussinesq approximation

The OB approximation is based on the assumption that the density variations in the fluid are small enough and can be neglected in the continuity equation as well as the advection terms of the momentum equation. However, the density variations cannot be neglected in the gravitational term of the momentum equation. Acceleration due to gravity is in general much larger than the local value of fluid acceleration (i.e., $|g| >> |Du_i/Dt|$), therefore the product ρg is significant even when the density variations are small. Hence, density is assumed to be constant except in the term where it is multiplied by gravity. Further in OB approximation, all thermophysical properties are constant and uniform. Conservation of mass, momentum, and energy equations are written in the dimensionless form under OB approximation as:

$$\frac{\partial u_i}{\partial x_i} = 0, \tag{2.3.1}$$

$$\frac{\partial u_i}{\partial t} + u_j \frac{\partial u_i}{\partial x_j} = -\frac{\partial p'}{\partial x_i} + \frac{1}{Re_\tau} \frac{\partial^2 u_i}{\partial x_j^2} + Ri_\tau \rho' \delta_{i,3} + \delta_{1,i}, \tag{2.3.2}$$

$$\frac{\partial T}{\partial t} + u_i \frac{\partial T}{\partial x_j} = \frac{1}{Re_\tau Pr} \frac{\partial^2 T}{\partial x_j^2}, \tag{2.3.3}$$

where p' is the fluctuating kinematic pressure and $\delta_{1,i}$ is the mean pressure gradient. ($\delta_{i,j} = 1$, if $i = j$). Buoyancy forces, that depend on local density gradients, acting in the wall-normal direction play a significant part in wall-bounded stratified turbulent flows as they interact with the turbulence and alter the mass, momentum, and heat transfer rates. This interplay between the turbulence and gravity forces is quantified in terms of three non-dimensional numbers that appear on non-dimensionalizing the equations, namely the shear Reynolds number (Re_τ), shear Richardson number (Ri_τ), and the Prandtl number (Pr). These three numbers describe the physics involved in stratified turbulent channel flows: Re_τ describes the competition between the inertial forces and the viscous forces, Ri_τ measures the interplay between the buoyancy and inertial forces – thereby quantifying the stratification level – and Pr is the ratio of momentum diffusivity to the thermal diffusivity.

$$Re_\tau = \frac{u_{\tau 0} h}{\nu_0}, \qquad Ri_\tau = \frac{g \Delta \rho h}{\rho_0 u_{\tau 0}^2}, \qquad Pr = \frac{\nu_0}{\lambda_0}, \tag{2.3.4}$$

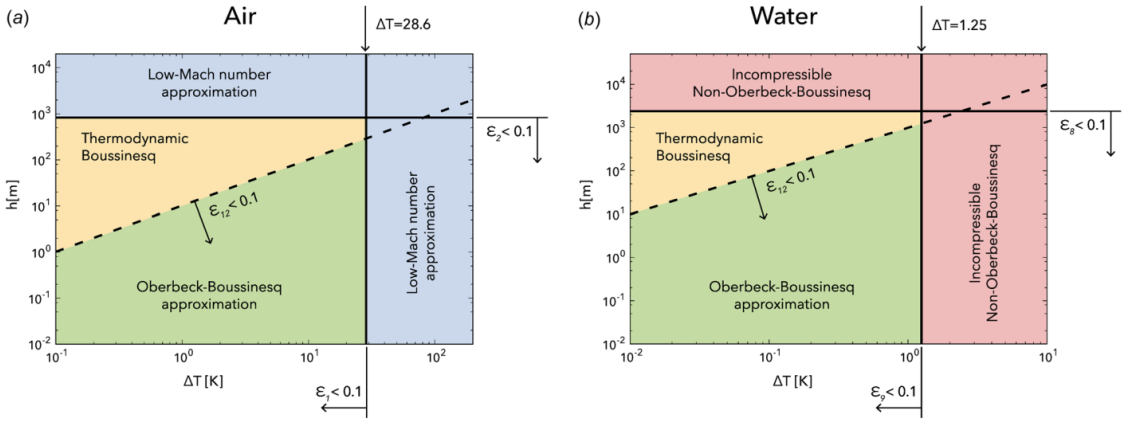

Figure 2.2: A parameter space $(\Delta T, h)$ of wall-bounded stratified turbulence with the different numerical approach that can be used for its description. The figure is taken from Zonta and Soldati (2018). Note that there are constraints given by ϵ, and the reader is directed to the reference for further reading.

where ρ_0, ν_0, λ_0 are reference fluid density, kinematic viscosity, and thermal diffusivity. $u_{\tau 0}$ is the initial shear velocity and is prescribed based on the mean pressure drop. g is the acceleration due to gravity and h is the half channel height. The density difference $\Delta\rho = \rho_b - \rho_t$, is due to the temperature difference between the bottom and top wall. This can also be expressed as $\Delta\rho/\rho_0 = -\beta_0 \Delta T$, where ΔT is the difference between the top and bottom walls. The reference temperature at which the properties are calculated is the mean temperature between the top and bottom walls.

Zonta and Soldati (2018) in their review paper discuss the range of validity of the OB approximation. A schematic of parameter space of $(\Delta T, h)$ is presented to summarise the discussion, and the schematic is shown in Fig. 2.2.

Several numerical studies have been carried out to understand the physics involved in stably stratified turbulent flows and are done so using the OB approximation. Some of the prominent studies are discussed in the next section.

2.3.1 Numerical studies

Gage and Reid (1968) studied the stability of thermally stratified flows and showed that for positive values of the Richardson number, the effect of stratification is completely stabilizing, and there exists a value of positive Richardson number, above which, the flow is completely stabilized. They mathematically calculated the dependence of the critical centerline Richardson number on the Reynolds number, yielding a neutral stability curve. The relation rewritten in terms of shear Reynolds number and shear Richardson number given by Zonta and Soldati (2018) is shown in Fig. 2.3. As it is evident, most studies have been performed on weakly-stratified turbulent flows and some of them are discussed in the following paragraphs.

Weakly/moderately-stratified turbulent flow: Garg et al. (2000) studied inhomogeneous stratified shear flows using Large Eddy Simulations (LES). Simulations were carried out on open and closed channels, wherein the flow was driven by a pressure gradient and stable stratification was maintained by fixing the wall temperatures. The transport equation for density was solved instead of solving the energy equation for temperature distribution. Although they did account for variable viscosity, the influence of temperature on the thermophysical property of air was limited. The simulations were performed for constant Reynolds and Prandtl numbers, ($Re_\tau = 180$, $Pr = 0.71$), over a range of shear Richardson numbers ($0 < Ri_\tau < 60$ for closed channel flows. Based on the values of shear Richardson numbers, three different flow regimes were identified namely: buoyancy-affected regime ($Ri_\tau < 30$), where turbulence is partially subdued; buoyancy-

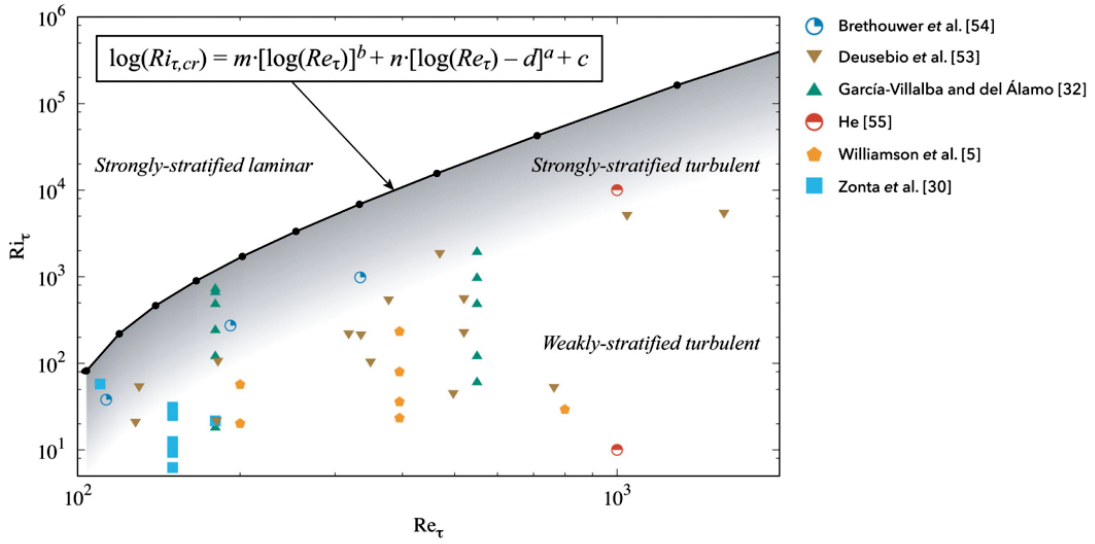

Figure 2.3: A parameter space (Re_τ, Ri_τ) of wall-bounded stratified turbulence depicting the current state of research. The black line indicates neutral stability curve and the with symbols denoting simulations of Brethouwer et al. (2012), Deusebio et al. (2015), Garcia-Villalba and Del Alamo (2011), He (2016), Williamson et al. (2015), Zonta et al. (2012b). The figure is taken from Zonta and Soldati (2018).

controlled regime ($30 < Ri_\tau < 45$), characterized by transient and local flow relaminarization; and buoyancy dominated-regime ($Ri_\tau > 45$), characterized by relaminarization in the whole flow. These findings were not consistent with the linear stability analysis by Gage and Reid (1968). The reason for the inconsistency can be understood from the plot showing the evolution of the bulk velocity presented by Garg et al. (2000). It is clearly evident that the results do not correspond to the final steady state, but instead, an intermediate transient state.

Armenio and Sarkar (2002) also performed LES on closed channel stratified turbulence using the Boussinesq approximation at $Re_\tau = 180$ and $Pr = 0.71$, but maintained all thermophysical properties constant and simulated up to stratification of $Ri_\tau = 480$. Increasing the Richardson number reduced the turbulence activity but, unlike Garg et al. (2000), there was no relaminarization observed. Armenio and Sarkar (2002) observed sustained turbulence at $Ri_\tau = 480$ and suggested that the flow relaminarization observed in Garg et al. (2000) was only a transient effect occurring for a limited period and disappearing over a longer time interval and the flow eventually recovering to a new statistically stable condition of stratified turbulence.

Iida et al. (2002) performed DNS of stably-stratified wall-bounded turbulence at $Re_\tau = 150$ and $Pr = 0.71$ using the Boussinesq approximation and constant thermophysical properties. The energy equation for temperature distribution was solved, unlike in the previous cases where the energy equation was solved for density distribution. Turbulence was observed on only one side of the channel while the other side was laminar at $Ri_\tau = 40$. Moestam and Davidson (2005) also conducted DNS of turbulent pressure-driven flow with stable stratification and discussed properties of relaminarization due to the domain size in connection to the results of Iida et al. (2002). They concluded that too small a box size results in relaminarization.

Garcia-Villalba and Del Alamo (2011) also performed DNS of stably-stratified turbulent channel flow at a very high Reynolds number of $Re_\tau = 550$ and a wide range of stratification levels. The equations were solved using the OB approximation. For weak stratification or high Reynolds number flows, the turbulence is affected by buoyancy only in the outer region and close to the wall resembles an unstratified case. However, at higher Richardson numbers, the near wall region has large laminar patches ($Ri_\tau \geq 60$ for $Re_\tau = 180$ or $Ri_\tau \geq 1920$ for $Re_\tau = 550$). At these values, the mean flow can sustain turbulence only if the computational box is large enough to accommodate these patches. If the computational box is too small then the laminar patches occupy the entire domain and do not allow a transition back to turbulence. Thus, explaining the full relaminarization

observed by Garg et al. (2000) and Iida et al. (2002) at sub-critical values of Ri_τ.

More recently, Zonta et al. (2022) analysed the flow at $Re_\tau = 1000$ and $Pr = 0.71$ for range of Ri_τ values upto $Ri_\tau = 300$. Within this range, turbulence was sustained close to the walls where the mean shear is too strong and buoyancy cannot compete. Farther from the wall, the effects of stratification are felt as the mean shear decreases. They also verified the previous studies that although the wall-normal velocity fluctuations and temperature fluctuations are large, they are decorrelated (have a phase lag of $\pi/2$), and therefore their product is small, almost going to 0 for $Ri_\tau \geq 200$ as reported by others before.

Strongly-stratified turbulent flow: The flow close to the stability curve is not as well explored as it is away from it. Some studies are available for strongly stratified flows. Nieuwstadt (2005) performed DNS on open channel turbulent flow with very large stratification and concluded that the turbulence decays and the flow approaches a laminar state. Flores and Riley (2011) performed DNS on the same configuration as that of Nieuwstadt (2005) to analyze in more detail the collapse of turbulence in strongly stratified flows. They showed that the critical parameter that controls the transient relaminarization is $Re_L = u_\tau L_{\mathrm{MO}}/\nu$, where u_τ is friction velocity and L_{MO} is the Obukhov length scale as discussed in an earlier section. The critical value of Re_L at which turbulence collapses was estimated to be about 100. Brethouwer et al. (2012) and He (2016) also performed DNS on strongly stratified turbulent flows and showed that the buoyancy affects the near wall region as well and the near wall turbulence is damped and laminar patches are observed. Deusebio et al. (2015) performed DNS on Couette flow and identified that as the stratification increases, laminar regions appearing for higher Re_τ seem more confined to the wall as that for lower Re_τ the laminar patches span the entire domain depth thus verifying the results of Brethouwer et al. (2012). They also modified the estimate of the critical value of Re_L to 200. However, more understanding is required in the case of strongly stratified turbulent flows.

2.4 Non-Oberbeck Boussinesq effects

The OB approximation can provide accurate results within a very limited range of parameters which is reviewed in Zonta and Soldati (2018). If the thermodynamic properties of the fluid vary with temperature and/or pressure then the NOB approaches must be used. If the fluid is gas then compressibility effects also become relevant. Some of the studies accounting for these effects are elaborated here.

Incompressible NOB approach: Liquids far from their critical points are mostly incompressible and the density can be considered a constant. In such cases, it becomes important to account for temperature or pressure variations of thermophysical properties of viscosity, thermal expansion coefficient, and thermal conductivity(μ, β, λ) of the fluid. The density is treated in a similar way as it was done during OB approximation.

Garg et al. (2000) performed LES with varying fluid viscosity and thermal diffusivity, but the influence of temperature changes on the properties of air was not pronounced therefore the flow changes were also very less evident. Later, for the longest time studies were mostly carried out keeping the properties constant and the studies of NOB effects for stratified turbulence have been fewer.

Zonta et al. (2012b) performed DNS on stably stratified turbulent channel flow with temperature-dependent fluid properties (viscosity (μ) and thermal expansion coefficient (β)). Three simulations were performed at ($Re_\tau = 180$, $Ri_\tau = 346$), ($Re_\tau = 150$, $Ri_\tau = 498$), ($Re_\tau = 110$, $Ri_\tau = 926$) and $Pr = 3$. Regardless of the initial Ri_τ, all cases exhibited a transition from turbulent to laminar state initially. However, if the Ri_τ is below a threshold value, then the flow transitions back to turbulence, with the exception of the case $Ri_\tau = 926$, which remained laminar. After this transition, the flow reaches a statistically steady state in which turbulence coexists with IGWs. The temperature-dependent properties cause asymmetry in the flow. In the case of temperature-

dependent viscosity, local flow relaminarization is observed on the cold side of the wall because the viscosity is higher thereby reducing the turbulence intensity while turbulence is sustained on the hot side of the wall. In the case of temperature-dependent thermal expansion coefficient, local flow relaminarization is observed at the hot side of the wall because of larger buoyancy forces. They also reported that for lower Re_τ, effects of temperature-dependent viscosity were more significant than temperature-dependent thermal expansion coefficient and vice versa for high Re_τ flows.

Low-Mach number approximation: The incompressible NOB approach cannot account for variable inertia effects. The low-Mach number approximation is valid for flows at low speeds, involving significant variation of density with temperature, which is the case, for instance, in gases and liquids close to their critical point. Majda and Sethian (1985) first presented the system of equations applied to the process of combustion. The system of equations allowed for large temperature and density variations, heat release, and effects of turbulence and was much simpler than the complete set of equations for compressible flow as the details of the acoustic waves had been omitted. McMurtry et al. (1986) also simultaneously performed DNS of a two-dimensional mixing layer using an approximate set of equations valid for low-Mach flows. They theorized that acoustic waves do not interact with the flow and thus filtering them out allows for larger timesteps thereby improving computing efficiency. Therefore, the approximate set of equation valid for low-Mach flows relieves the time-stepping constraint and at the same time allow density non-uniformities resulting from heat release to develop. The equations are presented in the next chapter. Low-Mach number approximation of Navier-Stokes equations is extensively used in various cases to solve combustion and heat transfer problems. However, studies on wall-bounded stratified turbulence using low-Mach number approximations have been fewer.

Lessani and Zainali (2009) performed LES on a closed channel flow at $Re_\tau = 180$ and $Pr = 0.71$ using low-Mach number approximation. The temperature ratio between the hot wall and the closed wall was varied from 1.01 to 6. Equations mentioned in section A were used and dependence of properties on temperature was given by Sutherland's law. At higher temperature ratios, the flow was asymmetrical because of the difference in properties on the two sides of the channel. The suppression of turbulence was higher closer to the hot wall. Increasing Ri_τ for a given temperature difference suppressed the turbulence across the channel.

The other instances where studies have been carried out using the low-Mach number approximation while considering buoyancy include the turbulent flow of supercritical carbon dioxide and supercritical water. Bae et al. (2005, 2008) carried out DNS of turbulent supercritical carbon dioxide flowing in heated vertical tubes at inlet bulk Reynolds number of 5400. The attenuation and restoration of turbulence due to interaction with the buoyant effects significantly affected the heat transfer coefficient. Nemati et al. (2015) performed DNS of heated pipe flows with carbon dioxide above the supercritical pressure and studied the effect of buoyancy and large thermophysical property variations on the mean flow statistics using the low-Mach approximation at $Re_\tau = 360$. Peeters et al. (2016) also used the low-Mach approximation to simulate the turbulent flow of supercritical carbon dioxide in a vertical annulus with a hot inner wall and cold outer wall at bulk Reynolds number of 8000. The turbulence was suppressed significantly at the hot wall and also the turbulent shear stress was lower. This behavior was attributed to variations in thermophysical properties and density stratification. Chu and Laurien (2016) simulated heat transfer of supercritical carbon dioxide in horizontal pipe with DNS for the first time at moderately low inlet bulk Reynolds number of 5400. A constant wall heat flux was applied. Because of buoyancy, stratification developed, and the lighter fluid which is at a higher temperature accumulated in the top part of the pipe resulting large degree of temperature variation in the circumferential direction. It was observed that turbulence was attenuated at the top layer because of reduced Reynolds stress near the top wall. These studies suggest that the physics is interesting and complex when the turbulent flow has variations in density and thermophysical properties in the presence of buoyant effects. The number of studies in this domain have been fewer and the topic demands more understanding which serves as the motivation for the current work.

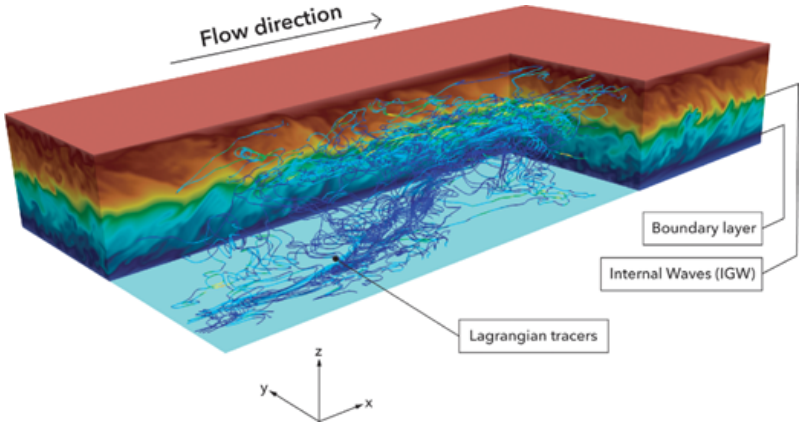

Figure 2.4: The structure of wall-bounded stably stratified turbulence. Close to the wall, turbulence is sustained while away from the wall, the region is dominated by buoyancy forces and we see the presence of IGW. The figure is taken from Zonta and Soldati (2018).

2.5 Internal gravity waves (IGW)

In stably stratified turbulent flows, turbulence remains the dominant flow structure in the near-wall region because of the larger shear in the region. However, toward the core of the channel, where the buoyancy effects are felt on large scales and turbulence is suppressed, dominant structures are the non-turbulent wavy structures called the internal gravity waves (IGWs). The presence of these waves is extensively reported in the literature (Iida et al., 2002; Armenio and Sarkar, 2002; Garcia-Villalba and Del Alamo, 2011). IGWs are characteristic of stably-stratified turbulent flows and appear because the buoyancy force restores a particle to its initial position when a particle is displaced vertically. The particle overshoots inertially and oscillates, thereby giving a wavy motion. The frequency of oscillation of the fluid particle is given by Brunt-Väisälä frequency which is given as:

$$N = \sqrt{\frac{-g}{\rho_0}\frac{\partial \rho}{\partial z}}. \tag{2.5.1}$$

The inverse of Brunt-Väisälä frequency or buoyancy frequency can be thought of as a time scale, the time taken by a displaced particle to come back to its equilibrium position. From the equation, it is clear that the frequency is a function of the local density gradient in the wall-normal direction, and therefore, the larger the density gradient, the smaller the time taken by a particle to reach the equilibrium position, which points towards the decreased influence of turbulent fluctuations and increased effects of stabilizing buoyancy.

The IGWs are present at the interface of the lighter and denser fluids. The density gradients at the interface are larger than anywhere else in the domain (thermocline). The presence of this interface affects the turbulent mixing and in turn the heat and momentum transfer rates. Iida et al. (2002) first reported that there is a phase lag of $\pi/2$ between density fluctuations and the vertical velocity fluctuations. This is shown in Fig. 2.5 in which it can be clearly seen that the crest of density fluctuations falls directly on zero of the velocity fluctuations contour. IGWs decorrelate the vertical fluctuations and the temperature fluctuations thereby causing a decrease in turbulent heat flux, resulting in a steep mean temperature gradient at the core.

2.6 Influence of stratification on macroscopic heat and momentum transfer rates

As discussed above, for stably stratified turbulence, if the stratification is not so strong as to suppress turbulence completely, the flow in the core of the channel would have IGWs as the dominant structures rather than turbulence. For neutrally-buoyant flows, there is no mechanism for the initiation of IGWs as there is no restoring force acting on particles that are displaced vertically. These IGWs affect the heat and momentum transfer rates. The IGWs are characterized

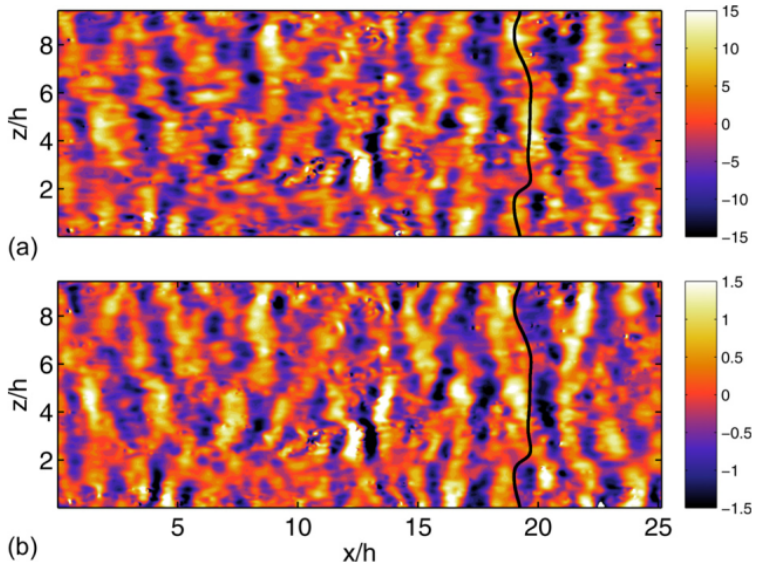

Figure 2.5: (a)Instantaneous fluctuations of density. (b) Instantaneous fluctuations of wall-normal velocity at horizontal plane $y/h = 1$. The simulation was carried out for $Re_\tau = 550$ and $Ri_\tau = 480$. Note that y is the wall-normal direction and z is the spanwise direction. The black curve represents the crest of the representative density field. The figure is taken from Garcia-Villalba and Del Alamo (2011).

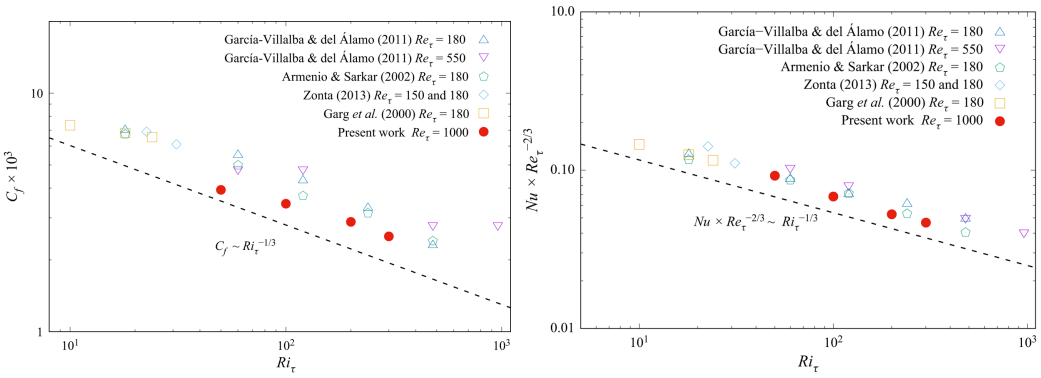

(a) Friction Factor as a function of Ri_τ.

(b) Rescaled Nusselt number as a function of Ri_τ.

Figure 2.6: Variation of friction factor and Nusselt number with Ri_τ. The figure is taken from Zonta et al. (2022).

by strong temperature gradients and the fluid particle that reach the interface cannot penetrate them as the energy required to do so is high, thereby reducing the momentum and heat transfer rates (Armenio and Sarkar, 2002; Iida et al., 2002; Garcia-Villalba and Del Alamo, 2011). The regions of strong temperature gradients are called thermocline and in the case of a stably stratified channel, it is formed right where the mean shear vanishes hindering the heat and momentum transfer rates. The momentum and heat transfer rates are quantified by friction factor (C_f) and the Nusselt number (Nu). The definition used by Garcia-Villalba and Del Alamo (2011) is given as,

$$C_f = \frac{2\tau_w}{\rho u_b^2}, \qquad Nu = \frac{2q_w h}{\lambda \Delta T}, \tag{2.6.1}$$

where λ is the thermal conductivity. Nu is the ratio of convective to conductive heat transfer. C_f is the ratio of wall shear stress to the kinetic energy of the flow. Garcia-Villalba and Del Alamo (2011) also obtained a scaling for C_f in terms of Ri_τ as $C_f \sim Ri_\tau^{-2/3}$. Zonta et al. (2022) obtained a scaling for Nu as $Nu \times Re_\tau^{-2/3} \sim Ri_\tau^{-1/3}$ as shown in Fig. 2.6a and Fig. 2.6b.

Zonta (2013) used results obtained from Zonta et al. (2012b) and compared them to DNS of stratified turbulence under OB conditions. He found that the NOB effects result in significant variations of heat and momentum transfer rates (up to 30%).

2.7 Discussion

Stably stratified turbulent flows have been of interest for a long time and with the enhancement of the computational power, numerical simulations have become very popular. These flows have mostly been analyzed using the OB approximation without accounting for variable inertia effects or variations in thermophysical properties. As these flows are characterized by numerous interesting flow structures, it would be important to understand the effects of property variations on these structures.

There are studies in which simulations are performed accounting for variations in viscosity and thermal conductivity, however, simulations with variable inertia effects are few. There are no DNS cases available that implement the variable inertia and account for strong density gradients. Therefore, DNS of stably stratified turbulent flows with strong property variations can potentially contribute to the current physical understanding through accounting of NOB effects, especially strong density variations in the flow. Analysis of these DNS results can provide useful insights into flow structure at different levels of stratification and also estimate the effect of buoyancy on turbulence intensities, heat, and momentum transfer rates.

3

Objective and Scope of Thesis

The objective of this thesis is:

> *To analyze the problem of stably stratified wall-bounded turbulence with strong variations in density and thermophysical properties of the fluid at different levels of stratification.*

Stably stratified wall-bounded turbulence under OB conditions has given insights into physics and has provided the first estimates of the problem, but OB approximation is never exactly valid in practice. Due to the narrow range of validity of OB approximation, it becomes necessary to account for Non-Oberbeck Boussinesq (NOB) effects. Few studies have been carried out accounting for the variation of the thermophysical properties of fluids keeping the density constant, for fluids like water. However, even fewer studies are available for stably stratified wall-bounded turbulent flows with large density gradients. Thus, in this thesis, we will look to understand the physics of stably stratified wall-bounded turbulent flow subjected to variations in density and other thermophysical properties.

The *scope* of this thesis is limited to calorically perfect fluids in a fully developed channel flow. Also, the velocity of the fluid should be much lower than the speed of sound as we use the low-Mach number approximation.

4

Governing Equations

The Navier-Stokes equations are mathematical expressions for the conservation of mass and momentum. Although the idea of conservation itself is straightforward, solving these equations in the most general form is anything but simple, as it would call for an inordinate amount of computational power and time. However, these equations can be greatly simplified by neglecting some of the physics that is not relevant and/or lies outside our interests. The Boussinesq approximation is one such simplification, where the density variations are assumed to be too small to influence the continuity equation and the convection terms in the momentum equation. In the present work, another simplification of the Navier-Stokes equations called the low-Mach number approximation is used. In this approach, the density variations due to temperature are accounted for in the equations. In this chapter, we will start off with a brief discussion on the low-Mach number approximation of the Navier-Stokes equations and discuss the governing equations that describe stably stratified turbulent flows. We will identify the relevant non-dimensional numbers that become apparent, derive the constraints that arise naturally through the imposition of low-Mach number approximation, and also refer to the relations used to compute the thermophysical properties.

4.1 Low-Mach number approximation

The idea behind the low-Mach number approximation, as touched upon in the previous chapter, is to filter the acoustic waves and evaluate the density and other thermodynamic properties as functions of temperature only. This approach works when the density fluctuations due to variations in pressure are insignificant and gives a valuable alternative to keep away from solving the Navier-Stokes equations for fully compressible flows while still accounting for variations in thermophysical properties (Majda and Sethian, 1985; McMurtry et al., 1986; Cook and Riley, 1996).

In solving for low-Mach number flows or, more precisely, in the limit of vanishing Mach, we assume that $\gamma M^2 << 1$ and express dependent variables as asymptotic expansions of γM^2 and then reduce the Navier-Stokes equations to leading order of γM^2. For example, we write pressure as $p = p^{(0)} + (\gamma M^2)p^{(1)} + (\gamma M^2)^2 p^{(2)} + \cdots$, and the same can be done with velocity and temperature. The derivation for the low-Mach number approximation is detailed in the section A.1, however, the essence of the approach is discussed in this section.

The idea behind expressing the pressure as an asymptotic expansion of γM^2 is that we can now address total pressure to be the weighted sum of *thermodynamic* pressure ($p^{(0)}$) and the *dynamic* pressure ($p^{(1)}$). The thermodynamic pressure does not vary in space (or the variations occur at much smaller orders of magnitude) and therefore does not directly influence momentum transport. The variations of dynamic pressure in space, however, occur in the same order of magnitude as the other terms in the momentum equation. Hence, dynamic pressure transports momentum. The decomposition of pressure allows for the exclusion of thermodynamic pressure from the momentum

equation. In other words, we decouple the thermodynamic pressure from the momentum equation.

It is important to note that the variations in dynamic pressure are too small to affect the thermophysical properties. Therefore, these properties are computed as functions of thermodynamic pressure (spatially invariant) and the temperature field across the domain. The thermodynamic pressure remains constant in time as well for an open system, but the variations with time become relevant for a closed system. The final form of equations that were implemented to solve stratified turbulent flows is discussed in the next section while the steps to arrive at these equations are detailed in the section A.1.

4.2 Governing equations

As discussed previously, expressing the dependent variables as power series of γM^2, substituting these expansions in the continuity, momentum, and energy equations, and collecting the lowest order terms in γM^2 yields the governing equations which are shown below:

$$\frac{\partial \rho}{\partial t} + \frac{\partial \rho u_j}{\partial x_j} = 0, \tag{4.2.1}$$

$$\rho \frac{\partial u_i}{\partial t} + \rho u_j \frac{\partial u_i}{\partial x_j} = -\frac{\partial p}{\partial x_i} + \frac{1}{Re_\tau} \frac{\partial \tau_{ij}}{\partial x_j} + \delta_{i,1} + \rho \, \frac{Ri_\tau}{\Delta\rho/\rho_0} \delta_{i,3}, \tag{4.2.2}$$

$$\rho C_p \frac{\partial T}{\partial t} + \rho C_p u_j \frac{\partial T}{\partial x_j} = \frac{1}{Re_\tau \; Pr} \frac{\partial}{\partial x_j} \left(\lambda \frac{\partial T}{\partial x_j} \right) + \frac{Q}{Re_\tau \; Pr} + \frac{\gamma - 1}{\gamma} \frac{\mathrm{d}p_0}{\mathrm{d}t}, \tag{4.2.3}$$

$$p_0 = \rho T. \tag{4.2.4}$$

Note that the superscript indicating the order is omitted, and all variables correspond to the zeroth order, except pressure. The zeroth order pressure (thermodynamic pressure) is indicated with p_0 and the first order pressure (dynamic pressure) is indicated with p. $\delta_{i,1}$ is the constant pressure difference driving the flow . Also, note that the variables are normalized using the values at the reference state. The reference temperature is T_0, which is the mean temperature of the walls, and the reference thermodynamic properties are calculated at the reference temperature, namely, ρ_0, λ_0, μ_0 and C_{p0}. The Reynolds, Richardson, and Prandtl numbers are given as:

$$Re_\tau = \frac{\rho_0 u_{\tau 0} h}{\mu_0}, \qquad Ri_\tau = \frac{\Delta\rho g h}{\rho_0 u_{\tau 0}^2}, \qquad Pr = \frac{\mu_0 C_{p0}}{\lambda_0}, \tag{4.2.5}$$

with g being the acceleration due to gravity, h being the half-channel height, and $u_{\tau 0}$ is the initial friction velocity given as,

$$u_{\tau 0} = \sqrt{-\frac{h}{\rho_0} \frac{\partial p}{\partial x}}. \tag{4.2.6}$$

This definition of friction velocity is different from the commonly used one in terms of the shear stress at the walls. In the current setup, the shear stress at both walls is not the same as the flow is subject to variable properties, and therefore, using the classical definition is not straightforward. The definition given in Eq. (4.2.6) is based on the constant driving pressure gradient and stems from simple force balance on the entire channel. This allows for consistency and reproducibility of the simulations carried out in the present work. The reference velocity was also used by Zonta et al. (2012a).

It is also important to point at the buoyancy term in Eq. (4.2.2). The $\Delta\rho/\rho_0$ factor does not appear naturally on normalization but is introduced artificially because it aids in the comparison of non-Oberbeck cases against the cases of Boussinesq approximation at a given Richardson number, with $\Delta\rho$ being the density difference between the top wall and the bottom wall. Essentially, we are

incorporating the non-dimensional number given by the temperature ratio between the walls into the Richardson number to be consistent in our comparison against the Bousssinesq approximation.

In addition to the equations described above, there are other constraints that can be imposed on the system. We know that the system is closed and hence, the total mass in the system should remain constant. If the total mass of the system is M_0, we can use this to compute the thermodynamic pressure in the system. By integrating Eq. (4.2.4), we obtain the variation of thermodynamic pressure with time,

$$p_0(t) = \frac{M_0}{\int_V \frac{1}{T} dV}. \tag{4.2.7}$$

The unknowns are $u,\ v,\ w,\ T,\ \rho,\ p_0,\ p$ and the equations at our disposal are Eq.(4.2.1), (4.2.2), Eq.(4.2.3), Eq.(4.2.4) and Eq.(4.2.7) . Therefore, we have 7 equations and 7 unknowns, forming a closed set.

Further reworking of the governing equations will be convenient for the numerical implementation described in the next chapter. To evaluate $\frac{\mathrm{d}p_0}{\mathrm{d}t}$, we integrate Eq. (4.2.3) over the entire volume,

$$\frac{\mathrm{d}p_0(t)}{\mathrm{d}t} = \frac{\gamma}{V} \frac{1}{Re_\tau\ Pr} \int_V \frac{\partial}{\partial x_j} \left(\lambda \frac{\partial T}{\partial x_j} \right) dV + \frac{\gamma\ Q}{Re_\tau\ Pr}. \tag{4.2.8}$$

The volume integral can be replaced with a surface integral to get,

$$\frac{\mathrm{d}p_0(t)}{\mathrm{d}t} = \frac{\gamma}{V} \frac{1}{Re_\tau\ Pr} \int_S \lambda \frac{\partial T}{\partial x_j} dS_j + \frac{\gamma\ Q}{Re_\tau\ Pr}. \tag{4.2.9}$$

For a closed system, another expression can be derived by combining Eq.(4.2.1), Eq.(4.2.3), and Eq.(4.2.4) that constrains the divergence of the velocity field. The velocity field is enforced by the dynamic pressure which becomes clear in the next chapter. The divergence of the velocity field for a closed system is given by,

$$\frac{\partial u_i}{\partial x_i} = \frac{1}{p_0(t)} \left[\frac{-1}{\gamma} \frac{\mathrm{d}p_0}{\mathrm{d}t} + \frac{1}{Re_\tau\ Pr} \int_S \lambda \frac{\partial T}{\partial x_j} dS_j + \frac{Q}{Re_\tau\ Pr} \right]. \tag{4.2.10}$$

This can be verified in the inviscid limit, the thermodynamic pressure remains constant and the velocity is essentially divergence-free.

Note that, the assumption of constant value of $C_p = 1$ has been made to get to Eq .(4.2.8), Eq .(4.2.9) and Eq .(4.2.10). The detailed derivation of these equations is presented in the section A.2.

4.2.1 Thermophysical properties

The thermophysical properties - dynamic viscosity and thermal conductivity - like density, are functions of temperature, and the spatially invariant thermodynamic pressure. The non-dimensional values of dynamic viscosity and thermal conductivity are calculated using Sutherland's law:

$$\mu(T) = T^{3/2} \frac{1 + S_\mu}{T + S_\mu}, \tag{4.2.11}$$

$$\lambda(T) = T^{3/2} \frac{1 + S_\lambda}{T + S_\lambda}, \tag{4.2.12}$$

where $S_\mu = 0.368$ and $S_\lambda = 0.648$ for air at reference temperature of $300K$ and normal pressure.

Sutherland's law provides a general relation for the thermophysical properties of air and were implemented in the setup and tested. However, these relations result in large variations of local friction Reynolds number, and therefore the variable property effects cannot be isolated.

To facilitate this, another set of relations can be described and are also used in the present work. The non-dimensional values of thermal conductivity and dynamic viscosity to ensure minimum variations in local friction Reynolds number are (see, for instance, Patel et al. (2015), for more details),

$$\mu = \sqrt{\rho}, \tag{4.2.13}$$

and likewise,

$$\lambda = \sqrt{\rho}. \tag{4.2.14}$$

In the next chapter, the implementation of these governing equations is discussed along with the different numerical methods that are employed in the present work.

5

Implementation

The governing equations described in the previous chapter are solved to understand the problem of stably-stratified turbulent channel flow in detail. In this chapter, the implementation of these governing equations is discussed. The incompressible Navier-Stokes solver developed by Costa (2018) was adapted to solve the low-Mach number approximation. The original code was modified to accommodate large density variations. A third-order WENO scheme was implemented for convection terms in the energy transport equation to avoid discontinuities and have smooth gradients in the temperature field. A pressure-splitting algorithm was implemented to deal with the variable coefficient Poisson equation. The numerical methods are discussed in detail in the subsequent sections.

5.1 Discretization schemes

The convective and diffusive terms of the momentum equation are discretized in space using a second-order, finite volume scheme. The equations are solved on staggered Cartesian grids, with velocities at face centers and scalars at the cell centers. The diffusion terms of the energy equation are treated the same way as the diffusion terms of the momentum equation, that is, we employ standard second-order finite differences. However, the advection terms of the energy equation are discretized using a third-order WENO scheme. Since we intend to prescribe considerable temperature differences between the walls, it is possible that the derivatives shoot up or become discontinuous. The steep gradients, in some cases, can cause fluctuations in temperature that might yield nonphysical values of temperature. With linear schemes, it is not possible to achieve beyond first-order accuracy in the presence of oscillations. Therefore, it becomes essential to implement a non-linear scheme that is robust and intrinsically handles the discontinuities that may arise due to large fluctuations. WENO is a high-resolution monotone-preserving scheme that uses interpolations from several sub-stencils and weighs them based on their relative smoothness to come up with a suitable approximation of the numerical fluxes. The details of the third-order WENO scheme implemented in the current code are discussed in section B.

The equations are advanced in time using the fully explicit, second-order Adams-Bashforth method. Each new time step, $n+1$, begins with the calculation of the updated temperature as:

$$T^{n+1} = T^n + \frac{\Delta t}{2}\left[3\Psi(T^n) - \Psi(T^{n-1})\right], \tag{5.1.1}$$

where, Ψ contains the convective, diffusive, and source terms of the energy transport equation and is given as:

$$\Psi(T^n) = -\rho^n u_j^n \frac{\partial T^n}{\partial x_j} + \frac{1}{Re_\tau\ Pr}\frac{\partial}{\partial x_j}\left(\lambda^n \frac{\partial T^n}{\partial x_j}\right) + \frac{\gamma - 1}{\gamma}\frac{\mathrm{d}p_0^n}{\mathrm{d}t} + \frac{Q}{Re_\tau\ Pr}. \tag{5.1.2}$$

With the temperature field available for the new time step, the thermodynamic pressure at the new time step, p_0^{n+1}, is calculated using Eq. (4.2.7), and subsequently, the thermodynamic properties are evaluated using Eq. (4.2.4), Eq. (4.2.13) and Eq. (4.2.14), and the rate of change of thermodynamic pressure using Eq. (4.2.9). The thermophysical properties computed at the new time step are available to be used in the momentum equations. Once the temperature field is obtained, and the thermophysical properties are determined, we can proceed to solve for velocity fields.

For computing velocities, we use the fractional-step method or the pressure projection method. We first compute a predicted velocity field using Eq. (4.2.2), but without the pressure gradient terms as:

$$\rho^{n+1}u_i^* = \rho^n u_i^n + \frac{\Delta t}{2}\left[3\Phi(u_i^n) - \Phi(u_i^{n-1})\right], \tag{5.1.3}$$

where,

$$\Phi(u_i^n) = -\rho^n u_j^n \frac{\partial u_i^n}{\partial x_j} + \frac{1}{Re_\tau}\frac{\partial \tau_{ij}^n}{\partial x_j} + \delta_{i,1}. \tag{5.1.4}$$

From the predicted velocity, the corrected velocity can be computed as:

$$u_i^{n+1} = u_i^* - \frac{\Delta t}{\rho^{n+1}}\frac{\partial p^{n+1}}{\partial x_i}. \tag{5.1.5}$$

The pressure field is unknown and needs to be computed to obtain the correct velocity field. This implies that there is one more equation that has not been used yet, the continuity equation. The straightforward approach to solve for pressure field is evaluating the momentum equation in the conservative form and using Eq. (4.2.1) as the constraint, thus yielding a constant coefficient Poisson equation,

$$\nabla^2 p = \frac{1}{\Delta t}\left[\left(\frac{\partial \rho}{\partial t}\right)^{n+1} + \nabla\cdot(\rho\mathbf{u})^*\right]. \tag{5.1.6}$$

The approximate value of $\partial\rho/\partial t$ can be calculated using backward difference methods. This has been previously done by McMurtry et al. (1986), Cook and Riley (1996) and Najm et al. (1998). However, Nicoud (2000) argued that this method does not conserve kinetic energy as the divergence-free constraint is not recovered in the inviscid limit. He also showed that this method is unstable for large temperature variations. Since the goal of the present work is to be able to capture strong gradients in temperature, this method seems unsuitable.

Another approach to solve for the pressure field is using Eq. (4.2.10), which is derived using the continuity equation, to constrain the divergence of velocity. This necessarily means that we are calculating a pressure field that would enforce the divergence constraint on the velocity field. If we take the divergence of the Eq. (5.1.5), we get a variable coefficient Poisson equation that can be solved for dynamic pressure,

$$\frac{\partial}{\partial x_i}\left(\frac{1}{\rho^{n+1}}\frac{\partial p^{n+1}}{\partial x_i}\right) = \frac{1}{\Delta t}\frac{\partial u_i^*}{\partial x_i} - \frac{1}{\Delta t}\frac{\partial u_i^{n+1}}{\partial x_i}, \tag{5.1.7}$$

where, $\partial u_i^{n+1}/\partial x_i$ is substituted by Eq. (4.2.10), and that would ensure that the constraint would be met. However, this would entail solving a variable coefficient Poisson equation as ρ^{n+1} is varying in space.

The variable coefficient Poisson equation is computationally expensive to solve, while, on the other hand, a constant coefficient Poisson equation is not only more convenient but also there are proven and efficient methods available to solve for the same. Hence, it would be ideal to impose the divergence constraint to Eq. (5.1.7) while avoiding solving a variable coefficient Poisson equation. This is achieved using the method proposed by Dong and Shen (2012) and Dodd and Ferrante (2014) in the context of multiphase flows. They put forward a technique in which the variable coefficient is reduced to a constant coefficient Poisson equation, that can be solved efficiently

(e.g., with an FFT-based Poisson solver). Indeed, Demou et al. (2019) used this pressure-splitting approach to solve thermally driven low-Mach flows.

This pressure-splitting method is adapted in the present work and is discussed in detail in the next section.

5.2 Pressure-splitting

Dong and Shen (2012) proposed the idea of splitting the variable density pressure gradient term into a term with a constant coefficient and another with a variable coefficient. Dodd and Ferrante (2014) expanded on the same in their work and verified the method for large density and viscosity ratios. The variable coefficient Poisson equation is transformed to a constant coefficient Poisson equation by means of the following decomposition:

$$\frac{1}{\rho^{n+1}}\frac{\partial p^{n+1}}{\partial x_i} \rightarrow \frac{1}{\rho_*}\frac{\partial p^{n+1}}{\partial x_i} + \left(\frac{1}{\rho^{n+1}} - \frac{1}{\rho_*}\right)\frac{\partial p^*}{\partial x_i}, \tag{5.2.1}$$

where ρ_* is a reference density (this could be any density. In the current code, the minimum density in the domain is used which was also preferred for stability purposes in the references mentioned), p^* is an estimated pressure which is calculated through extrapolation from the previous two time-steps,

$$p^* = \left(1 + \frac{\Delta t^{n+1}}{\Delta t^n}\right)p^n - \left(\frac{\Delta t^{n+1}}{\Delta t^n}\right)p^{n-1}. \tag{5.2.2}$$

This extrapolation of pressure given in the above equation for variable time-steps is specific for Adams-Bashforth time-stepping and the coefficients vary if another time-stepping scheme is to be used. Note that superscripts $n+1$ and n are used for Δt which have not been used in the earlier equations. All the instances in the previous equations correspond to $n+1$ and will do so in the rest of the report unless explicitly mentioned. Also, note that because the pressure is extrapolated, the accuracy of the solution would be affected by the size of the time steps.

By substituting Eq. (5.2.1) in Eq. (5.1.7), we get a constant coefficient Poisson equation for pressure,

$$\frac{\partial^2 p^{n+1}}{\partial x_i^2} = \frac{\rho_*}{\Delta t}\frac{\partial u_i^*}{\partial x_i} - \frac{\rho_*}{\Delta t}\frac{\partial u_i^{n+1}}{\partial x_i} + \frac{\partial}{\partial x_i}\left[\left(1 - \frac{\rho_*}{\rho^{n+1}}\right)\frac{\partial p^*}{\partial x_i}\right]. \tag{5.2.3}$$

The $\partial u_i^{n+1}/\partial x_i$ term in the Poisson equation corresponds to the divergence of the velocity field in the new time step. For incompressible flows, this velocity field is expected to be divergence-free. However, under the low-Mach number approximation the divergence of the velocity field should satisfy Eq. (4.2.10). This condition is derived using the equation of state, the energy transport equation, and the continuity equation as elaborated in A.2. Hence, the divergence of the velocity field at the new time step, $\frac{\partial u_i^{n+1}}{\partial x_i}$, is enforced to satisfy Eq. (4.2.10), and the dynamic pressure calculated from the Poisson equation appropriately corrects the predicted velocity field. The other terms on the RHS of Eq.(5.2.3) are computed using second-order central differences.

The constant coefficients Poisson equation for pressure is solved using FFT based, direct method which is adapted by Costa (2018). Thus the dynamic pressure is evaluated and the correct velocity field is computed with this pressure field.

The decomposed pressure from Eq. (5.2.1) is substituted in Eq. (5.1.5) and the corrected velocity is calculated as:

$$u_i^{n+1} = u_i^* - \frac{\Delta t}{\rho_*}\frac{\partial p^{n+1}}{\partial x_i} - \Delta t\left(\frac{1}{\rho^{n+1}} - \frac{1}{\rho_*}\right)\frac{\partial p^*}{\partial x_i}. \tag{5.2.4}$$

The calculation of corrected velocity marks the completion of one full-time step. The equations are solved in a loop until the steady state is attained.

The numerical method was validated against the cases given by Franck (1998) and Nicoud (2000). Franck (1998) comprises two cases, one with small property variations and another with significant property variations. In this study, the friction Reynolds number at steady state at both walls is considerably different. Nicoud (2000) comprises cases with large property variations, but the thermophysical properties are defined such that the friction Reynolds numbers do not significantly vary locally. This validation is presented in the following section.

5.3 Validation

The numerical method discussed in the previous section is tested by running DNS on turbulent channel flow with variable properties and the results obtained using the present code are validated against the cases which are presented in Franck (1998) and Nicoud (2000).

Direct numerical simulations were conducted on a turbulent channel flow with isothermal walls, where the top wall was maintained at T_2 and the bottom wall at T_1. In Franck (1998), two cases are simulated at temperature ratios of $T_2/T_1 = 1.01,\ 2$ with the thermophysical properties given by Sutherland's law. In Nicoud (2000), three cases corresponding to temperature ratios of $T_2/T_1 = 1.01,\ 2,\ 4$ are compared, and the thermophysical properties are defined as in Eq. (4.2.13) and Eq. (4.2.14).

First, we will compare our results with Franck (1998) in which the thermophysical properties are given by the Sutherland's law. Case A refers to the DNS of turbulent channel flow with $T_2/T_1 = 1.01$ at $Re_\tau = 180$ and Case B refers to the DNS of turbulent channel flow with $T_2/T_1 = 2$ at $Re_\tau = 110$. The comparison of our results with that of Franck (1998) is shown in Fig. 5.1 and Fig. 5.2.

From Fig. 5.1 and Fig. 5.2, we see that the present code validates closely with Franck (1998). However, we can also clearly see that thermophysical properties defined by Sutherland's law result in large variations in the local friction Reynolds number as can be observed in Case B. The friction Reynolds number at the cold wall is significantly larger than that near the hot wall.

To minimize the local variation in the friction Reynolds number, we can use thermophysical properties as defined in Eq. (4.2.13) and Eq. (4.2.14). This relation is used in Nicoud (2000) and the velocity profiles are validated for temperature ratios, $T_2/T_1 = 2,\ 4$, with the results from the present code. Note that since the case of $T_2/T_1 = 1.01$ corresponds to very small variations in properties (temperature acts like a passive scalar) and the velocity profile was validated previously for this case, it will not be validated again. However, the macroscopic quantities yielded in the case are corroborated. The velocity profiles for $T_2/T_1 = 2,\ 4$ are compared in Fig. 5.3 and the macroscopic quantities are validated in Table 5.1,

In Table 5.1, $Re_{\tau,c}$ and $Re_{\tau,c}$ are the friction Reynolds numbers at the cold and hot wall respectively. We can see that the values do not vary a lot from each other. Re_b is the bulk Reynolds number. C_{f1} and C_{f2} are the coefficient of friction at the cold and hot wall respectively. The coefficient of friction is based on the bulk density and maximum velocity. The heat flux parameter is given by $B_q = q_w/\rho_w C_p u_\tau T_w$, where u_τ is the friction velocity, T_w and ρ_w are the wall temperature and the density at the wall, C_p is the heat capacity and q_w is the wall heat flux. The value of this heat flux parameter is calculated at both walls.

From Fig. 5.3, we see a reasonable collapse of the data from the present code with that of Nicoud (2000) and from Table 5.1, we see that the macroscopic quantities calculated from the present code agree very well with ones reported in Nicoud (2000), for turbulent channel flow with isothermal walls and property variations, wherein the local Reynolds number is not significantly different.

From the validations presented above, we can see that the discretization schemes and the numerical method described in the previous section corroborate well with the data from Nicoud (2000), and with confidence, we can proceed to understand the cases of stably stratified turbulent channel flows. In the next chapter, the details of the computational setup and the different DNS

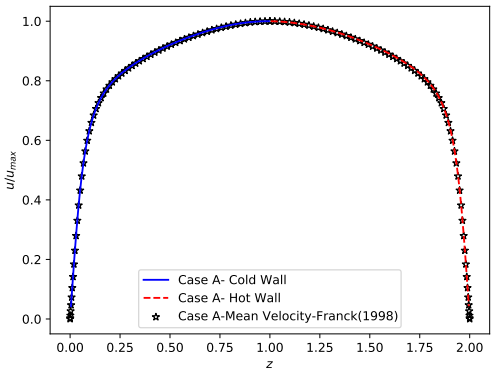

(a) Mean velocity.

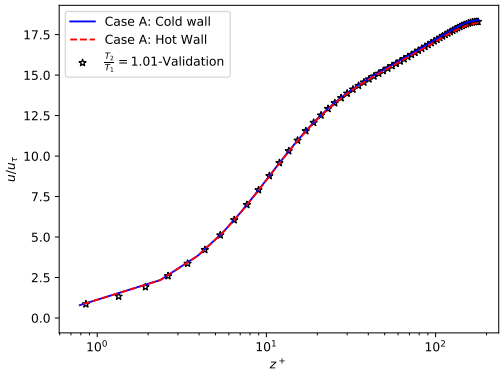

(b) u^+ in wall-units.

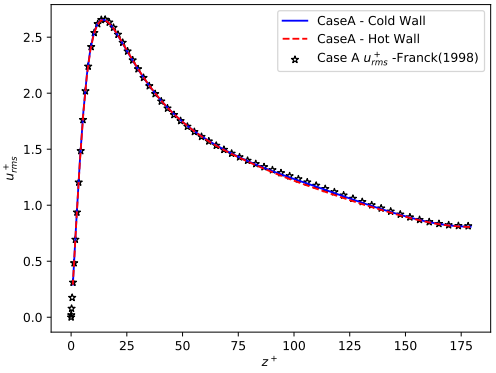

(c) Streamwise velocity fluctutations.

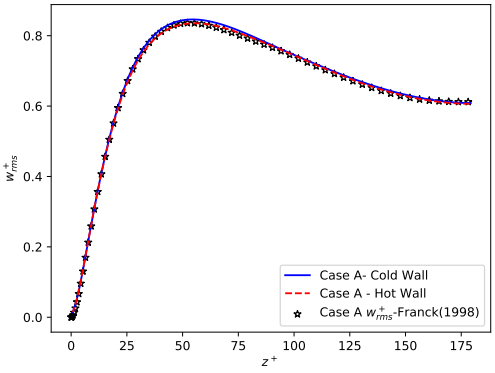

(d) Wall-normal velocity fluctuations.

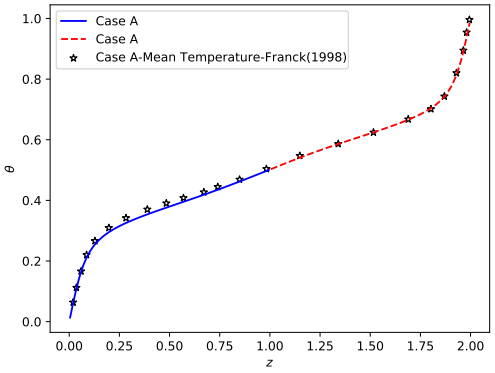

(e) Mean temperature.

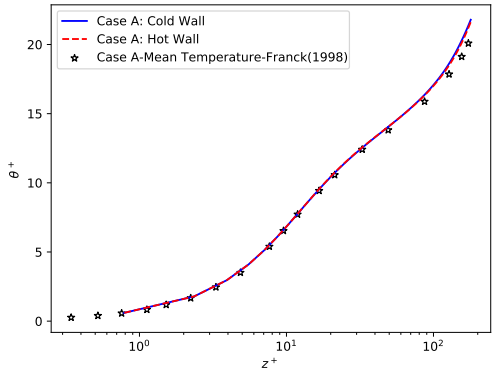

(f) θ^+ in wall-units.

Figure 5.1: Validation of DNS results obtained using the numerical method described in the present work with Franck (1998) for the case $T_2/T_1 = 1.01$. Symbols correspond to data from Franck (1998). Lines correspond to results obtained in the present code- Red lines: Hot wall, Blue lines: Cold wall.

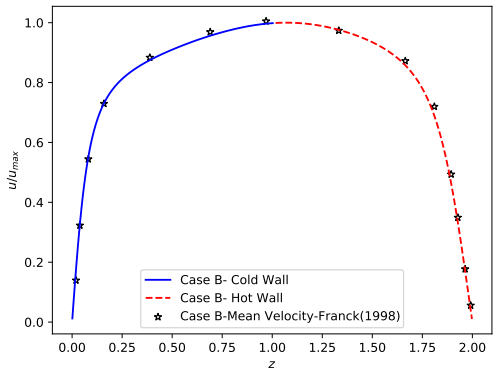

(a) Mean velocity.

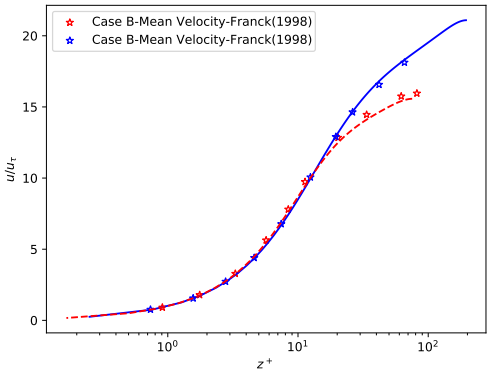

(b) u^+ in wall-units.

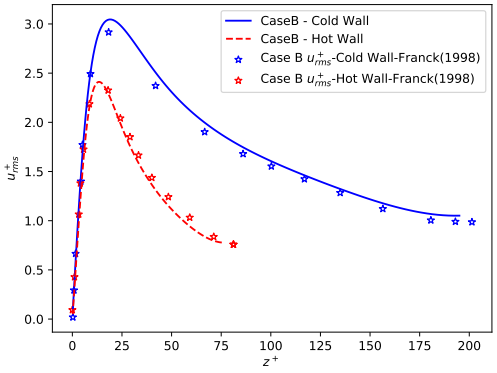

(c) Streamwise velocity fluctuations.

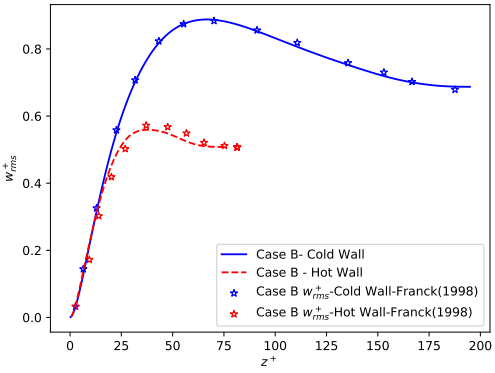

(d) Wall-normal velocity fluctutations.

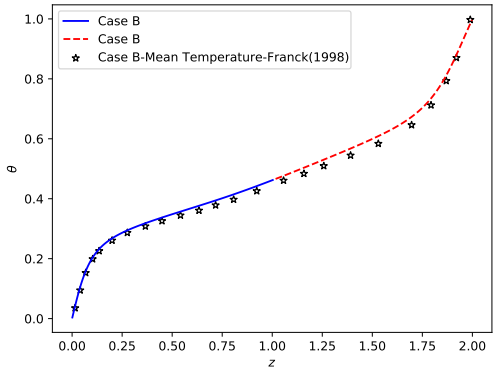

(e) Mean temperature.

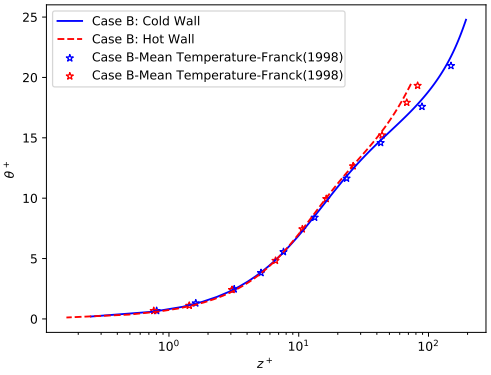

(f) θ^+ in wall-units.

Figure 5.2: Validation of DNS results obtained using the numerical method described in the present work with Franck (1998) for the case $T_2/T_1 = 2$. Symbols correspond to data from Franck (1998). Lines correspond to results obtained in the present code- Red: Hot side, Blue: Cold side.

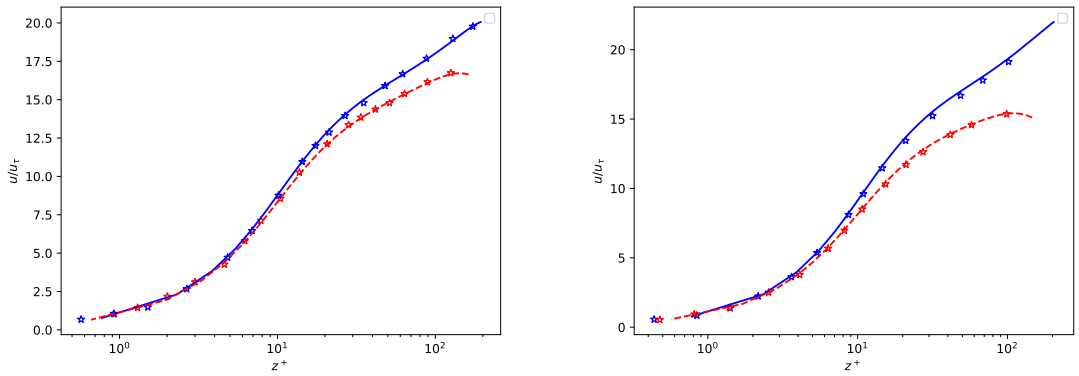

(a) u^+ in wall-units for $T_2/T_1 = 2$.

(b) u^+ in wall-units for $T_2/T_1 = 4$.

Figure 5.3: Validation of DNS results obtained using the numerical method described in the present work with Nicoud (2000) for the case $T_2/T_1 = 2,\ 4$. Symbols correspond to data from Nicoud (2000). Lines correspond to results obtained in the present code- Red: Hot side, Blue: Cold side.

	Case	$Re_{\tau,c}$	$Re_{\tau,h}$	Re_b	$C_{f1} \times 10^3$	$C_{f2} \times 10^3$	B_{q1}	B_{q2}
Present code	$T_2/T_1 = 1.01$	180	180	2827	5.99	5.96	≈ 0	≈ 0
Nicoud (2000)		182	185	2855	6.1	6.1	≈ 0	≈ 0
Present code	$T_2/T_1 = 2$	193	165	2895	6.97	5.07	-0.019	0.014
Nicoud (2000)		195	164	2810	7.0	5.0	-0.018	0.016
Present code	$T_2/T_1 = 4$	202	147	3082	8.00	4.20	-0.043	0.026
Nicoud (2000)		211	151	2818	8.2	4.2	-0.041	0.029

Table 5.1: Validation of macroscopic quantities obtained in the present code with Nicoud (2000). The subscript 1 refers to the cold wall and 2 to the hot wall. C_f is the coefficient of friction based on mean density and maximum velocity. B_q is the heat flux parameter defined as $B_q = q_w/\rho_w C_p u_\tau T_w$

cases of stably stratified turbulent flow simulated in the present work are discussed.

6

Numerical Simulations

The Navier-Stokes equations are solved in the limit of the vanishing Mach number enabling us to account for density variations due to temperature gradients while neglecting acoustic waves. The assumption works in our case of stably stratified turbulent flows as the thermodynamic pressure is almost constant and the changes in density due to pressure are insignificant. In our setup, the walls of the channel are maintained at different temperatures resulting in density gradients in the domain. If density gradients exist in the presence of gravity, we get stratified flow. The present chapter discusses in detail the computational setup and campaign of simulations carried out in order to understand the physics of stably stratified turbulent flows with strong variations in properties.

6.1 Computational details

Stably stratified turbulent flow is simulated in a horizontal straight channel as shown in Fig. 6.1. In the present work, the domain size is kept fixed for all the cases. We perform simulations on a channel whose dimensions are $(L_x \times L_y \times L_z) = (4\pi h \times 4\pi h/3 \times 2h)$, where $L_x,\ L_y,\ L_z$ are lengths of the channel in streamwise, spanwise and wall-normal directions respectively. The grid for all the cases contains $1024 \times 256 \times 240$ cells. In the wall-normal direction, a symmetric grid stretching function with clustering at the walls is used as we do not expect large differences in the local friction Reynolds numbers. The flow is driven by a constant pressure gradient in the streamwise direction, and gravity acts in the wall-normal direction.

The walls of the channel are subjected to Dirichlet boundary conditions such that the temperature gradients are significant. For stable stratification, it is required that the upper wall is at a higher temperature than the lower wall. In the present work, we are looking at temperature ratio, $T_2/T_1 = 2$. The temperatures T_1 and T_2 are given such that $T_1 = T_0 - \Delta T/2$ and $T_2 = T_0 + \Delta T/2$, where T_0 is the reference temperature which is also the mean of the upper and lower wall temperatures. Zonta and Soldati (2018) discussed the limitations of the Oberbeck-Boussinesq approximation and the conditions where it fails to yield accurate results. One of the constraints for the OB approximation to be valid is that $\beta\Delta T < 0.1$. For the temperature boundary conditions that are prescribed in our case, $\beta\Delta T = 0.6667$, implying that we need to be looking beyond the OB approximation. That also justifies the implementation of the low-Mach approximation to compare the results against the OB approximation and understand the effect of density variations on the flow. Note that, because the boundary conditions are not symmetric, we should expect different stresses and heat fluxes at both walls.

In the code, the shear Reynolds number along with reference friction velocity, reference length, and reference density are provided as inputs. The reference friction velocity is calculated as $u_{\tau 0} = \sqrt{-h/\rho_0\ \partial p/\partial x}$, whereas the reference density is calculated at the reference temperature using the

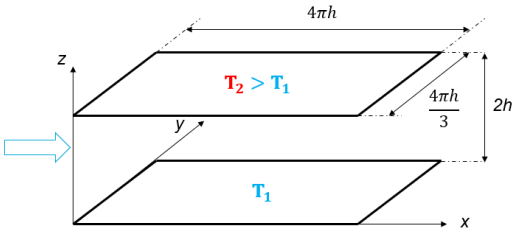

Figure 6.1: Computational domain for the present work.

equation of state and the thermophysical properties are calculated as functions of density such that the friction Reynolds numbers at the hot wall and the cold wall are not very different. These equations, also mentioned in the previous chapter, are stated again for convenience. The equations for density, dynamic viscosity, and thermal conductivity are,

$$\rho = \frac{P_0}{T}, \quad \mu = \rho^{0.5}, \quad \lambda = \rho^{0.5}.$$

The normalized pressure gradient driving the flow is unity. Half-channel height is taken as the reference length. The velocity field is initialized with a fully developed Poiseuille profile and two vortices are triggered at the center of the channel to render the flow turbulent. CFL condition is prescribed to keep a check on the time-step size. This is calculated after comparing time scales for the diffusion of heat and momentum and convection. Periodic boundary conditions are imposed for all velocity components and pressure in the streamwise and spanwise directions. In the wall-normal direction, pressure is bounded by the Neumann boundary condition while the Dirichlet boundary condition, or the no penetration condition, is imposed upon the velocity components. In addition, the magnitude of the acceleration due to gravity is calculated for a given temperature gradient, to impose the required shear Richardson number using Eq. (4.2.5).

The scalar, temperature in this case, is initialized with a linear profile from the top wall, T_2, to the bottom wall, T_1. Periodic boundary conditions are assigned for temperature in the streamwise and spanwise directions, which is the same as that of pressure and velocity. In the wall-normal direction, the walls are assigned fixed values of temperature, which need to be specified as an input in addition to the Prandtl number. The thermophysical properties are calculated for the initial temperature profile using Eq. (4.2.4), Eq. (4.2.13), and Eq. (4.2.14). Thermophysical properties are defined such that the local values of Re_τ are not very different from the initial values of Re_τ anywhere in the domain. This allows us to isolate the effects of variable inertia on the flow.

6.2 Cases

A total of 10 cases corresponding to weakly/moderately stratified turbulent flows are simulated at $Re_{\tau 0} = 180$ and $Pr = 0.76$. The simulations are carried out in a channel with isothermal walls, where the top wall is maintained at T_2 and the bottom wall at T_1. In the present work, we explore temperature ratios $T_2/T_1 = 1.01,\ 2,\ 4$ using the low-Mach approximation. The cases with $T_2/T_1 = 1.01$ are grouped together as Case A and cases with $T_2/T_1 = 2$ are classified as Case B. Four simulations corresponding to $Ri_\tau = 0,\ 18,\ 36,\ 60$ were carried out for both, Case A and Case B. In addition, towards the end two more simulations corresponding to $Ri_\tau = 0,\ 18$ were carried out for $T_2/T_1 = 4$, which are labeled as Case C. Due to the paucity of time, only two simulations could be performed at a temperature ratio of 4.

Only the results of Cases A and B are analyzed in this thesis and the results of Case C are presented in the appendix. The $T_2/T_1 = 1.01$ case serves as the representative case for the Boussinesq approximation as it has very small fluctuations in density. The cases at higher temperature ratios are compared to this case to identify the effects of variable properties. At different temperature ratios, the simulations are carried out for a range of Richardson numbers, $Ri_\tau = 0,\ 18,\ 36,\ 60$. The neutrally buoyant cases have already been validated with Nicoud (2000) in the previous section. Simulations were also carried out at higher Ri_τ, but the laminar pockets were large enough

to engulf the entire domain in these cases. The domain was too small for sustained turbulence, and therefore the flow just laminarized in the entire domain. Indeed, a larger domain would facilitate the sustained turbulence (Garcia-Villalba and Del Alamo, 2011), but in the present work, the domain size is kept uniform across cases. The different cases are summarised in Table 6.1 which also presents the global quantities obtained from the simulations. It should be noted that at higher temperature ratios the property variations result in different friction Reynolds numbers at both walls. Furthermore, it also results in unequal values of shear stress at both walls. The Nusselt number corresponds to the average Nusselt number between the walls. However, even that would be different at both the walls which is discussed in greater detail in Table 7.3. In effect, the thermophysical property variations cause enhancement of turbulence near the cold wall and deterioration of turbulence near the hot wall.

Case	TR	Ri_τ	$Re_{\tau,c}$	$Re_{\tau,h}$	Re_b	Ri_b	$C_{f,c}$e3	$C_{f,h}$e3	Nu
A0	$T_2/T_1 = 1.01$	0	180	180	2823	0	8.15	8.09	6.28
A1		18	180	180	3048	0.031	6.99	6.95	4.24
A2		36	180	180	3225	0.056	6.25	6.21	3.45
A3		60	180	180	3456	0.081	5.46	5.38	2.91
B0	$T_2/T_1 = 2$	0	194	166	2708	0	9.50	6.96	6.29
B1		18	196	165	2937	0.032	8.16	5.74	4.34
B2		36	195	167	3124	0.057	7.18	5.28	3.58
B3		60	191	170	3348	0.083	6.20	4.72	3.07
C0	$T_2/T_1 = 4$	0	210	153	3010	0	11.06	5.82	6.11
C1		18	215	151	3895	0.035	8.04	4.23	4.41

Table 6.1: Macroscopic quantities obtained from the simulations for different cases. The subscript h indicates the value at the hot wall and c indicates at the cold wall. C_f is the coefficient of friction based on the bulk velocity and bulk density. Nu is the Nusselt number. The simulations are performed on a domain of size $L_x \times L_y \times L_z$, which is $4\pi h \times 4\pi h/3 \times 2h$. The grid contains $1024 \times 256 \times 240$ cells.

As DNS requires resolution of even the smallest scales of the flow, we should ensure that the grid used for the study is capable of it. For our cases, since $Pr \approx 1$, the smallest scale in the flow is given by the Kolmogorov scale, or by the viscous wall length scale. In Table. 6.2, the smallest grid-spacing, along different axes, with respect to the viscous length scale is presented. From the table, it is clear that the wall-normal grid-spacing is small enough to resolve the smallest eddies in the flow.

The neutrally buoyant case is initialized with a Poiseuille field with linear temperature profile. But for the case of $Ri_\tau = 18$, the steady-state velocity and temperature fields of the $Ri_\tau = 0$ case are used as initial conditions. This allows for shorter transient and faster convergence to the steady state. Similarly, the cases of successively higher Ri_τ are initialized with the steady-state fields computed for the case with the closest Ri_τ.

6.3 Transient evolution of the flow

Since the flow is driven by a constant pressure gradient, the flow evolves to attain a steady state mean velocity or the target values of Ri_τ and Re_τ. In our case, we track the mean velocity of the flow until it reaches a steady state value. The evolution of bulk velocity in time for different sub-cases in Case B is shown in Fig. 6.2. Alternatively, one could also monitor shear stress on the walls as an indicator of a steady state. As the pressure gradient driving the flow is kept constant, we can deduce from the force balance on the channel that the shear stress at the walls in a steady state has to approach a constant value.

Case	TR	$(\Delta x)_c^+$	$(\Delta y)_c^+$	$(\Delta z)_c^+$	$(\Delta x)_h^+$	$(\Delta y)_h^+$	$(\Delta z)_h^+$
A0	$T_2/T_1 = 1.01$	2.112	2.816	0.786	2.104	2.801	0.784
A1		2.112	2.816	0.786	2.106	2.808	0.784
A2		2.113	2.818	0.787	2.106	2.807	0.784
A3		2.118	2.824	0.789	2.100	2.801	0.784
B0	$T_2/T_1 = 2$	2.279	3.038	0.778	1.945	2.593	0.664
B1		2.298	3.064	0.784	1.938	2.585	0.662
B2		2.282	3.043	0.779	1.959	2.611	0.669
B3		2.285	3.046	0.780	1.979	2.637	0.675
C0	$T_2/T_1 = 4$	2.457	3.276	0.806	1.778	2.371	0.584
C1		2.511	3.348	0.824	1.769	2.359	0.581

Table 6.2: Mesh details with respect to the viscous length scale at both walls. The viscous length scale at the cold wall is given as $\delta_{v,c} = \mu_c/\rho_c u_{\tau,c}$, and a similar definition can be applied to obtain the viscous length scale at the hot wall.

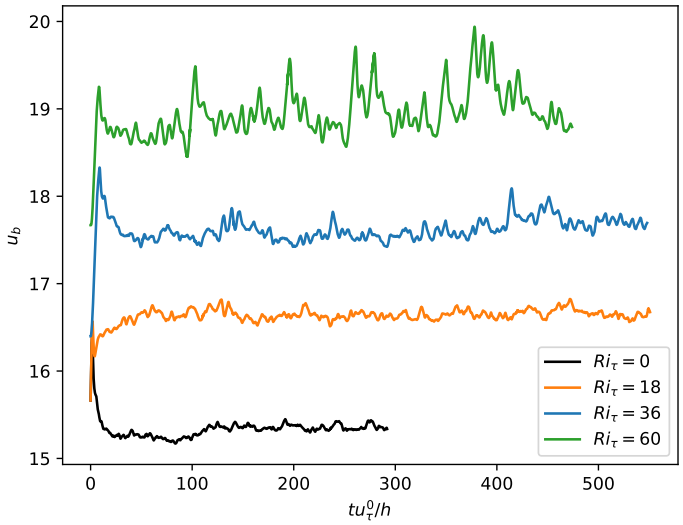

Figure 6.2: Evolution of mean velocity with time for different Richardson numbers for Case B.

As the stratification grows stronger, it becomes increasingly unfavorable for the disturbances to persist in the flow and the flow tends to revert back to a stable, laminar state. Therefore it is reasonable to think that the evolution of these flows is accompanied by random spots of relaminarization (Armenio and Sarkar, 2002; Garcia-Villalba and Del Alamo, 2011). The flow accelerates and the turbulence is restored when gravity is not very strong. However, if the laminar spots are large enough to envelop the entire domain then the flow is completely laminarized and there is little or no scope for retaining the turbulent state. This has been observed by the authors previously at relatively higher Richardson numbers when performing simulations in smaller computational domains. Garg et al. (2000) observed complete relaminarization of flow at $Ri_\tau \geq 45$ whereas Garcia-Villalba and Del Alamo (2011) in their DNS runs observed substantial oscillations of global quantities at $Ri_\tau = 60$. These studies were carried out using the Boussinesq approximation.

In our simulations, from Fig. 6.2 it is apparent that the $Ri_\tau = 60$ case has bursts in the mean velocity during the evolution. This is because large regions in the domain are relaminarizing and

at very small disturbances turbulence is restored. From the results, it was also observed that the $Ri_\tau = 60$ case underwent relaminarization in parts in regular intervals of around 100 eddy turnover times. This was an issue as the relaminarization affected the time averages significantly. It is possible that the cases pertaining to the other two Richardson numbers also undergo periodic relaminarization but the frequency is too small to bear an effect on the long-time averages or to be captured in our simulations.

In addition to the small computational box, the fact that our simulations are carried out at $Re_\tau = 180$ could also be a factor. The turbulent flow prescribed by this friction Reynolds number does not necessarily have a significant separation of scales. As a result, it is a possibility that the buoyancy forces damp the velocity fluctuations locally in the logarithmic region forming a laminar patch. But, owing to the proximity to the wall, this patch is perturbed by the turbulent eddies, and turbulence is recovered. This process continues, resulting in oscillations of global quantities.

7

Results

Stably stratified turbulent flows are marked by the interaction between turbulence in the flow and the buoyancy forces. These forces cause local laminarization of flow thus impacting the heat and momentum transfer rates. In this study, we try and understand wall-bounded stably stratified turbulent flows beyond the Oberbeck-Boussinesq assumptions, that is, in the presence of strong variations in density. The governing equations describing the flow and their implementation were discussed in the preceding chapters. In this chapter, the flow structure and statistics obtained in the present work at different levels of stratification, for different temperature ratios between walls, are compared. The results for the $T_2/T_1 = 1.01$ case are used as a proxy for the Boussinesq approximation and are compared with the results of cases corresponding to higher temperature ratios. This facilitates the isolation of variable inertia effects on the flow. In the next section, we look at the qualitative behavior of the flow. And subsequently, compare the flow statistics for the different cases covered in the present work.

7.1 Qualitative description of the flow

The contours of instantaneous velocity and temperature distributions on a $x - z$ cross-section of the channel located at $y = L_y/2$ are shown in Fig. 7.1, Fig. 7.2, Fig. 7.3 and Fig. 7.4. The direction of the mean flow is from left to right. Firstly, we have contours corresponding to the case of $T_2/T_1 = 1.01$. This case is representative of the Boussinesq approximation as the variations in density are small and can be neglected. And then the instantaneous contours for the case of $T_2/T_1 = 2$ are presented. In this case, the density gradients are strong and cannot be neglected. In this section, we will qualitatively analyze the effects of varying temperature ratios between walls and also the effect of increasing Richardson numbers on the flow structure.

The instantaneous temperature contours are shown in Fig. 7.1 and Fig. 7.2. At $Ri_\tau = 0$, the neutrally buoyant case, we see that the temperature is well-mixed in the entire domain. In neutrally buoyant flows, the inertia forces are unopposed and the eddies traverse the entire height of the channel unconstrained, resulting in greater mixing. With increasing Richardson numbers, the inertia forces are no longer unopposed. They are countered by the buoyancy forces in case of stable stratification. The local behavior of the flow is determined by the relative magnitudes of these forces. In the near-wall region of stratified flows, mechanical shear overpowers the buoyancy. Hence, the eddies in this region contribute to mixing, and we see that the structure of the flow resembles that of the neutrally buoyant case. Away from the walls, the shear weakens and the buoyancy forces start to dominate the inertial forces. The vertical motion of the eddies in this region is damped, as gravity acts as an additional constraint. This is because the eddies move across density gradients in the presence of gravity, and consequently their kinetic energy is converted to potential energy resulting in hindered mixing in the vertical direction. It is apparent that an interface develops, in a way, splitting the channel into an upper half and a lower half. The upper half corresponds to the

hot region and the lower half to the cold region. The temperature appears to be homogeneously distributed in each of the halves separately, with a sharp transition at the interface. The interface, where temperature gradients are sharper than anywhere else in the domain, is called a thermocline. As density is a function of temperature, the density gradients are also strong in this region. This facilitates the initiation of internal gravity waves (IGWs) which is discussed in section 7.3. The interface comprises stable layers of fluid of different densities. Stability implies that the denser fluid layers lie below the layers of the lighter fluid. When the wall-normal velocity fluctuations disturb these layers by carrying a fluid particle to another layer, a restoring buoyancy force acts to bring this particle back to its equilibrium position. This forces the particle back towards its initial position even before the temperature is diffused to the surrounding fluid. The particle overshoots due to its inertia, thus resulting in a kind of oscillatory motion or the IGWs. The interface, made up of these waves, acts as an obstruction to the movement of eddies. The eddies cannot penetrate through the interface but only scour the interface on either side. Thus limiting the mixing across the interface.

On comparing the $T_2/T_1 = 1.01$ case with $T_2/T_1 = 2$ case, we notice that the thermocline is shifted toward the hot wall for the $T_2/T_1 = 2$ case. When the temperature difference between the walls is significant, and the thermophysical properties are functions of temperature, we can expect a disparity between the shear stress at the top and the bottom walls and the deviation of the point of zero stress away from the center of the channel due to the variations in density and dynamic viscosity. For the case $T_2/T_1 = 2$, the shear stress at the cold wall is greater than at the hot wall because of the higher viscosity of the fluid at the cold wall and therefore the interface is located further away from the cold wall. In the $T_2/T_1 = 1.01$ case, the profiles are symmetric. The stress at both walls is almost equal because the temperature difference is too small to cause variations in thermophysical properties. In either case, the region of zero stress corresponds to the region with maximum velocity which is evident from Fig. 7.3 and Fig. 7.4. It can be seen from the instantaneous velocity contours that, just like temperature, the mixing of momentum also diminishes with the increasing Richardson numbers and we see larger gradients of velocity. As a result, the mean velocity increases in the central region for increasing Richardson numbers. Aside from the shifting of the thermocline, we do not see any significant differences in the instantaneous contours of the OB and NOB cases. The turbulence structure close to the walls, far away from the interface, remains more or less similar in both sets of simulations.

In summary, from the instantaneous velocity and temperature contours, one can identify that the mixing, especially in the vertical direction, deteriorates in stably stratified turbulent flows. A thick interface (thermocline) is formed separating the hot and cold sides and the position of the interface varies when the temperature ratio between the walls is significant enough to cause variations in the thermophysical properties of the flow. The interface is made up of internal gravity waves. Reduced mixing, formation of the thermocline, and the IGWs are some of the characteristics of stably stratified turbulent flows. In the next section, we will compare the flow statistics obtained for the $T_2/T_1 = 1.01$ case and the $T_2/T_1 = 2$ case. $T_2/T_1 = 1.01$ corresponds to the case with negligible variations in thermophysical properties, like the assumptions made in Boussinesq approximation, while the $T_2/T_1 = 2$ has significant variations in density, viscosity and thermal conductivity that need to be accounted for accurate prediction of the flow field. This comparison would facilitate us to understand the effects of variation of thermophysical properties on stably stratified turbulent flows.

7.2 Fluid velocity and temperature statistics

The velocity and temperature profiles are presented in two parts. In the first part, we compare the statistics for a given Richardson number at different temperature ratios. Thus we get an idea of the effects of variable inertia by comparing the $T_2/T_1 = 2$ case with that of $T_2/T_1 = 1.01$ case, which closely represents the Boussinesq approximation. In the second part, we compare the statistics at different Richardson numbers for a given temperature ratio and understand the buoyancy effects on the flow at different levels of stratification.

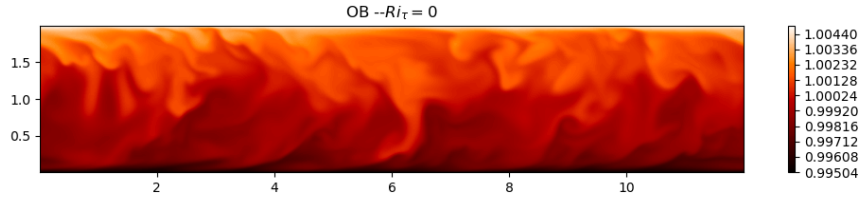

(a) $Ri_\tau = 0$ at $T_2/T_1 = 1.01$.

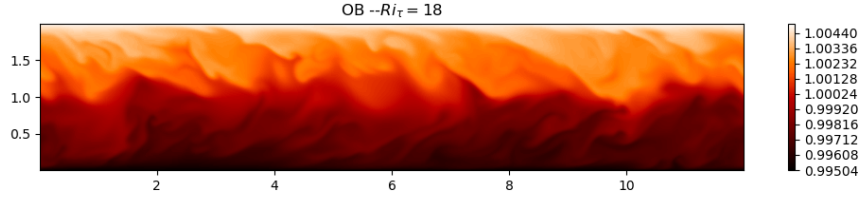

(b) $Ri_\tau = 18$ at $T_2/T_1 = 1.01$.

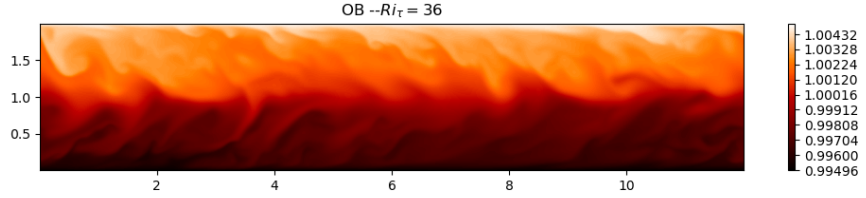

(c) $Ri_\tau = 36$ at $T_2/T_1 = 1.01$.

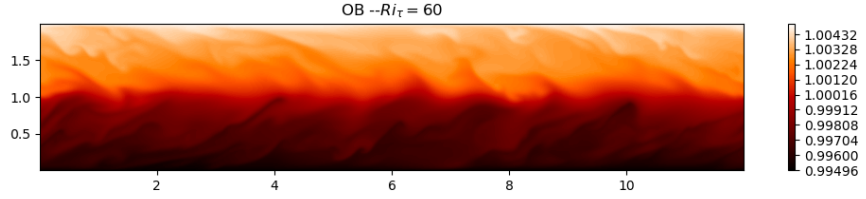

(d) $Ri_\tau = 60$ at $T_2/T_1 = 1.01$.

Figure 7.1: Instantaneous temperature contours on a $x - z$ cross-section of the channel located at $y = L_y/2$. The results correspond to Case A. (*a*) $Ri_\tau = 0$. (*b*) $Ri_\tau = 18$. (*c*) $Ri_\tau = 36$. (*d*) $Ri_\tau = 60$.

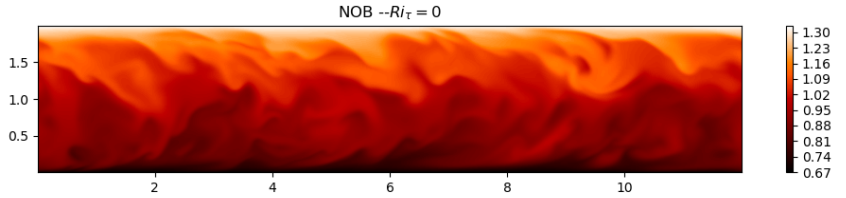

(a) $Ri_\tau = 0$ at $T_2/T_1 = 2$.

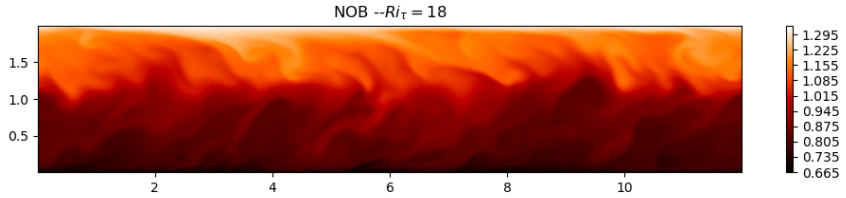

(b) $Ri_\tau = 18$ at $T_2/T_1 = 2$.

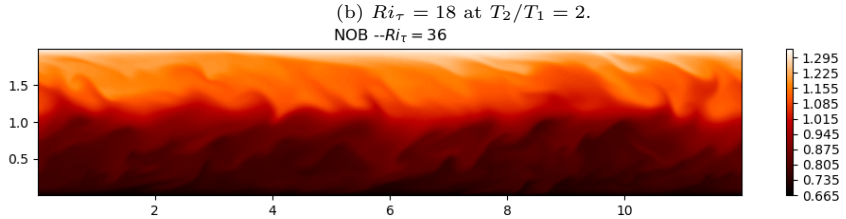

(c) $Ri_\tau = 36$ at $T_2/T_1 = 2$.

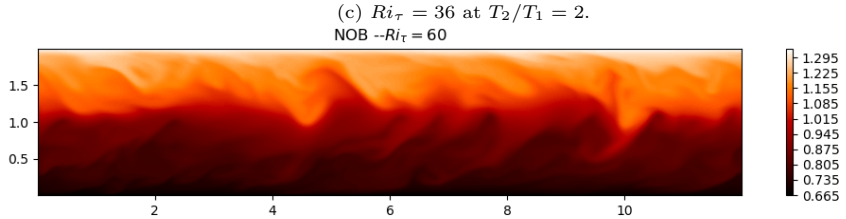

(d) $Ri_\tau = 60$ at $T_2/T_1 = 2$.

Figure 7.2: Instantaneous temperature contours on a $x-z$ cross-section of the channel located at $y = L_y/2$ for Case B. (*a*) $Ri_\tau = 0$. (*b*) $Ri_\tau = 18$. (*c*) $Ri_\tau = 36$. (*d*) $Ri_\tau = 60$.

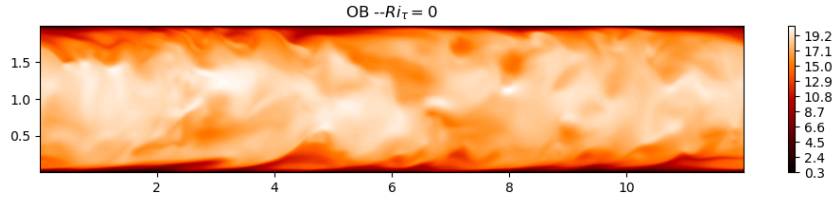

(a) $Ri_\tau = 0$ at $T_2/T_1 = 1.01$.

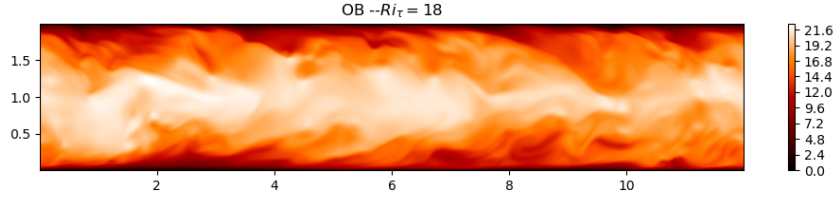

(b) $Ri_\tau = 18$ at $T_2/T_1 = 1.01$.

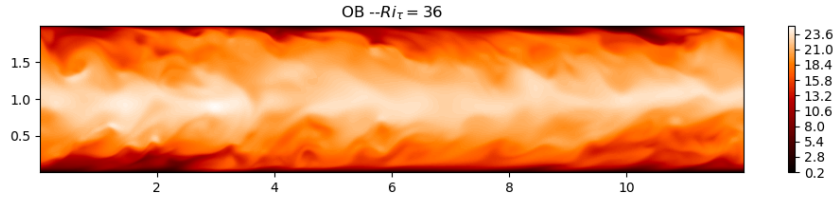

(c) $Ri_\tau = 36$ at $T_2/T_1 = 1.01$.

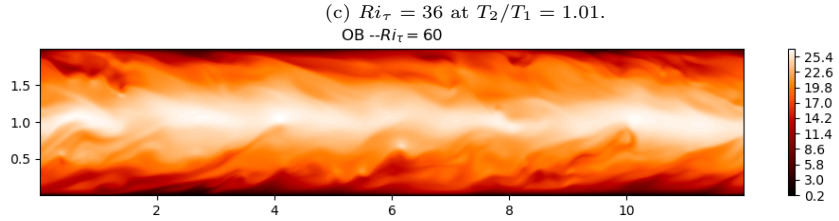

(d) $Ri_\tau = 60$ at $T_2/T_1 = 1.01$.

Figure 7.3: Instantaneous velocity contours on a $x - z$ cross-section of the channel located at $y = L_y/2$ for Case A. (a) $Ri_\tau = 0$. (b) $Ri_\tau = 18$. (c) $Ri_\tau = 36$. (d) $Ri_\tau = 60$.

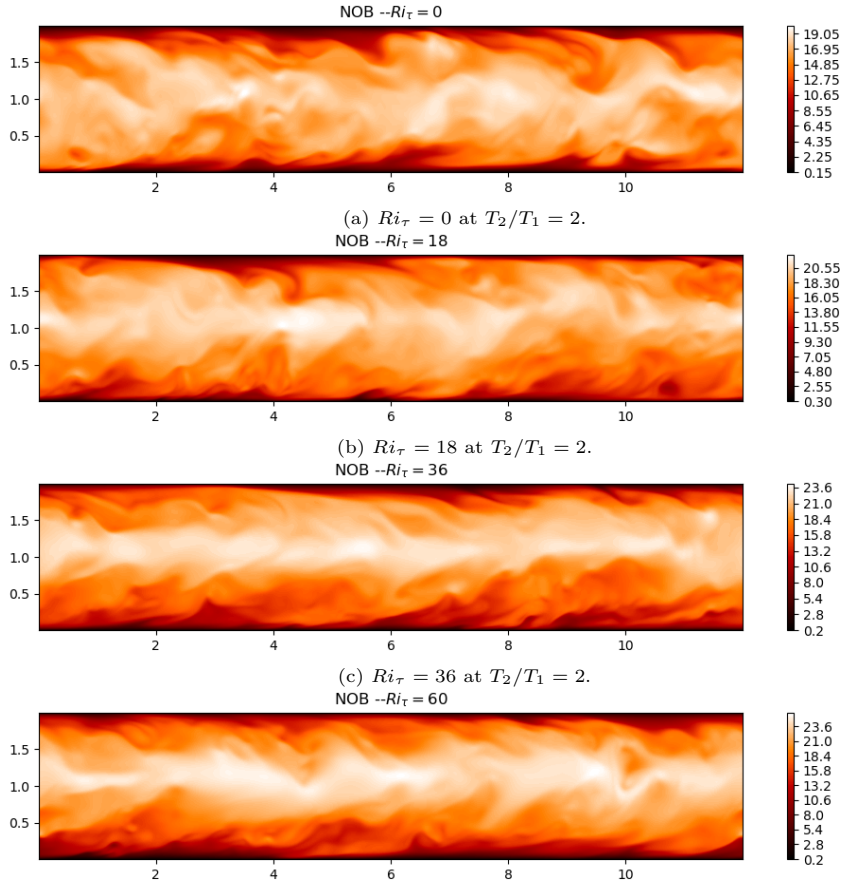

(a) $Ri_\tau = 0$ at $T_2/T_1 = 2$.

(b) $Ri_\tau = 18$ at $T_2/T_1 = 2$.

(c) $Ri_\tau = 36$ at $T_2/T_1 = 2$.

(d) $Ri_\tau = 60$ at $T_2/T_1 = 2$.

Figure 7.4: Instantaneous velocity contours on a $x - z$ cross-section of the channel located at $y = L_y/2$ for Case B. (*a*) $Ri_\tau = 0$. (*b*) $Ri_\tau = 18$. (*c*) $Ri_\tau = 36$. (*d*) $Ri_\tau = 60$.

7.2.1 Case A vs. Case B

We will first compare the flow statistics between two cases, one in which there are little or no property variations and another with considerable variations in thermophysical properties. We present these comparisons at different Richardson numbers to see if the effect of property variations is impacted by the Richardson numbers. In almost all the plots, unless explicitly mentioned otherwise, the results corresponding to the $T_2/T_1 = 1.01$ case (Case A) are given by dotted lines, and that of $T_2/T_1 = 2$ (Case B) are represented by solid lines. The Richardson numbers are distinguished by the color of the lines with the neutrally buoyant case given by black. Orange, blue, and green indicate $Ri_\tau = 18,\ 36,\ 60$ respectively.

The normalized mean temperature profiles comparing cases A0 and B0 are shown in Fig. 7.6b. The temperature is normalized as $\theta = (T - T_1)/(T_2 - T_1)$ and is averaged over time and in homogeneous directions. T_1 is the temperature at the lower wall and T_2 at the upper wall. For case B0, we see that the temperature gradient at the hot wall increases and at the cold wall decreases so as to compensate for the distribution of thermal conductivity of the fluid which is a function of temperature. Thermal conductivity values are higher at the cold wall and therefore we observe a smaller gradient at the cold wall than at the hot wall. In accordance with the temperature profiles, near the cold wall, we have fluid of high density and high dynamic viscosity than near the hot wall, as the properties are related as per the Eq.(4.2.13) and Eq.(4.2.14).

From Table. 6.1, we see that the Reynolds number at the walls in Case B is varying slightly with increasing Richardson numbers which is not observed in Case A. This is the effect of the variation in thermophysical properties. The temperature gradients at the wall are changing with increasing Richardson numbers. But this change, in Case A, is limited to the energy transport equation as the temperature is almost a passive scalar. However, in Case B, the changes in temperature profile affect the momentum equation as density and dynamic viscosity are functions of temperature. The variation of density and dynamic viscosity in the hot and cold sides of the channel for both cases is shown in Fig. 7.5, where they are plotted as a function of y^+.

The mean velocity profiles ($\overline{u}^+$) over the whole channel height z, comparing cases A0 and B0 are shown in Fig. 7.6a. The arithmetic mean of the friction velocity, $u_\tau = (u_{\tau,c}+u_{\tau,h})/2$, is used for normalization. The mean velocity profile for Case A0 ($T_2/T_1 = 1.01$, $Ri_\tau = 0$) is symmetric about the geometric center of the channel. On the other hand, for Case B0 ($T_2/T_1 = 2$, $Ri_\tau = 0$), the temperature fluctuations are significant to induce variations in thermophysical properties. Since the temperature boundary conditions are asymmetric, it is reflected in the mean velocity profile as well. The lower values of dynamic viscosity and density on the hot side of the channel explain the slightly steeper gradients of velocity and higher mean velocity in the region. A similar but opposite argument can be made for the cold side. It is important to note that, even though we observe a higher strain rate at the hot wall, we can confirm from Table. 6.1 that $Re_{\tau,c}$ is actually greater than $Re_{\tau,h}$ indicating that the flow is more turbulent at the cold wall. This is in line with the observations of Zonta et al. (2012a).

We can also compare cases A and B at higher Richardson numbers. The effect of variable properties observed for the neutrally buoyant case is also observed for different Richardson numbers, as shown in Fig. 7.6. From the figures, it can be observed that the trends described for $Ri_\tau = 0$ persist at $Ri_\tau = 18,\ 36,\ 60$.

The variance of the velocity fluctuations, normalized by the arithmetic mean of the friction velocity, for Case A and Case B, are compared in Fig. 7.7 and Fig. 7.8. In Fig. 7.7. The scaled streamwise velocity fluctuation values for the two cases collapse over each other near the wall for neutrally buoyant flows. Near the core, the collapse is not achieved as the velocity in the region no longer scales with the friction velocity. In addition, the effects of stratification also come into the picture in this region. It is evident that the property variations do have an effect on the flow. It would be interesting to plot these profiles taking into account these effects. This would enable us to lump all the effects due to property variations thereby isolating the other remaining effects on the flow. This is possible if we plot semi-locally scaled values.

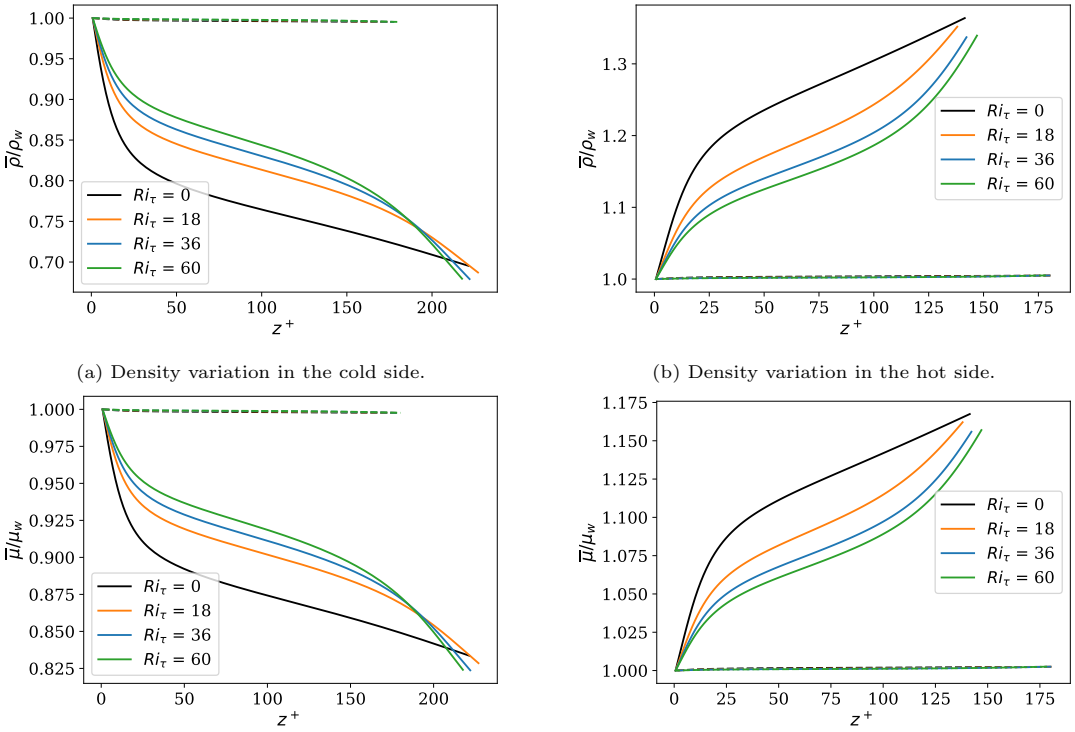

(a) Density variation in the cold side.

(b) Density variation in the hot side.

(c) Viscosity variation in the cold side.

(d) Viscosity variation in the hot side.

Figure 7.5: Variation of density and dynamic viscosity in the hot and cold sides of the channel for Case A and Case B at $Ri_\tau = 0,\ 18,\ 36,\ 60$. The values are normalized with the values at the respective walls. The solid lines correspond to Case B and the dashed lines to Case A. (a, b) show variation of density at the cold and hot walls respectively. (c, d) show variation of dynamic viscosity at the cold and hot walls respectively.

Semi-local scaling is different from classical scaling in the sense that we do not define the characteristic scales with the properties at the wall but instead use the local properties to define the characteristic scales. The semi-local scale for friction velocity is given as $u_\tau^* = \sqrt{\tau_w/\overline{\rho}}$, and the semi-locally scaled wall-normal coordinate is $z^* = \overline{\rho} u_\tau^* z/\overline{\mu}$. The semi-local Reynolds number is defined as $Re_\tau^* = \overline{\rho} u_\tau^* h/\overline{\mu}$. Note that, half channel height is used in the definition of friction Reynolds number despite hot and cold sub-channels being separated asymmetrically. The reader is referred to Patel et al. (2015) for a detailed description of semi-local scaling. The semi-locally scaled fluctuation values are shown in Fig. 7.8, and we see a collapse for the neutrally buoyant case at both walls up to $z^* = 50$ wall units.

On increasing Richardson numbers, we see that the peak for streamwise velocity fluctuations near the hot wall increases slightly for Case B in Fig. 7.7. However, this trend is not seen in Fig. 7.8. Instead, we observe that the semi-locally scaled profiles of streamwise velocity fluctuations still collapse up to $z^* = 50$ wall units even at higher Richardson numbers. This implies that the difference observed in Fig. 7.7 is due to property variations and accounting for these variations would render the difference imperceptible. In the central region of the channel, we observe a similar dip in streamwise velocity fluctuations for both cases. In summary, for Case A and Case B, the effects of stratification on streamwise velocity fluctuations are identical.

The variations of wall-normal and spanwise velocity fluctuations are also presented in Fig. 7.7 and Fig. 7.8. We see the manifestation of higher friction Reynolds numbers at the cold wall in the higher values of velocity fluctuations in the region for the neutrally buoyant case. For stratified cases, we see that the disparity between Cases A and B decreases, and for $Ri_\tau = 60$, we see that the profiles almost collapse over the entire length of the channel in Fig. 7.7. However, we do not observe a similar trend in the semi-locally scaled fluctuations shown in Fig. 7.8 and we see almost identical plots across Richardson numbers. This is indicative that the trend observed in Fig. 7.7 is probably a consequence of property variations. Intuitively, this makes sense as shear production dominates the effects of gravity close to the wall. This means that the production of eddies due

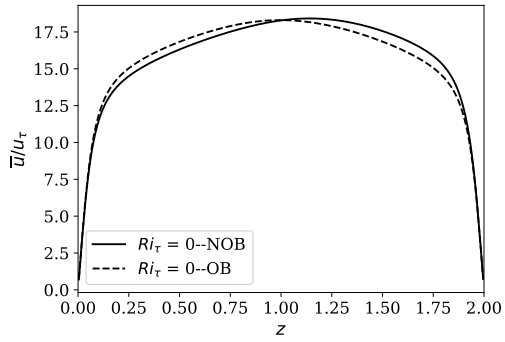

(a) Mean velocity profile for $Ri_\tau = 0$.

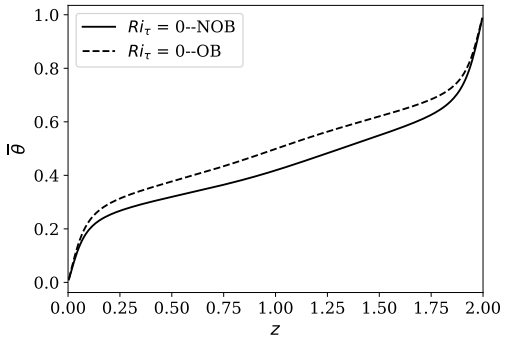

(b) Mean temperature profile for $Ri_\tau = 0$.

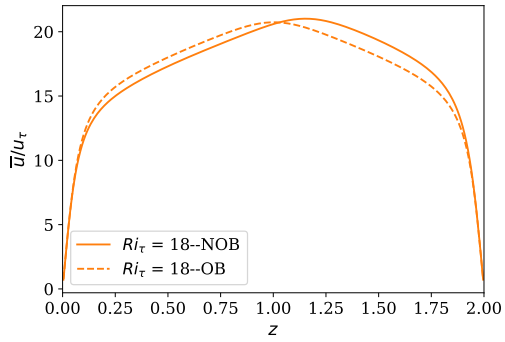

(c) Mean velocity profile for $Ri_\tau = 18$.

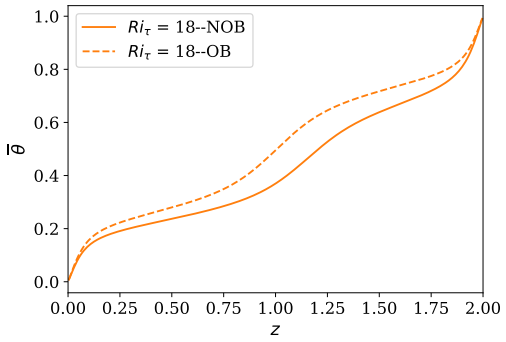

(d) Mean temperature profile for $Ri_\tau = 18$.

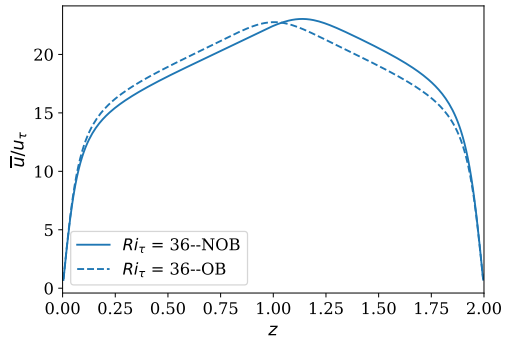

(e) Mean velocity profile for $Ri_\tau = 36$.

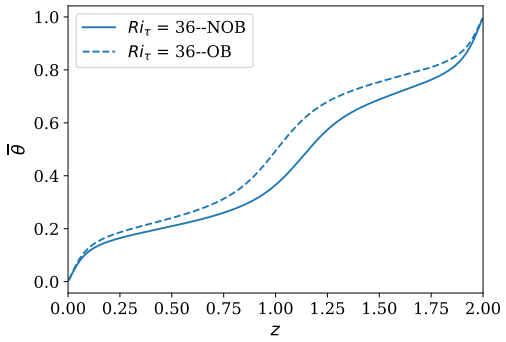

(f) Mean temperature profile for $Ri_\tau = 36$.

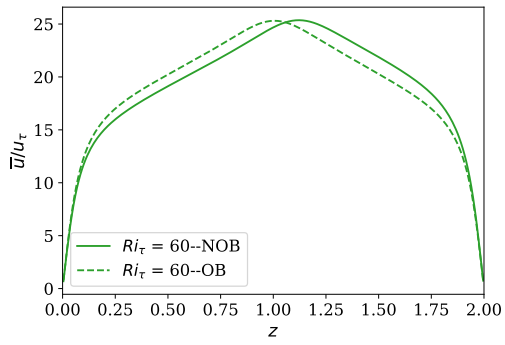

(g) Mean velocity profile for $Ri_\tau = 60$.

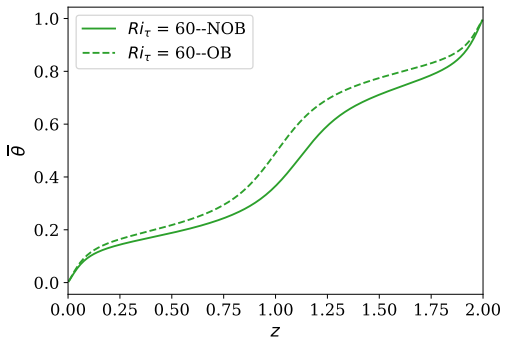

(h) Mean temperature profile for $Ri_\tau = 60$.

Figure 7.6: Mean velocity and mean temperature profiles comparing Cases A and B. Mean velocity profile scaled with average friction velocity and mean temperature profile given in terms of θ, where $\theta = (T - T_1)/(T_2 - T_1)$. OB means representative of the Oberbeck-Boussinesq approximation ($T_2/T_1 = 1.01$) and NOB indicates that the non-Oberbeck-Boussinesq effects are accounted for in the simulations ($T_2/T_1 = 2$). (a, c, e, g) compare the mean velocity profiles and (b, d, f, h) compare the mean temperature profiles for $Ri_\tau = 0, 18, 36, 60$ respectively.

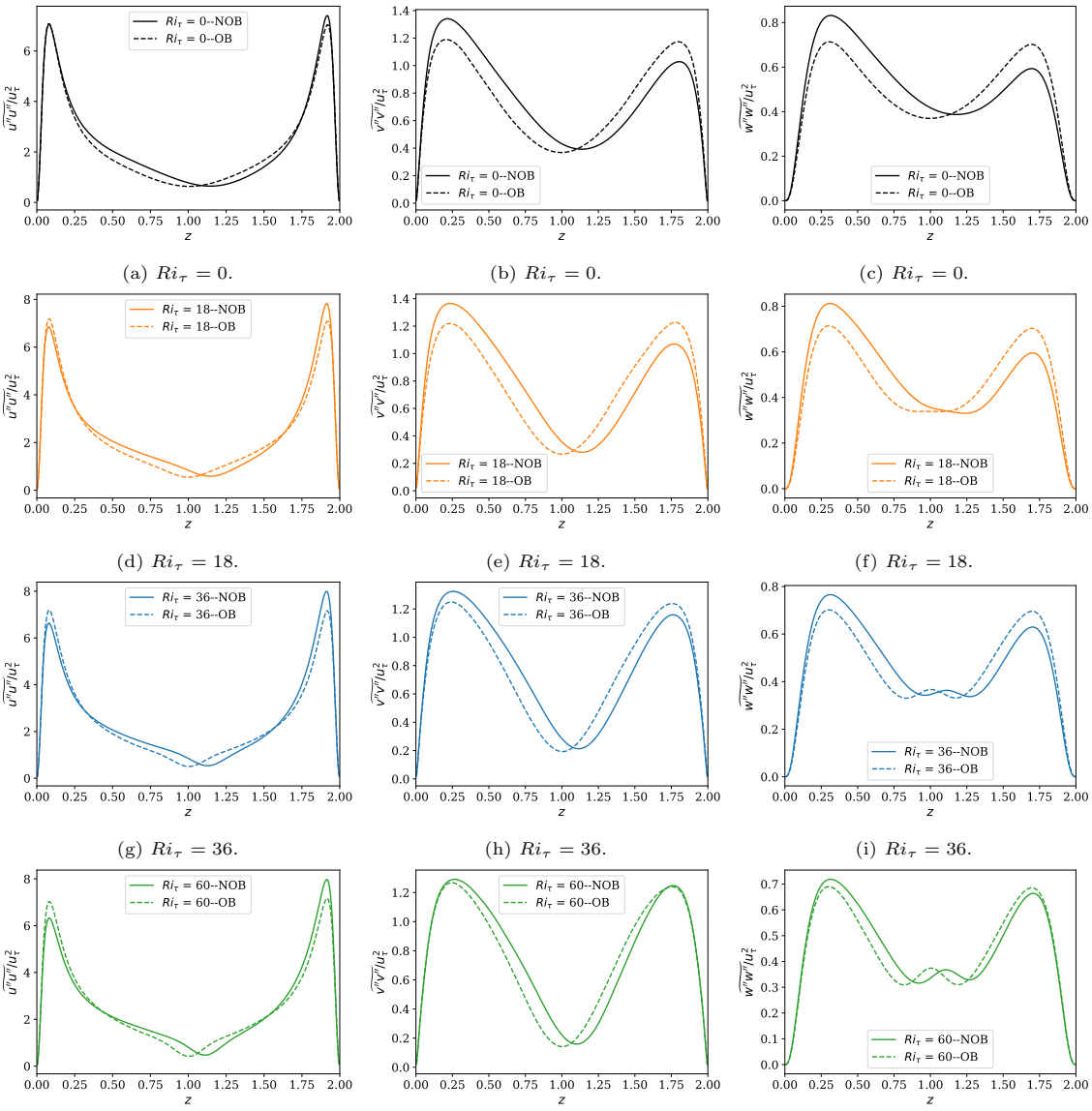

(a) $Ri_\tau = 0$. (b) $Ri_\tau = 0$. (c) $Ri_\tau = 0$.

(d) $Ri_\tau = 18$. (e) $Ri_\tau = 18$. (f) $Ri_\tau = 18$.

(g) $Ri_\tau = 36$. (h) $Ri_\tau = 36$. (i) $Ri_\tau = 36$.

(j) $Ri_\tau = 60$. (k) $Ri_\tau = 60$. (l) $Ri_\tau = 60$.

Figure 7.7: Variance of velocity fluctuations normalized with the square of the arithmetic mean of friction velocity for Cases A and B. OB means representative of the Oberbeck-Boussinesq approximation ($T_2/T_1 = 1.01$) and NOB indicates that the non-Oberbeck-Boussinesq effects are accounted for in the simulations ($T_2/T_1 = 2$). (a, d, g, j) - streamwise velocity fluctuations, (b, e, h, k) - spanwise velocity fluctuations, (c, f, i, l) - wall-normal velocity fluctuations, for $Ri_\tau = 0,\ 18,\ 36,\ 60$ respectively.

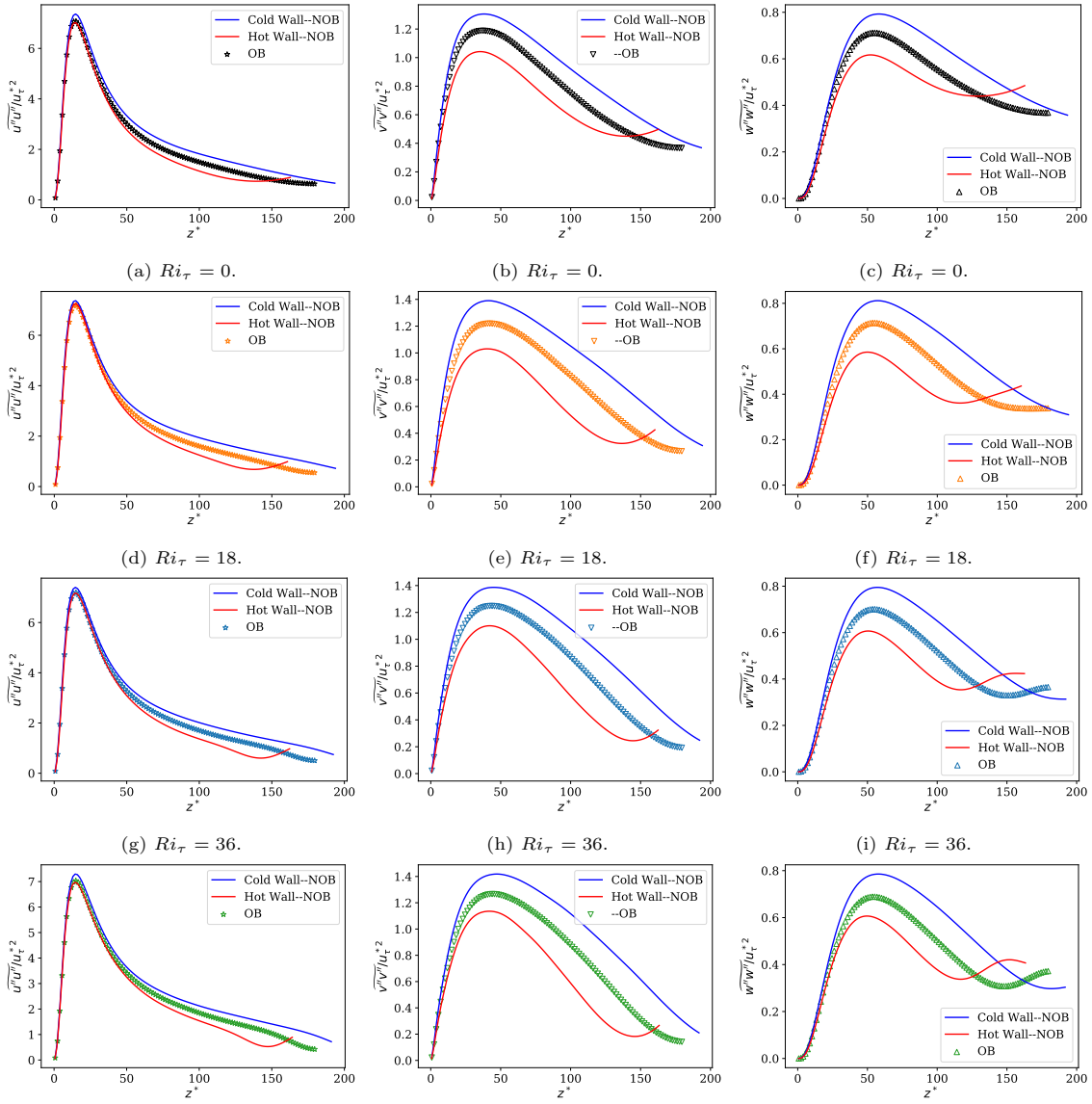

(a) $Ri_\tau = 0$. (b) $Ri_\tau = 0$. (c) $Ri_\tau = 0$.

(d) $Ri_\tau = 18$. (e) $Ri_\tau = 18$. (f) $Ri_\tau = 18$.

(g) $Ri_\tau = 36$. (h) $Ri_\tau = 36$. (i) $Ri_\tau = 36$.

(j) $Ri_\tau = 60$. (k) $Ri_\tau = 60$. (l) $Ri_\tau = 60$.

Figure 7.8: Semi-locally scaled variance of velocity fluctuations comparing Cases A and B. Case A is indicated by symbols. For Case B, hot side (red lines) is scaled with respect to the hot wall and the cold side (blue lines) is scaled with respect to the cold wall. (a, d, g, j) - streamwise velocity fluctuations, (b, e, h, k) - spanwise velocity fluctuations, (c, f, i, l) - wall-normal velocity fluctuations, for $Ri_\tau = 0,\ 18,\ 36,\ 60$ respectively.

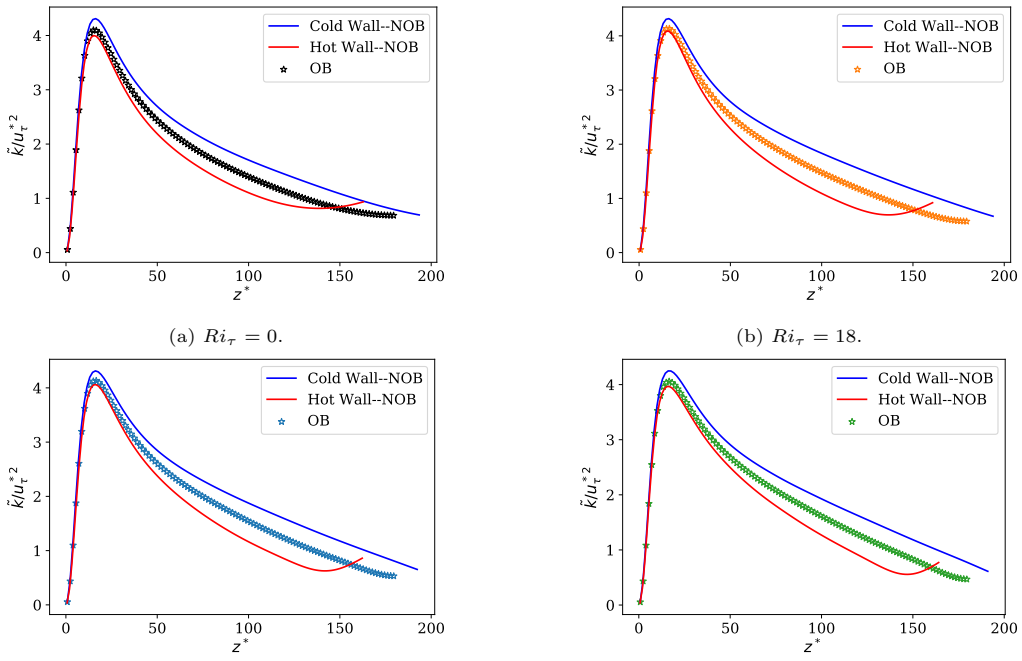

(a) $Ri_\tau = 0$.

(b) $Ri_\tau = 18$.

(c) $Ri_\tau = 36$.

(d) $Ri_\tau = 60$.

Figure 7.9: Turbulent kinetic energy comparing the $T_2/T_1 = 1.01$ case with $T_2/T_1 = 2$ case. Case A is indicated by symbols. For Case B, the cold side (blue lines) is normalised with ${u^*_{\tau,c}}^2$ and the hot side (red lines) with ${u^*_{\tau,h}}^2$. (*a*) $Ri_\tau = 0$. (*b*) $Ri_\tau = 18$. (*c*) $Ri_\tau = 36$. (*d*) $Ri_\tau = 60$.

to mechanical shear is much larger than the dissipation of these eddies by the buoyancy forces in this region. But in the core of the channel, the situation is the opposite and the effects of gravity become more pronounced. In the region where IGWs act, we observe a similar behavior between cases A and B in Fig. 7.7 for both spanwise and wall-normal velocity fluctuations.

We can also compare the turbulent kinetic energy of the constant property case with that of the variable properties. The turbulent kinetic energy is given as $\tilde{k} = \widetilde{u_i'' u_i''}/2$. In Fig. 7.9, the turbulent kinetic energy is normalized with local friction velocity, u^*_τ, and plotted against z^*, which is the wall-normal coordinate normalized with the local viscous length scale. It is not surprising that the turbulent kinetic energy profiles closely resemble the profiles of variance of streamwise velocity fluctuations as it is the dominant component. In the near wall region, we observe that the normalized turbulent kinetic energy on the cold side for Case B (with property variations) seems to have slightly gained over the Case A counterpart, and on the hot side, the effect is the opposite. We can attribute this small difference to the difference in the local Reynolds number in the flow.

The temperature fluctuations, normalized with the temperature difference between the walls, comparing Cases A and B are shown in Fig. 7.10. For the neutrally buoyant case A0, we can observe that the fluctuations are symmetric about the geometric center of the channel. For Case B0, we see that the fluctuations are higher close to the hot wall. This can be explained by the lower friction Reynolds number at the hot wall. Lower $Re_{\tau,h}$ implies that the viscous sub-layer is thicker and therefore the temperature decreases faster near the hot wall than it increases near the cold wall (Nicoud, 2000). We observe a similar trend at higher Richardson numbers as well, wherein the temperature fluctuations are invariably higher at the hot wall than at the cold wall.

One of the significant differences between the constant and variable property cases, Case A and Case B, is the position of the point or the plane of zero stress. In the case of flow with constant properties, the shear stress at both walls is equal and hence we get zero stress at the geometric center of the channel. The equal stresses result in symmetric flow characteristics about exactly the half-channel height (h). However, when the property variations are significant, the shear stress at the hot wall is not the same as that at the cold wall because the density and dynamic viscosity values at both walls are largely different. Thus, zero stress is no longer realized at the geometric center of the channel but is shifted toward one of the walls.

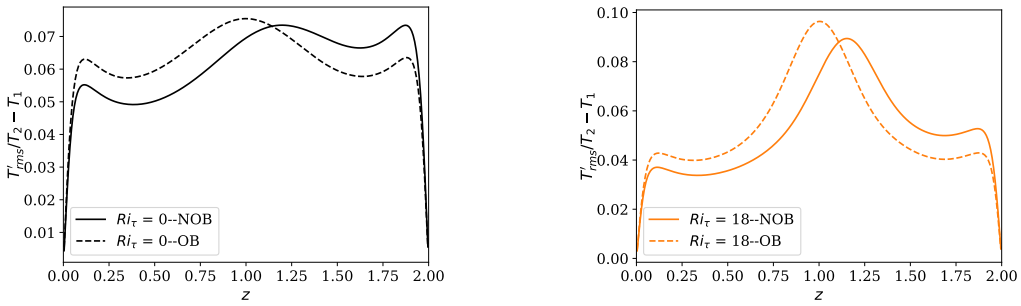

(a) $Ri_\tau = 0$.

(b) $Ri_\tau = 18$.

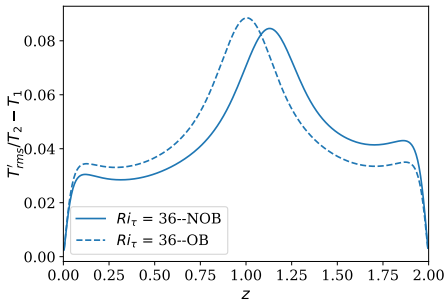

(c) $Ri_\tau = 36$.

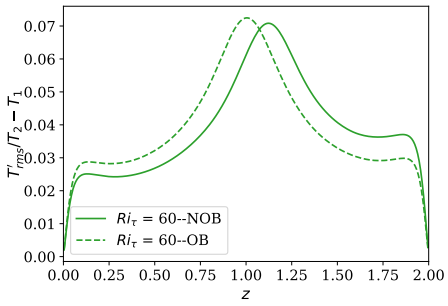

(d) $Ri_\tau = 60$.

Figure 7.10: RMS values of temperature fluctuations for Cases A and B. (*a*) $Ri_\tau = 0$. (*b*) $Ri_\tau = 18$. (*c*) $Ri_\tau = 36$. (*d*) $Ri_\tau = 60$.

The location of the zero-stress from one of the walls (cold wall in this case) can be determined by carrying out a simple force balance on the sub-channel extending from the cold wall ($z = 0$) to the location of zero stress ($z = L^*$). The two forces acting on this control volume are the shear stress, acting at the cold wall, which is balanced by the external pressure gradient that is driving the flow. The shear stress at the cold wall can be expressed as $\tau_c = \rho_c u_{\tau,c}^2$, where ρ_c and $u_{\tau,c}$ are the density of the fluid and friction velocity at the cold wall. We can write the force balance as,

$$\tau_c = -\frac{\partial p}{\partial x} L^* = -\delta_{i,1} L^*. \tag{7.2.1}$$

Since $\partial p/\partial x$ is constant, we see that as shear stress at the cold wall increases, the location of zero-stress shifts away from the cold wall. In the present work, the normalized pressure gradient is equal to unity, and L^* can be determined solely by the properties and velocity gradient at the cold wall.

The distribution of total stress in the wall-normal direction over the entire height of the channel can be evaluated using the averaged streamwise momentum equation. The $x-$momentum equation after averaging is:

$$\frac{\partial \overline{p}}{\partial x} = \frac{\partial \overline{\tau_t}}{\partial z}, \tag{7.2.2}$$

where the total stress $\overline{\tau_t}$ is the sum of Reynolds stress and the viscous shear stress, given as,

$$\overline{\tau_t} = -\overline{\rho u'' w''} + \mu \overline{\frac{\partial u}{\partial z}}. \tag{7.2.3}$$

The variables are decomposed into a Favre mean and Favre fluctuation. For any variable γ, we can write $\gamma = \tilde{\gamma} + \gamma''$, where $\tilde{\gamma} = \overline{\rho\gamma}/\overline{\rho}$ and $\overline{\rho\gamma''} = 0$ but $\overline{\gamma''} \neq 0$. $\tilde{\gamma}$ is the Favre mean and γ'' is the Favre fluctuation. The overline indicates Reynolds averaged quantity.

Integrating Eq. (7.2.2) from 0 to z, for $z < L^*$, gives:

$$\frac{\partial \overline{p}}{\partial x}\, z = \overline{\tau_t}(z) - \rho_c u_{\tau,c}^2. \tag{7.2.4}$$

Note that $\partial\overline{p}/\partial x$ is the normalized pressure gradient driving the flow, which is unity in our case, and if we substitute Eq. (7.2.3) for $\overline{\tau_t}$, we get the distribution of the total stress in the cold sub-channel,

$$1 - \frac{z}{L^*} = \frac{1}{\rho_c u_{\tau,c}^2}\left(-\overline{\rho u'' w''} + \overline{\mu \frac{\partial u}{\partial z}}\right). \tag{7.2.5}$$

We can perform a similar exercise for the hot sub-channel where we integrate Eq. (7.2.3) from z to H, for $L^* < z \leq H$, where H is the total height of the channel. We get,

$$-1 + \frac{\rho_c u_{\tau,c}^2}{\rho_h u_{\tau,h}^2}\,\frac{1}{L^*}\,(H - z) = \frac{1}{\rho_h u_{\tau,h}^2}\left(-\overline{\rho u'' w''} + \overline{\mu \frac{\partial u}{\partial z}}\right). \tag{7.2.6}$$

Note that the linear profile of total stress is retained even in the variable property case, with the minor difference being that the location zero stress is slightly skewed from the center. The stress profiles are plotted against the wall-normal coordinate in Fig. 7.11 to illustrate the shift of zero stress away from the center for the variable property cases. The values for L^* are also tabulated for different cases in Table 7.1.

Case	TR	Ri_τ	L^*
A0	$T_2/T_1 = 1.01$	0	1.00
A1		18	1.00
A2		36	1.00
A3		60	1.01
B0	$T_2/T_1 = 2$	0	1.15
B1		18	1.16
B2		36	1.14
B3		60	1.12

Table 7.1: The distance of the zero stress plane from the cold wall in turbulent channel flows for $Ri_\tau = 0,\ 18,\ 36,\ 60$ at $T_2/T_1 = 1.01$ and $T_2/T_1 = 2$.

The turbulent momentum flux for different cases is plotted using the semi-local scales in Fig. 7.12. The semi-locally scaled plots account for property variations and thus enable us to comment on the flow characteristics arising due to other effects. Unsurprisingly, turbulent momentum flux is invariably larger at the cold wall than at the hot wall in the flow with variable properties, at all Richardson numbers. This is expected as the density of the fluid in this region is higher. Thus implying that the x-momentum flux transported by the wall-normal velocity fluctuations ($\overline{\rho u'' w''}$) towards the cold wall is greater than that towards the hot wall. This results in higher values of Reynolds stress at the cold wall rendering the flow more turbulent in the region. We can also observe that the location of the peak is not altered by changing the Richardson numbers. Therefore, from these observations, it would be reasonable to presume that stratification does not affect turbulent momentum flux in the viscous sub-layer and the buffer layer of the turbulent channel flow. We can see the effects of gravity gradually increasing through the log layer and being the maximum in the core region. In the core region, we observe that the difference between Cases A and B decreases with increasing Richardson numbers, which signifies the effect of gravity in the region.

Along similar lines as the turbulent momentum flux, we also consider the turbulent heat flux in the channel which is given as $-\overline{\rho w'' T''}$. In Fig. 7.13, the variation of turbulent heat flux in the channel is shown as a function of the dimensionless distance z^*. We compare the constant property flows alongside the flows with property variations at different Richardson numbers. For neutrally buoyant flows, we observe that the turbulent heat flux profiles almost collapse over each other. This is expected as the flow is well-mixed and diffusive heat flux is minimum in the interior of the

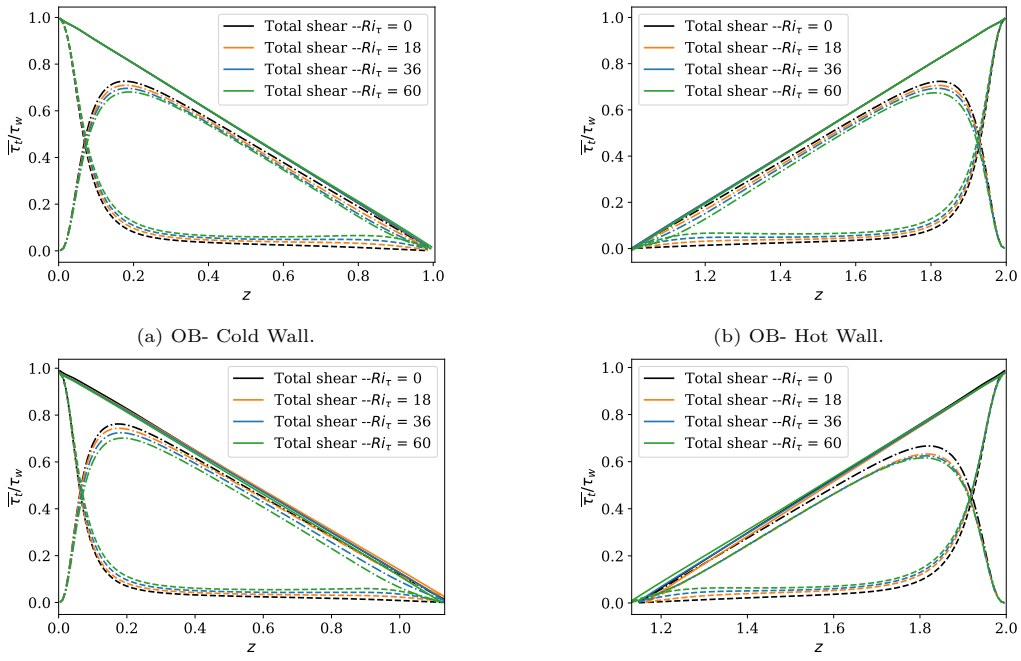

(a) OB- Cold Wall.

(b) OB- Hot Wall.

(c) NOB- Cold Wall.

(d) NOB- Hot Wall.

Figure 7.11: Total stress profile for $Ri_\tau = 0,\ 18,\ 36,\ 60$ to illustrate the shift in the region of zero stress for the $T_2/T_1 = 2$ case in comparison to the $T_2/T_1 = 1.01$ case. The stress is normalized with $\rho_c u^2_{\tau,c}$ in the cold side and with $\rho_h u^2_{\tau,h}$ in the hot side. $--$ is viscous shear stress and $-\cdot-$ is Reynolds stress. (a, b) correspond to Case A at cold and hot wall respectively. (c, d) correspond to Case B at cold and hot wall respectively.

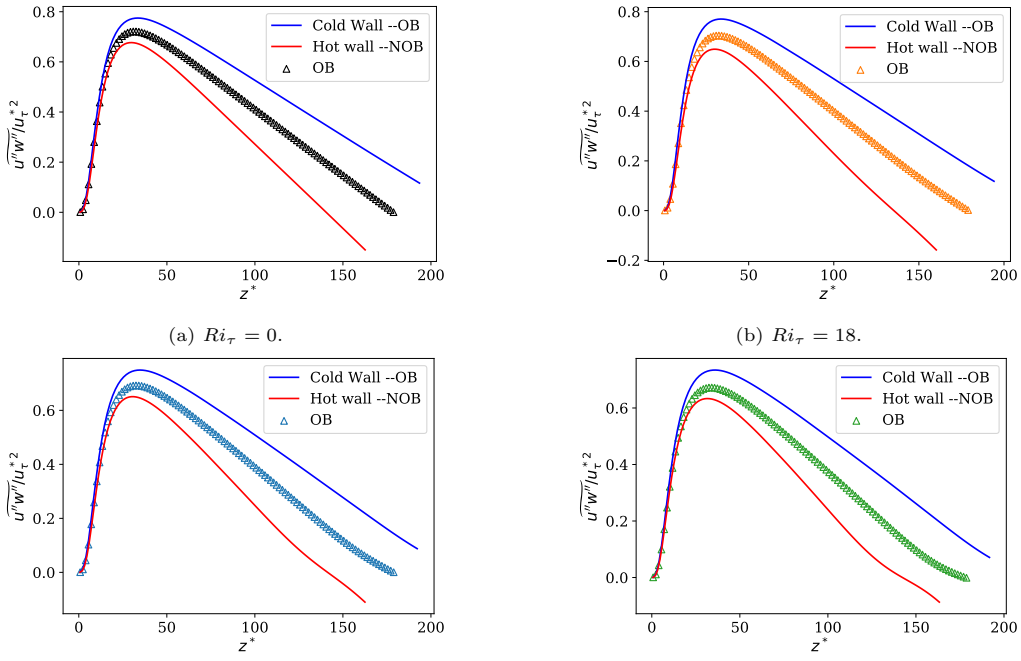

(a) $Ri_\tau = 0$.

(b) $Ri_\tau = 18$.

(c) $Ri_\tau = 36$.

(d) $Ri_\tau = 60$.

Figure 7.12: Variation of semi-locally scaled turbulent momentum flux. Symbols correspond to Case A. Lines (Red - Hot side, Blue - Cold side) correspond to Case B. (a) $Ri_\tau = 0$. (b) $Ri_\tau = 18$. (c) $Ri_\tau = 36$. (d) $Ri_\tau = 60$.

channel. As the stratification increases, a thermocline is developed in the region where buoyancy forces solely influence the flow. In this region, the temperature gradients are large, resulting in an increase in the diffusive flux and a drop in the values of the turbulent heat flux. We see that the normalized turbulent heat flux profiles, at both walls, almost collapse for Case A and Case B in the viscous sub-layer and the buffer layer for all Richardson numbers, reinforcing the idea that

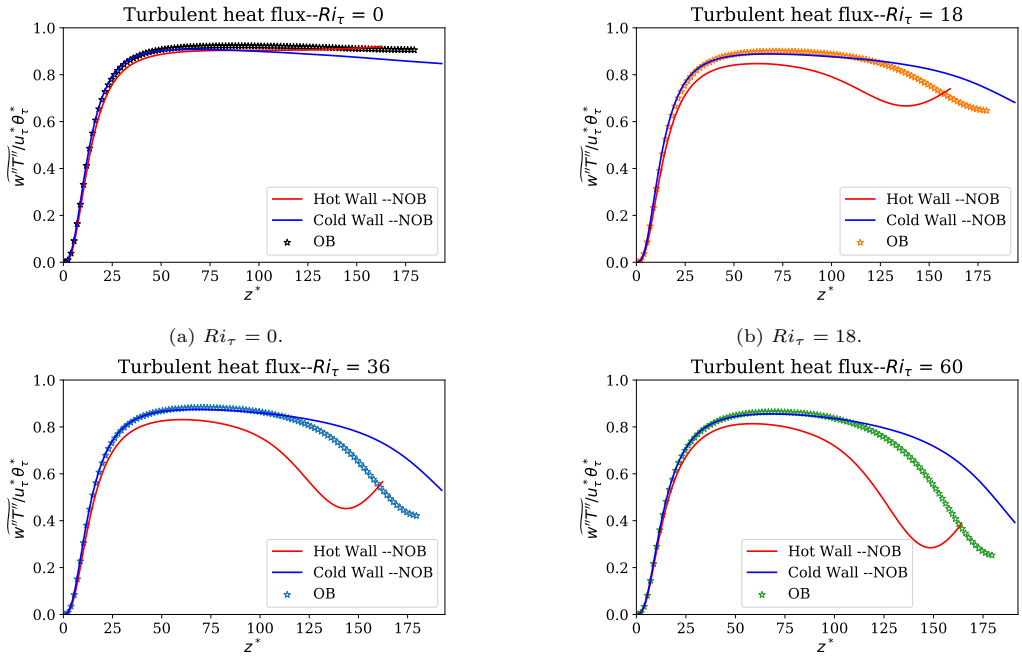

(a) $Ri_\tau = 0$. (b) $Ri_\tau = 18$.

(c) $Ri_\tau = 36$. (d) $Ri_\tau = 60$.

Figure 7.13: Turbulent heat flux for different Richardson numbers. The markers correspond to the constant property case ($T_2/T_1 = 1.01$) and lines to the variable property case ($T_2/T_1 = 2$). Red lines correspond to the flux in the hot region and the blue lines to the cold region of the variable property case. (*a*) $Ri_\tau = 0$. (*b*) $Ri_\tau = 18$. (*c*) $Ri_\tau = 36$. (*d*) $Ri_\tau = 60$.

gravity is ineffective near the walls where mechanical shear is dominant. For flows with constant properties (Case A), we observe the fall-off starting at around $z^* = 125$ wall units from either wall as the flow structure is symmetric at about half-channel height. In flows with variable properties (Case B), we observe that the turbulent heat flux values start to dip closer to the hot wall at about $z^* = 80$ wall units from it. Although the position of the trough varies from Case A to Case B, the amplitude of the troughs is very comparable.

Thus in conclusion, we see that the turbulent channel flows, with and without property variations, retain the typical turbulent characteristics in the vicinity of the walls due to the lack of impact of buoyancy forces on the eddies in this region. As shear becomes less effective away from the walls, we begin to notice the impressions of gravity on turbulent heat flux. The property variations mostly influence the location at which the turbulent heat flux deteriorates but not the effect of stratification itself.

In this section, we compared stably stratified flows with and without property variations. The temperature difference between the top hot wall and the bottom cold wall was increased to ensure that the density fluctuations are considerable. The results were compared to a case in which the density fluctuations are negligible. The effect of buoyancy, to suppress the wall-normal velocity fluctuations in regions of weak shear, was observed to be identical for either of the cases. From the mean velocity profiles, we observed the acceleration in the mean flow is also identical for both cases. The profiles of the variance of velocity fluctuations scaled using local properties showed that the trends observed for neutrally buoyant cases persist even at higher Richardson numbers. Invariably, we observed that the flow near the walls is unaffected by the buoyancy forces. The significant difference in the case with variable properties is that the region of zero stress is shifted toward the hot wall because the combined effects of variation of density and the dynamic viscosity cause friction Reynolds number to be higher on the cold side than on the hot side. As a consequence, although the effect of buoyancy is the same, the site of action of these forces is altered in the case of the flow with variable properties. This was shown in the stress budgets and also in the diminishing of turbulent heat flux in the core region. In the next section, we will closely examine the effect of increasing Richardson numbers on flows with strong property variations.

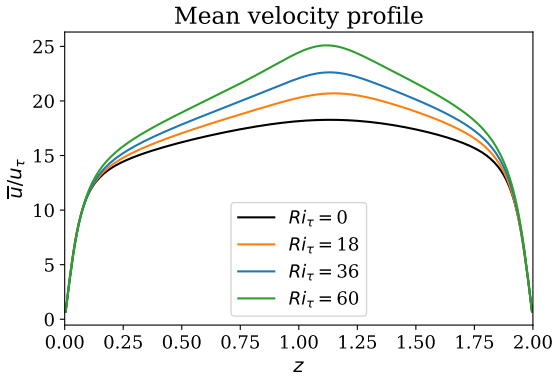

(a) Mean velocity.

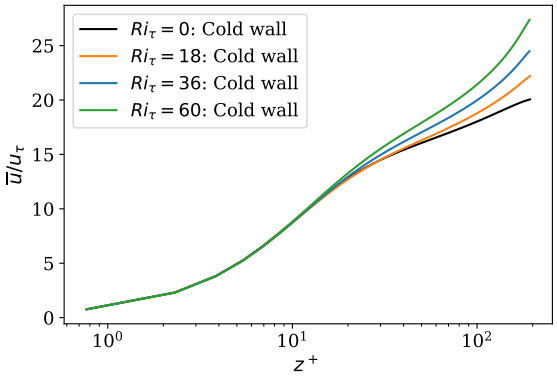

(b) $\overline{u}^+$ in wall-units on the cold side in semi-log scale.

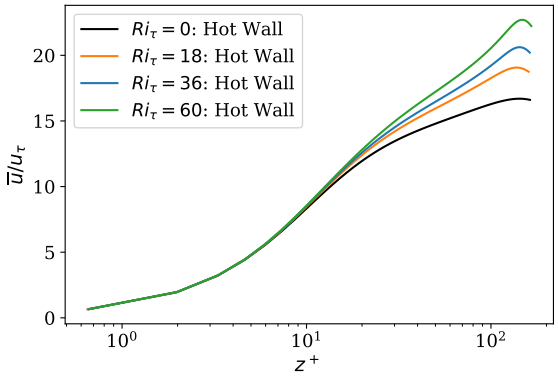

(c) $\overline{u}^+$ in wall-units on the hot side in semi-log scale.

Figure 7.14: (a) - Variation of mean velocity in the entire height of the channel. (b) - Variation of mean velocity in the cold region in wall-units. (c) - Variation of mean velocity in the hot region in wall-units.

7.2.2 Comparison between cases B0, B1, B2 and B3

The temperature ratio, $T_2/T_1 = 2$, between the hot and cold walls induces significant density gradients in the channel. The density fluctuations have to be accounted for to predict accurate flow quantities. The effect of the existence of strong density gradients in the presence of gravity on the mean statistics of the flow will be looked at in this section. The mean velocity profiles ($\overline{u}^+$) as a function of the wall-normal coordinate at different Richardson numbers is shown in Fig. 7.14. The averaging is carried out over time and along homogeneous directions. Reynolds and Favre's averaging is discussed in detail in the appendix. In the current section, the quantities presented are mostly Reynolds averaged unless explicitly mentioned. The results are rendered according to the following color code: black refers to the neutrally buoyant case ($Ri_\tau = 0$), orange corresponds to the case $Ri_\tau = 18$, blue refers to the case $Ri_\tau = 36$ and green to $Ri_\tau = 60$, and all of them are obtained for the channel with the ratio between the temperature at the walls is $T_2/T_1 = 2$.

From Fig. 7.14b and Fig. 7.14c, we can observe that in the inner layer, comprising the viscous sub-layer and the buffer layer (close to around $z^+ = 25$ wall-units), the velocity profiles at different Richardson numbers collapse onto that of the neutrally buoyant case. This is because the eddies in the region are too small to be affected by the buoyancy forces and the flow is dominated by the viscous forces in the region. The friction velocity used for normalization is only based on the viscous forces, which is why we see that the plots at higher Richardson numbers are indistinguishable from that of the neutrally buoyant case in the near-wall region. Away from the walls, however, the mean streamwise velocity increases with the increasing Richardson numbers, and the profiles deviate from that of the neutrally buoyant case. This is a consequence of stratification. In this region, a new velocity scaling needs to be developed which accounts for the effect of the buoyancy forces.

The shear stress contends the action of buoyancy. The buoyant forces are most effective in the core region where the shear is weak, or even absent. The core of the channel, characterized

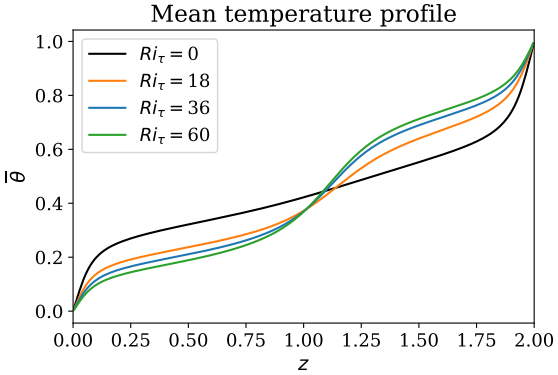

(a) Mean temperature.

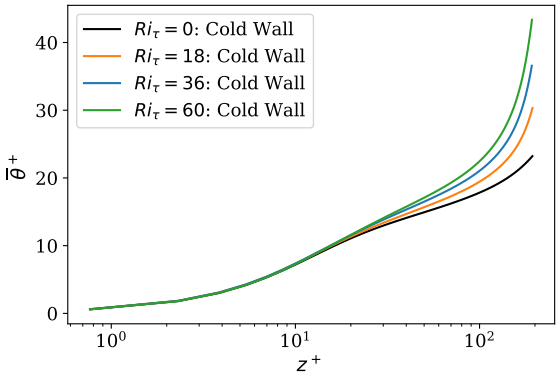

(b) $\overline{\theta}^+$ in wall-units on the cold side in semi-log scale.

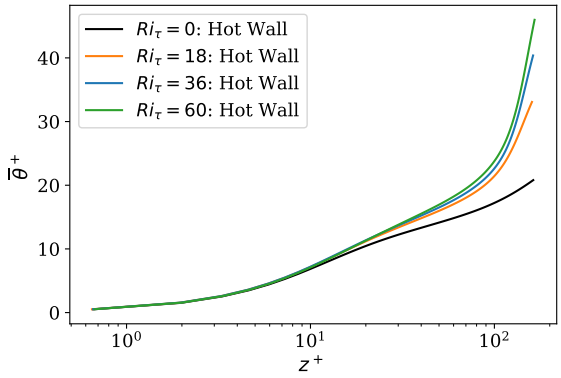

(c) $\overline{\theta}^+$ in wall-units on the hot side in semi-log scale.

Figure 7.15: Mean temperature profiles for $Ri_\tau = 0,\ 18,\ 36,\ 60$ at $T_2/T_1 = 2$. θ is the normalised temperature and is given as $\theta = (T - T_1)/(T_2 - T_1)$.$(a)$ - Variation of mean temperature in the entire height of the channel. (b) - Variation of mean temperature scaled with the friction temperature $\theta_{\tau,c}$ in the cold region in wall-units. (c) - Variation of mean temperature scaled with the friction temperature $\theta_{\tau,h}$ in the hot region in wall-units.

by weak shear, is mostly populated with large eddies that carry significant energy and traverse longer distances. But these eddies need to expend energy to move across density gradients in the presence of gravity. As a result, the turbulent kinetic energy is consumed, and converted to potential energy. Since the buoyancy forces act on these large-scale eddies and suppress the wall-normal velocity fluctuations, Reynolds stresses in the region are reduced. Thus explaining the increase in the mean streamwise velocity with increasing Richardson numbers and also the almost laminar, parabolic shape of the velocity profile(Garcia-Villalba and Del Alamo, 2011).

As the velocity toward the center of the channel increases, due to the dominant buoyancy forces in the region, the velocity gradients also increase. The velocity gradients on the hot side of the channel are higher than on the cold side because the viscosity in the region is lower. This is evident from the mean temperature profiles in Fig. 7.15a where we see the temperature on the hot side increases with increasing Richardson numbers. This corresponds to increasingly lower viscosity values as viscosity is inversely proportional to temperature. Thus, we can explain the mean velocity profiles for increasing Richardson numbers in a channel with variable thermophysical properties.

The mean temperature profiles are shown in Fig. 7.15a. The temperature is normalized as $\theta = (T - T_1)/(T_2 - T_1)$ and is averaged over time and in homogeneous directions. T_1 is the temperature at the lower wall and T_2 at the upper wall. $\overline{\theta}^+$ is $\overline{\theta}$ scaled with the friction temperature, θ_τ, where $\theta_\tau = q_w/\rho_w C_p u_\tau$. $\overline{\theta}^+$ in the cold side of the channel shown in Fig. 7.15b is scaled with the friction temperature at the cold wall, $\theta_{\tau,c} = q_{w,c}/\rho_{w,c} C_p u_{\tau,c}$ and similarly on the hot side, shown in Fig. 7.15c, is scaled with the friction temperature at the hot wall, $\theta_{\tau,h} = q_{w,h}/\rho_{w,h} C_p u_{\tau,h}$. In Fig. 7.15, the temperature is not rescaled in wall units, and the effect of stratification is evident. We observe that the temperature profile, although relatively homogeneous and well-mixed in the cold and hot sides of the channel, the two sides are separated by a region where the temperature changes

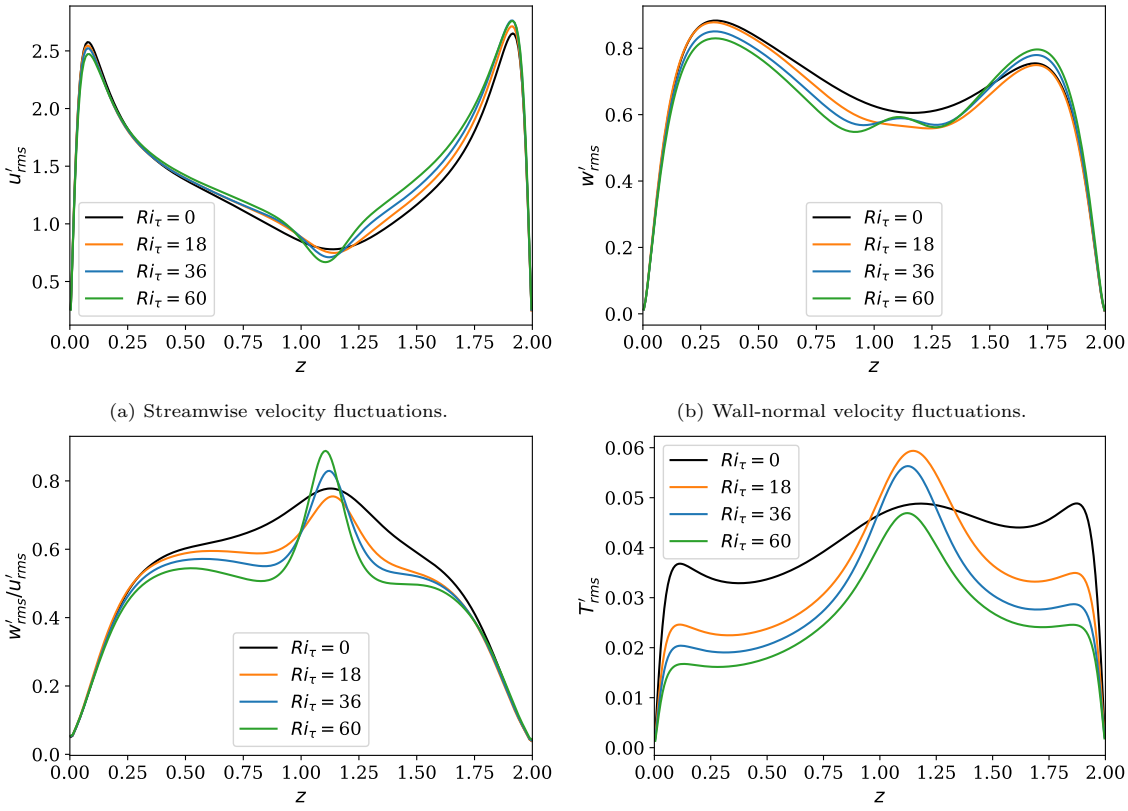

(a) Streamwise velocity fluctuations.

(b) Wall-normal velocity fluctuations.

(c) Ratio of wall-normal to streamwise velocity fluctuations.

(d) RMS of temperature fluctuations.

Figure 7.16: RMS values of temperature fluctuations and velocity fluctuations for $Ri_\tau = 0,\ 18,\ 36,\ 60$ at $T_2/T_1 = 2$. (a) - Streamwise velocity fluctuations. (b) - Wall-normal velocity fluctuations. (c) - Ratio of wall-normal to streamwise velocity fluctuations. (d) - Temperature fluctuations.

rapidly. This layer in which the gradients are much stronger than anywhere else in the domain is called a thermocline. The existence of thermocline is a characteristic of stably stratified turbulent flows (Armenio and Sarkar, 2002; Garcia-Villalba and Del Alamo, 2011). The turbulent eddies in the core are completely suppressed rendering the turbulent heat flux non-existent (Fig. 7.19b). The diffusive flux is the only active component and since the total heat flux in the channel is constant, the diffusive flux in the core has to increase (Fig. 7.19a) resulting in large gradients in temperature in the core region. Thus, explaining the development of the thermocline. As the interface grows, the toll of potential energy that the eddies need to pay increases, only making it harder to penetrate the interface. With the decrease in turbulent flux, the fluid is less well-mixed, as a result of which the heat flux at the walls diminishes and so does the Nusselt number.

The variation of the root mean square of temperature fluctuations is shown in Fig. 7.16d. The fluctuations are significantly lower than the neutrally buoyant case except in the core region where the fluctuations shoot up to values greater than the neutrally buoyant case. However, this overshoot is not the fluctuation per se, but the manifestation of the laminar wavy structures or the internal gravity waves. This can be deduced by the fact that the magnitude of turbulent heat flux (Fig. 7.19b) is considerably lower at the core of the channel even though the temperature fluctuations (Fig. 7.16d) and the wall-normal velocity fluctuations (Fig. 7.16b) by themselves have higher magnitudes. This implies that these fluctuations are decorrelated, that is, the maximum of temperature fluctuations coincide with the zeros of the wall-normal velocity fluctuations and vice versa (Garcia-Villalba and Del Alamo, 2011). This can be explained by the existence of IGWs in the region. The IGWs are discussed in the section 7.3. These waves oscillate in the wall-normal direction. At the crest of the wave, the wall-normal velocity would be zero as it is an extremum, while the local fluctuation of the fluid temperature would be the highest. Thus, we can explain the small values of turbulent heat flux despite large values of wall-normal velocity fluctuations and temperature fluctuations separately, in the core region.

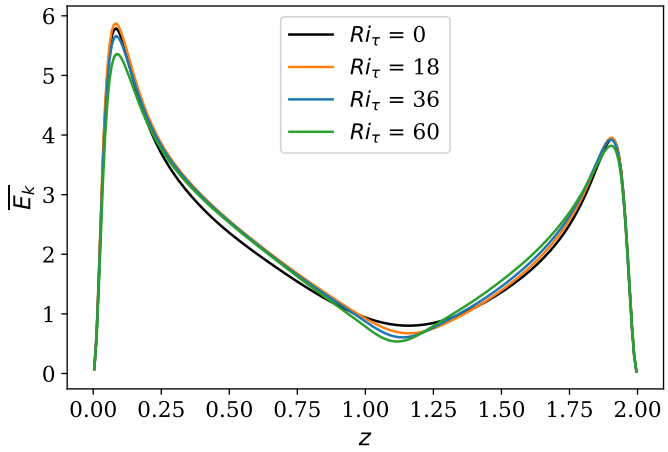

Figure 7.17: TKE intensities for $Ri_\tau = 0,\ 18,\ 36,\ 60$ at $T_2/T_1 = 2$.

The variation of the root mean square of velocity fluctuations is shown in Fig. 7.16. The velocity fluctuations near the wall are mostly unaffected as shear overpowers the buoyancy effects in the region. Away from the wall, we notice deviations from the neutrally buoyant case. The streamwise velocity fluctuations increase as we move away from the wall with increasing Richardson numbers, because the increased mean velocity results in steeper velocity gradients, and dip sharply in the core where turbulence is completely subdued. This trend is consistent in the profiles of turbulent kinetic energy per unit volume ($E_k = \overline{\rho}\tilde{k}$, where $\tilde{k} = \widetilde{u_i'' u_i''}/2$) shown in Fig. 7.17. It is apparent that, in the region away from the walls, and before the IGWs, the turbulence intensity increases with increasing Richardson numbers as the velocity gradients increase. It should also be of no surprise that the intensity of turbulence is higher closer to the cold wall than the hot wall owing to the larger turbulent stress due to the presence of denser fluid in the region.

The wall-normal velocity fluctuations on the other hand decrease farther from the wall, and a local maximum is observed at the core for stratified flows, where the IGWs are anticipated. This local maximum is not observed for neutrally buoyant flows. The decrease in wall-normal velocity fluctuations can be attributed to turbulent kinetic energy being converted to potential energy due to the influence of buoyancy. Fig. 7.16c shows the ratio of wall-normal velocity fluctuations to that of streamwise fluctuations. The ratio indicates the efficiency of energy transfer from the streamwise component to the wall-normal energy component. The ratio is unaffected compared to the neutrally buoyant case near the wall, but we see a stark drop as we move toward the core region indicating the effect of stratification in limiting the interaction between the two fluctuating components (Zonta et al., 2022). Stratification renders the wall-normal component less energetic near the core as the eddies are suppressed.

In the following paragraphs, we will look at the turbulent momentum fluxes and turbulent heat fluxes for different Richardson numbers and compare them against the neutrally buoyant case. For this part, we will be working with the Favre averaged quantities. The Reynolds and Favre decomposition is discussed in detail in section C. Favre decomposition allows us to treat equations with variable properties in a similar fashion to that of constant property equations. As discussed in the previous section, the streamwise momentum equation on Favre averaging reduces to the following form:

$$1 - \frac{z}{L^*} = \frac{1}{\rho_c u_{\tau,c}^2}\left(-\overline{\rho u'' w''} + \overline{\mu \frac{\partial u}{\partial z}}\right). \tag{7.2.7}$$

where $\rho_c,\ u_{\tau,c}$ are the density and friction velocity at the cold wall. The superscript double prime ($u'',\ w''$) are the Favre fluctuations and L^* is the distance from the cold wall where the total stress is zero. $\overline{\rho u'' w''}$ is the Reynolds stress or the turbulent momentum flux and $\overline{\mu \partial u/\partial z}$ is the viscous shear stress or the diffusive momentum flux. From the equation, we can clearly see that the total stress in the channel can be given by a straight line. The stress budgets are shown for the hot and cold regions in the channel in Fig. 7.18. The stresses in hot region are normalized using $\rho_h u_{\tau,h}^2$

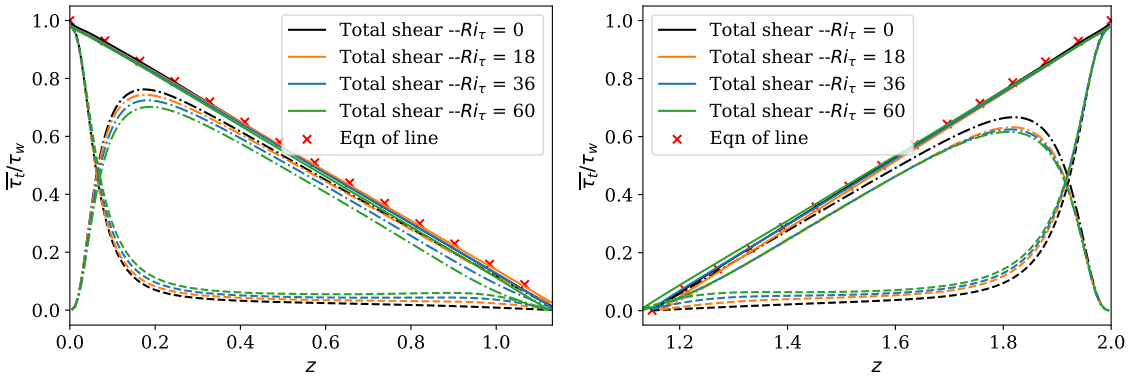

(a) Stress budget in the cold part.

(b) Stress budget in the hot part.

Figure 7.18: Stress budgets in the cold and hot regions for $Ri_\tau = 0,\ 18,\ 36,\ 60$ at $T_2/T_1 = 2$. $--$ is wall-shear stress and $- \cdot -$ is the Reynolds stress. (a) shows stress balance in the cold region normalized using $\rho_c u_{\tau,c}^2$. (b) corresponds to the stress balance in the hot region normalized using $\rho_h u_{\tau,h}^2$. The red markers correspond to the line equation given in Eq. (7.2.7).

and that in the cold region are normalized using $\rho_c u_{\tau,c}^2$. As established in the previous section, the point of zero stress does not occur at the center of the channel but is shifted toward the hot wall, dictated by the boundary conditions imposed at the walls. The viscous shear stress is highest at the walls and decreases as we get to the core. The turbulent flux increases first and then decreases with a relatively sharp dip around the core region where IGWs are located. The lack of wall-normal fluctuations cause reduced mixing of momentum, thereby resulting in a decrease in $\overline{\rho u'' w''}$. From Eq.(7.2.7), it is required that the viscous shear stress in the region increases due to this decrease in turbulent momentum flux, which can be seen from Fig. 7.18. Therefore, for stably stratified flows we see a slight bump in the viscous shear stress values around the core region. The increase in velocity gradient and the lack of mixing in the core region explains the almost parabolic profile for stratified flows, as opposed to the well-mixed, flat profile for neutrally buoyant flows.

We can arrive at an equation for heat flux in the channel by Favre averaging the energy transport equation. The final form of the equation is:

$$q_w = -\overline{\rho w'' T''} + \overline{\lambda \frac{\partial T}{\partial z}} \tag{7.2.8}$$

where q_w is the heat flux at the wall, $\overline{\rho w'' T''}$ is the turbulent heat flux and $\overline{\lambda \partial T/\partial z}$ is the diffusive heat flux. Fig. 7.19b shows the turbulent heat flux and Fig. 7.19a shows the diffusive heat flux, both normalized using the heat flux at the walls. The stratified cases are characterized by lower turbulent heat fluxes. The turbulent heat flux decreases in magnitude for increasing Richardson numbers and is more or less constant until the core of the channel. At the core, the turbulent heat fluxes decrease significantly in magnitude as the wall-normal velocity fluctuations are suppressed due to the conversion of turbulent kinetic energy to potential energy. From Eq. (7.2.8), the drop in turbulent heat fluxes requires an increase in the diffusive heat flux. This is realized by an increase in the temperature gradients in the core region (Fig. 7.19a), resulting in a thermocline.

The marked drop of turbulent heat fluxes in the core region is despite the relatively large values of the wall-normal velocity fluctuations (Fig. 7.16b) and of temperature fluctuations (Fig. 7.16d). The reason for this behavior has been mentioned several times before as the occurrence of internal gravity waves. In the next section, we will look at these waves in some detail.

7.3 Internal gravity waves

The behavior of stratified turbulent flows is determined by the interplay between the mechanical shear produced by the driving pressure gradient and the buoyancy effects that arise on the introduction of gravity. Stratification is the formation of thin, well-defined layers of varying densities

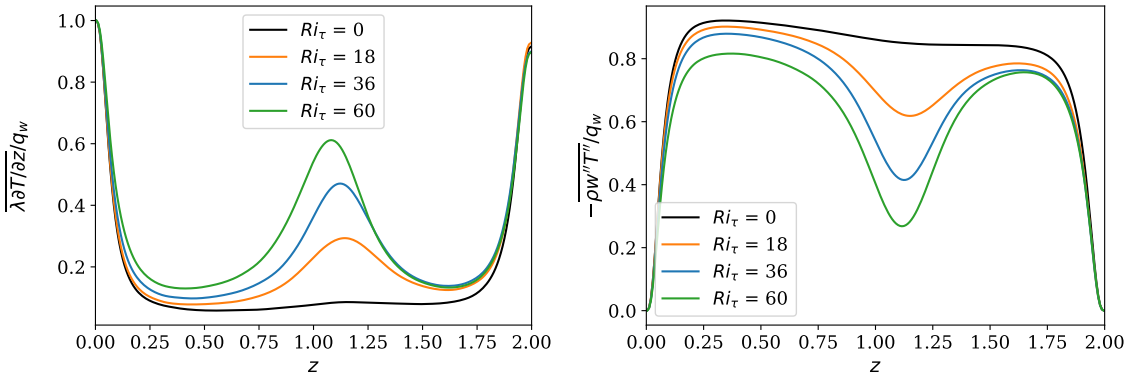

(a) Diffusive heat flux.

(b) Turbulent heat flux.

Figure 7.19: Turbulent and diffusive heat flux normalized with the wall heat flux at the walls for $Ri_\tau = 0,\ 18,\ 36,\ 60$ comparing cases B0, B1, B2, and B3. (a) - Diffusive heat flux. (b) - Turbulent heat flux.

within the fluid. If the stratification is unstable, then small disturbances, turbulent eddies in this case, are amplified so as to facilitate attaining the less energetic (more favored) configuration. If the stratification is stable, the layers of denser fluid lie below the lighter fluid, then the arrangement is already the most favored configuration with the least potential energy. Therefore, the layers of fluid are averse to mixing between them and would require energy to work against this potential gradient. This energy is supplied by the mechanical shear produced by the external driving force.

However, the distribution of shear in the channel is not uniform. It is more prominent near the walls as the no-slip velocity boundary condition implies large velocity gradients, and it decreases away from the wall to be vanishingly small and even completely absent at one point. In the regions near the walls, shear is dominant and pays the toll of potential energy to drive the mixing between the layers. In regions where the shear is weak, buoyancy is the only physical mechanism influencing the flow and the stable layers of the fluid remain unmixed. Thus evolves a kind of thick interface, thermocline, that is stable. And this happens in the core of the channel. Note that thermocline and pycnocline are used interchangeably in the present work as density is a function of only the temperature. The contours of density gradients for the cases with small density variations are shown in Fig. 7.20 and for strong variations are shown in Fig. 7.21. Note that the colors in the contours are indicative of relative magnitudes, however, the density gradients in consideration for the non-Oberbeck Boussinesq case are of much larger magnitudes than the gradients that appear within the Boussinesq approximation.

7.3.1 Buoyancy frequency

Within the thermocline, however, there still exist eddies and wall-normal velocity fluctuations. When these wall-normal velocity fluctuations displace the fluid in the very stable layers at the core, the displaced fluid experiences a restoring buoyancy force as it is surrounded by fluid of a different density. Let fluid which is initially at z_0 whose density is $\rho(z_0)$ be displaced in the wall-normal direction to $z_0 + \zeta$, where ζ is the displacement of a particle in the wall-normal direction and the fluid density at this location is $\rho(z_0 + \zeta)$. Then, a simple force balance on this displaced fluid particle would yield:

$$\rho(z_0)\frac{\mathrm{d}^2\zeta}{\mathrm{d}t^2} = (\rho(z_0 + \zeta) - \rho(z_0))g,$$

The density $\rho(z_0 + \zeta)$ can be given by a Taylor expansion as,

$$\rho(z_0 + \zeta) = \rho(z_0) + \frac{\mathrm{d}\rho(z_0)}{\mathrm{d}z}\,\zeta + \frac{\mathrm{d}^2\rho(z_0)}{\mathrm{d}z^2}\,\zeta^2 + \cdots .$$

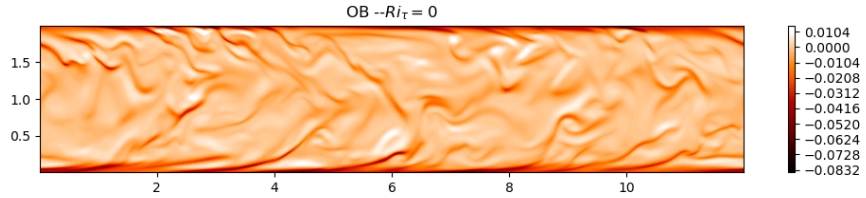

(a) $Ri_\tau = 0$ at $T_2/T_1 = 1.01$.

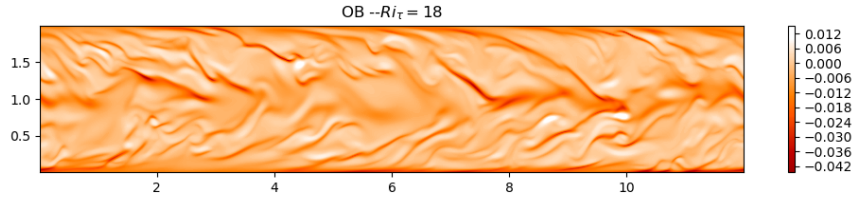

(b) $Ri_\tau = 18$ at $T_2/T_1 = 1.01$.

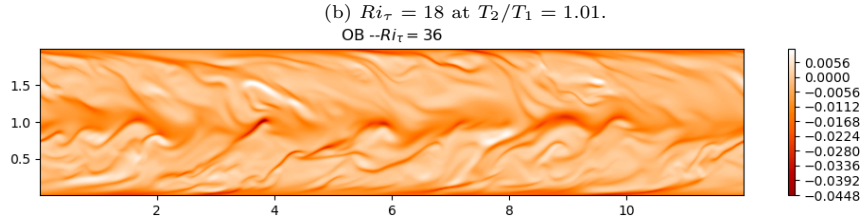

(c) $Ri_\tau = 36$ at $T_2/T_1 = 1.01$.

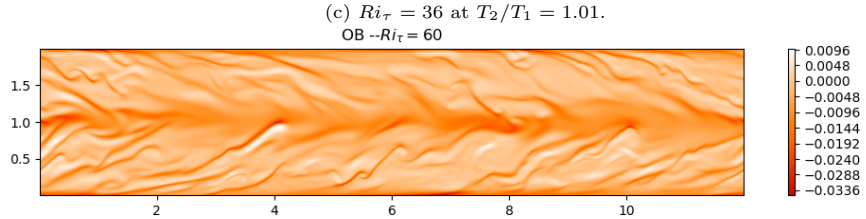

(d) $Ri_\tau = 60$ at $T_2/T_1 = 1.01$.

Figure 7.20: Density gradient ($\partial\rho/\partial z$) in the channel for Case A, a representative case for Boussinesq approximation. (*a*) $Ri_\tau = 0$. (*b*) $Ri_\tau = 18$. (*c*) $Ri_\tau = 36$. (*d*) $Ri_\tau = 60$.

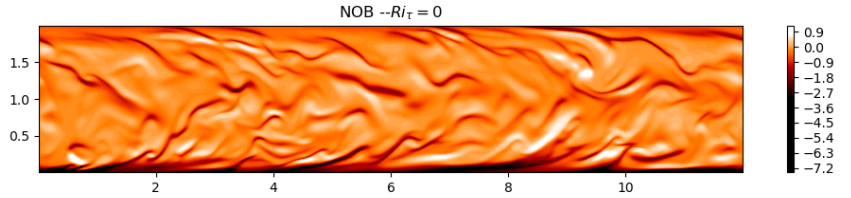

(a) $Ri_\tau = 0$ at $T_2/T_1 = 2$.

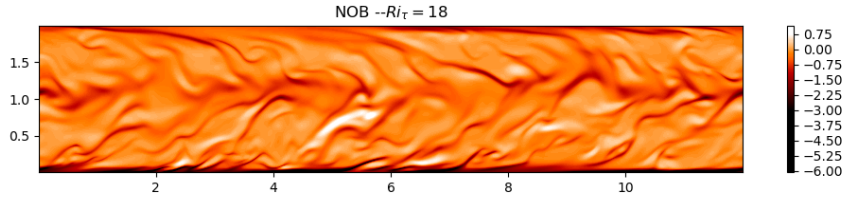

(b) $Ri_\tau = 18$ at $T_2/T_1 = 2$.

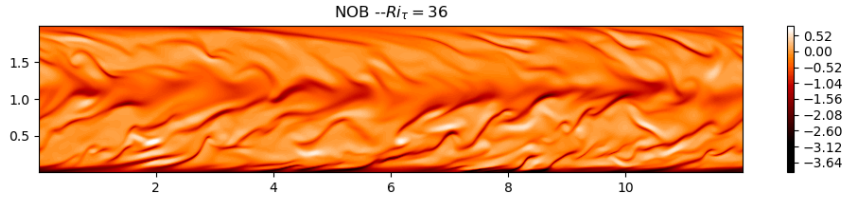

(c) $Ri_\tau = 36$ at $T_2/T_1 = 2$.

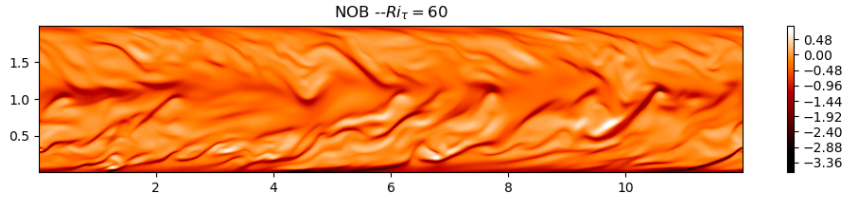

(d) $Ri_\tau = 60$ at $T_2/T_1 = 2$.

Figure 7.21: Density gradient ($\partial\rho/\partial z$) in the channel for Case B accounting for the NOB effects. (a) $Ri_\tau = 0$. (b) $Ri_\tau = 18$. (c) $Ri_\tau = 36$. (d) $Ri_\tau = 60$.

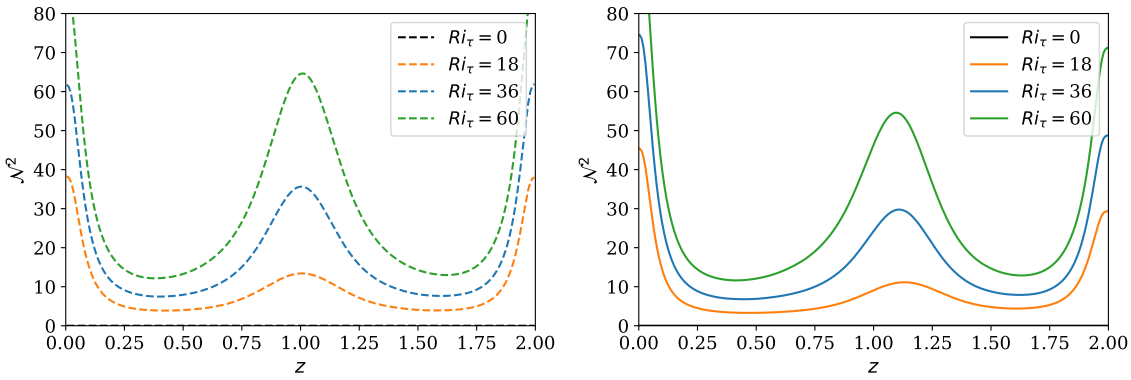

(a) Variation of $\mathcal{N}^2$ in the channel at $T_2/T_1 = 1.01$.

(b) Variation of $\mathcal{N}^2$ in the channel at $T_2/T_1 = 2$.

Figure 7.22: Variation of Brunt-Väisälä frequency in the channel with the distance from the wall for $Ri_\tau = 0,\ 18,\ 36,\ 60$ at $T_2/T_1 = 1.01$ and $T_2/T_1 = 2$. The red line corresponds to $Ri_g = 0.2$. (*a*) Case A. (*b*) Case B.

Since the flow in the region is laminar, it is reasonable to assume linear variation of density and neglect the higher-order terms. On using this we get,

$$\rho(z_0)\frac{\mathrm{d}^2\zeta}{\mathrm{d}t^2} - g\frac{\mathrm{d}\rho(z_0)}{\mathrm{d}z}\ \zeta = 0.$$

On rewriting this equation, we get:

$$\frac{\mathrm{d}^2\zeta}{\mathrm{d}t^2} + \mathcal{N}^2\zeta = 0, \tag{7.3.1}$$

where,

$$\mathcal{N} = \sqrt{-\frac{g}{\rho(z_0)}\frac{\mathrm{d}\rho}{\mathrm{d}z}}. \tag{7.3.2}$$

We can identify that Eq. (7.3.1) indicates oscillatory motion whose natural frequency is given by $\mathcal{N}$. This is called the Brunt-Väisälä frequency or the buoyancy frequency and can be used to characterize the internal gravity waves. In other words, internal gravity waves are a result of the overshooting of the fluid particle due to inertia under the action of the restoring buoyancy force, giving rise to oscillations. The existence of thermocline results in the development of these IGWs. For further reading, the reader is referred to the research mentioned in Zonta and Soldati (2018) on internal gravity waves.

The inverse of the Brunt-Väisälä frequency can be viewed as a timescale for flows that have buoyancy influencing them. The timescale gives a measure of the time taken by a fluid particle that is displaced, to come back to its equilibrium position. As the stratification increases, we know that the density gradients get steeper, and from Eq. (7.3.2) it is straightforward that the frequency increases. This means, for higher stratification, the particle would be swiftly put back to its initial position, thereby rendering the mixing process completely unlikely and turbulence non-existent.

The variation of Brunt-Väisälä frequency in the channel for different levels of stratification is shown in Fig. 7.22. We see very high values of the buoyancy frequency close to the wall. However, the density gradients near the wall are due to the boundary conditions imposed on the flow and therefore are not relevant to the discussion as we are interested in density gradients that arise due to buoyancy. Therefore, only the variation of buoyancy frequency away from the walls is considered. We see that the buoyancy frequency increases for increasing Richardson numbers and is more or less constant in the bulk of the channel except in the region dominated by buoyancy. A local maximum is observed in the core region where shear is the weakest. The figure reinforces our understanding that these waves dominate inside the thermocline.

With this understanding of the IGWs, it is easier to perceive the drop in the turbulent heat flux values (Fig. 7.19b) at the location of the interface. It is also clear that the IGWs affect the mixing

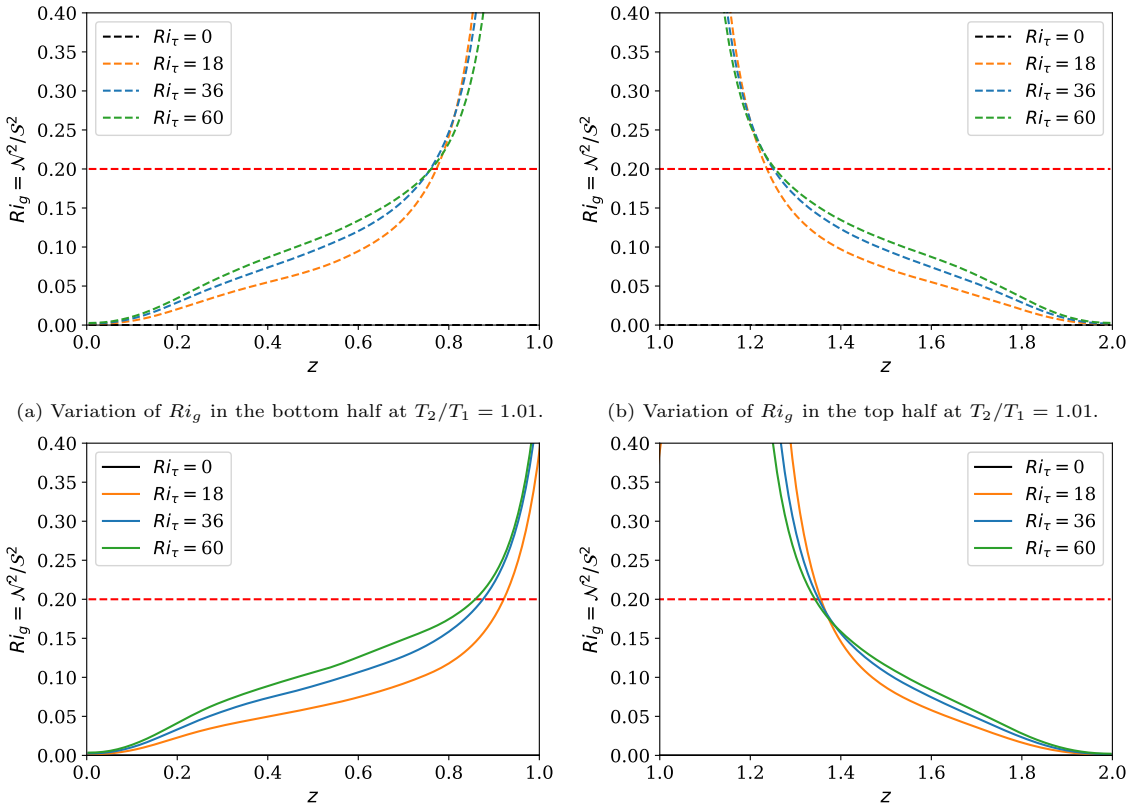

(a) Variation of Ri_g in the bottom half at $T_2/T_1 = 1.01$.

(b) Variation of Ri_g in the top half at $T_2/T_1 = 1.01$.

(c) Variation of Ri_g in the bottom half at $T_2/T_1 = 2$.

(d) Variation of Ri_g in the top half at $T_2/T_1 = 2$.

Figure 7.23: Variation of gradient Richardson number in the bottom and top halves of the channel for $Ri_\tau = 0,\ 18,\ 36,\ 60$ at $T_2/T_1 = 1.01$ and $T_2/T_1 = 2$. The red line corresponds to $Ri_g = 0.2$. $(a, b$ correspond to Case A in the cold and hot sub-channels respectively. $(c, d$ correspond to Case B in the cold and hot sub-channels respectively.

process, or more specifically hinder it in our case. In order to characterize the mixing efficiency or the state of stably stratified flow, the more commonly used parameter is the gradient Richardson number (Ri_g). The gradient Richardson number is the recurrent specification for atmospheric and oceanic flows and also in experiments. The gradient Richardson number is defined as the ratio of the square of the buoyancy frequency to that of the shear rate,

$$Ri_g = -\frac{g\frac{\partial \rho}{\partial z}}{\rho_0 \left(\frac{\partial u}{\partial z}\right)^2} = \frac{\mathcal{N}^2}{\mathcal{S}^2}. \tag{7.3.3}$$

Rohr et al. (1988) carried out experiments on uniformly sheared flows and showed that $Ri_g \geq 0.25$ renders the flow completely stable everywhere. Armenio and Sarkar (2002); Garcia-Villalba and Del Alamo (2011) showed that the gradient Richardson number for a channel does not have a global value but is a function of the distance from the wall. They reported low values close to the wall and higher values away from it, as the shear decreases. Armenio and Sarkar (2002) showed for channel flow at $Re_\tau = 180$ and Garcia-Villalba and Del Alamo (2011) for channel flow at $Re_\tau = 550$. They used the Boussinesq approximation. They found that the slope changes drastically above $Ri_g \approx 0.2$. In the present work, the gradient Richardson number as the function of wall-normal distance is plotted for the cold region as well as the hot region in Fig. 7.23. We do notice the abrupt change in slope beyond $Ri_g = 0.2$ in the cold region as well as in the hot region. However, the effect of variable inertia is clear in the fact that it is not symmetric. The $Ri_g = 0.2$ value occurs much closer to the hot wall than it does for the cold wall. The reason for this is the lower shear stress at the hot wall and higher local Richardson numbers in the hot region because of the lighter fluid present in the region. A singularity is observed for the gradient Richardson number at the location of the IGWs.

7.4 Macroscopic quantities of the flow

In this section, we will compare the coefficient of friction and the Nusselt numbers for the different cases that were simulated in the present work. In the previous sections, we have already established that the variable properties affect the turbulent activity, thereby altering the momentum and heat transfer characteristics at the walls. These macroscopic quantities are also affected by stratification as gravity hinders mixing in the vertical direction. The coefficient of friction (C_f) is based on the bulk velocity and the bulk density of the fluid and is given as:

$$C_f = \frac{\rho_w u_\tau^2}{\rho_b u_b^2/2}. \tag{7.4.1}$$

The Nusselt number (Nu), which is indicative of the heat transfer at the walls is expressed as,

$$Nu = \frac{q_w L_w^*}{k_w \Delta T}, \tag{7.4.2}$$

where, $q_w = -k\partial T/\partial z$ is the heat flux at the walls, k_w is the thermal conductivity at the walls, L_w^* is the distance of the interface (plane of zero stress) from the wall and ΔT is the temperature difference between the wall and the interface.

In Table 7.2, we compare quantitatively the change in macroscopic quantities with increasing Richardson numbers with respect to the neutrally buoyant case, for the constant property case. The same exercise is carried out in Table 7.3 for the variable property cases. We observe almost similar trends for both cases wherein the Nusselt decreases more than the coefficient of friction, hinting at a greater impact of stratification on heat transfer than momentum transfer. The decreasing values of the friction coefficients indicate that the wall-shear stress is decreasing, or in other words, the flow is getting less turbulent. The Nusselt number for a fully laminar case would be equal to 1, so at $Ri_\tau = 60$, we see that the flow is not completely laminar and theoretically should be capable to withstand greater stratification.

Case	Ri_τ	Re_b	$C_{f,c}$e3	$C_{f,h}$e3	Nu_c	Nu_h
A0	0	2823(-)	8.15(-)	8.09(-)	6.29(-)	6.28(-)
A1	18	3048 (+8 %)	6.99(-14%)	6.95(-14%)	4.25(-32%)	4.24(-32%)
A2	36	3225(+14 %)	6.25(-23%)	6.21(-23%)	3.43(-45%)	3.45 (-45%)
A3	60	3456(+22 %)	5.46(-33%)	5.38(-34%)	2.88(-54%)	2.93(-53%)

Table 7.2: Comparison of the effect of stratification on macroscopic quantities for the constant property flow. The values are compared relative to the neutrally buoyant case. C_f is the coefficient of friction based on the bulk velocity and bulk density. Nu is the Nusselt number.

Case	Ri_τ	Re_b	$C_{f,c}$e3	$C_{f,h}$e3	Nu_c	Nu_h
B0	0	2706(-)	9.52(-)	6.96(-)	6.39(-)	5.93(-)
B1	18	2937 (+9 %)	8.18(-14%)	5.74(-18%)	4.55(-29%)	3.93(-34%)
B2	36	3123(+15 %)	7.19(-25%)	5.28(-24%)	3.67(-43%)	3.33 (-44%)
B3	60	3346(+24 %)	6.20(-35%)	4.72(-32%)	2.99(-53%)	2.98(-50%)

Table 7.3: Comparison of the effect of stratification on macroscopic quantities for the variable property flow. The values are compared relative to the corresponding values of the neutrally buoyant case. C_f is the coefficient of friction based on the bulk velocity and bulk density. Nu is the Nusselt number.

In Table 7.4, we compare cases A and B at a given Richardson number. The higher local Reynolds number near the cold wall in Case B results in increased turbulence at the cold wall.

This is also seen from the table where the quantities are invariably higher at the cold wall for Case B than its Case A counterpart. Conversely, the values near the hot wall are lower than the corresponding Case A values. This difference can be critical when estimating the heat transfer coefficients for heat exchangers. We can observe that increasing Richardson numbers does not affect the difference between the macroscopic quantities at all. However, the present work covered only $T_2/T_1 = 2$, we can expect higher differences for greater temperature ratios between the walls as the disparity between the local Reynolds numbers at the walls would be greater.

Case	Ri_τ	Re_b	$C_{f,c}$e3	$C_{f,h}$e3	Nu_c	Nu_h
A0	0	2823(-)	8.15(-)	8.09(-)	6.29(-)	6.28(-)
B0		2706(-4%)	9.52(+14%)	6.96(-14%)	6.39(+2%)	5.93(-6%)
A1	18	3048 (-)	6.99(-)	6.95(-)	4.25(-)	4.24(-)
B1		2937 (-4 %)	8.18(+17%)	5.74(-17%)	4.55(+7%)	3.93(-7%)
A2	36	3225(-)	6.25(-)	6.21(-)	3.43(-)	3.45 (-)
B2		3123(-3 %)	7.19(+15%)	5.28(-14%)	3.67(+7%)	3.33 (-3%)
A3	60	3456(- %)	5.46(-)	5.38(-)	2.88(-)	2.93(-)
B3		3346(-3 %)	6.20(+14%)	4.72(-12%)	2.99(+4%)	2.98(+2%)

Table 7.4: Comparison of the macroscopic quantities for the constant and variable property flow at a given Richardson number. The change in the macroscopic quantities in variable property cases is expressed with respect to the corresponding quantities in constant property cases. C_f is the coefficient of friction based on the bulk velocity and bulk density. Nu is the Nusselt number.

7.5 Mean kinetic energy

The mean kinetic energy and the turbulent kinetic energies are derived using Favre averaged variables in section C and the final form of the equations is given here. The equation of MKE, $K = \tilde{u}_i\tilde{u}_i/2$, is:

$$\overline{\rho}\frac{\partial K}{\partial t} + \overline{\rho}\tilde{u}_j\frac{\partial K}{\partial x_j} = -\tilde{u}_i\frac{\partial \overline{p}}{\partial x_i} + \frac{\partial}{\partial x_j}\left(\tilde{u}_i\overline{\tau_{ij}} - \tilde{u}_i\overline{\rho u_i'' u_j''}\right) + \tilde{u}_i\overline{\rho}g_i - \overline{\tau_{ij}\frac{\partial \tilde{u}_i}{\partial x_j}} + \overline{\rho u_i'' u_j''}\frac{\partial \tilde{u}_i}{\partial x_j}, \tag{7.5.1}$$

and the TKE, $k = \overline{\rho u_i'' u_i''}/2\overline{\rho} = \widetilde{u_i'' u_i''}/2$ is:

$$\frac{\partial \overline{\rho}k}{\partial t} + \frac{\partial \overline{\rho}\tilde{u}_j k}{\partial x_j} = -\overline{\rho\, u_j'' u_i''}\frac{\partial \tilde{u}_i}{\partial x_j} - \frac{\partial}{\partial x_j}\left[\frac{\overline{\rho u_j'' u_i'' u_i''}}{2} + \overline{u_j'' p'} - \overline{u_i''\tau_{ij}}\right] - \overline{u_i''}\frac{\partial \overline{p}}{\partial x_i} + \overline{p'\frac{\partial u_i''}{\partial x_i}} - \overline{\tau_{ij}\frac{\partial u_i''}{\partial x_j}}, \tag{7.5.2}$$

where the variables are decomposed into a Favre mean and Favre fluctuation. Favre decomposition is also discussed in section C.

Note that, for a channel flow, the buoyancy term disappears from both the equations on averaging with the variables decomposed using Favre decomposition. It is expected that the buoyancy effects appear indirectly through other terms. It would be interesting to identify the terms that contribute to the buoyancy effects which is beyond the scope of the present thesis.

In the present work, we will look at the individual terms of the mean kinetic energy equation, Eq. (7.5.1). The LHS of the equation is the rate of change of the mean kinetic energy. On the RHS, $-\tilde{u}_i\partial\overline{p}/\partial x_i$ corresponds to the production of the mean kinetic energy by the pressure gradient that is driving the flow. This is the energy supplied to the mean motion. $\partial/\partial x_j\left(\widetilde{u}_i\overline{\tau_{ij}} - \tilde{u}_i\overline{\rho u_i'' u_j''}\right)$ is the transport term that includes the transport of energy of the motion by viscous shear stresses

and Reynolds stresses respectively. Since the energy is only transported from one part of the domain to another, the volume integral of the transport terms is zero. $\tilde{u}_i\overline{\rho}g_i$ is the production or dissipation of the mean motion by buoyancy. $\overline{\tau_{ij}\partial\tilde{u}_i/\partial x_j}$ is the viscous dissipation of the mean flow. This corresponds to the energy that is directly lost as heat and is not cascaded to smaller eddies. Finally, $\overline{\rho u_i'' u_j''}\partial\tilde{u}_i/\partial x_j$ is the dissipation term or the energy that is cascaded from the mean flow towards smaller eddies and is the source of turbulent kinetic energy.

The variation of different terms of the MKE equation in the channel at $T_2/T_1 = 1.01$ (left side) and $T_2/T_1 = 2$ (right side) for $Ri_\tau = 0,\ 18,\ 36,\ 60$ is shown in Fig. 7.24. The $T_2/T_1 = 1.01$ case is indicative of the Boussinesq approximation as the density variations are not strong enough and can be neglected and, the case $T_2/T_1 = 2$ corresponds to the one with strong density gradients where we could expect to see some variable inertia effects. For the channel with $T_2/T_1 = 1.01$, we see that at all Richardson numbers, the terms are more or less symmetrical about the mid-plane of the channel. The mean energy produced is transported to the walls by means of viscous stresses and turbulent stresses. The transport of mean energy by turbulent stresses dips in the core of the channel where the IGWs are located, due to a lack of turbulence, and the energy transported by the viscous stresses sees a rise at the location. This partnership between viscous transport and turbulent transport becomes significant at larger Richardson numbers. At the walls, the mean energy is either converted to heat (most of it) or becomes the source of turbulent kinetic energy.

In the case of stronger density gradients, $T_2/T_1 = 2$, the profiles become asymmetrical. The friction Reynolds number at the hot wall is lower than that at the cold wall. This implies that even though the velocity gradients may be larger at the hot wall, the effect of higher dynamic viscosity values at the cold wall overpowers, resulting in high shear stress values at the cold wall. As a result, the viscous dissipation and the turbulent kinetic energy production at the hot wall are lower than that at the cold wall. This is apparent from Fig. 7.24b, Fig. 7.24d, Fig. 7.24f and, Fig. 7.24h. From the figures, it is also evident that the transport of MKE by turbulent stresses is compensated by the viscous stresses at the location of IGWs, which in this case are shifted toward the hot wall.

To summarize, stratification suppresses turbulence and consequently, in the vicinity of the IGWs, the transport of MKE by turbulent fluctuations is hindered. The degree of hindrance increases with the increase of stratification. The viscous stresses make up for the lack of transport by the turbulent stresses. The temperature ratio between the walls dictates the positioning of the IGWs and also renders the dissipation of MKE at both walls asymmetric.

7.6 Spanwise vorticity

In this section, we will look at the variation of spanwise vorticity in the channel. The motivation behind the choice of spanwise vorticity is that the relatively stronger density gradient occurs in the direction normal to the pressure gradient, thereby contributing to the vorticity in the spanwise direction. This is better explained with the vorticity transport equation which is:

$$\frac{D\omega_i}{Dt} = -\omega_i\frac{\partial u_j}{\partial x_j} + \frac{1}{\rho^2}\epsilon_{ijk}\frac{\partial\rho}{\partial x_j}\frac{\partial p}{\partial x_k} + \omega_j\frac{\partial u_i}{\partial x_j} + \frac{1}{Re_\tau}\frac{\partial^2\omega_i}{\partial x_j\partial x_i}, \tag{7.6.1}$$

where ϵ_{ijk} is the Levi-Civita symbol. The variation of the vorticity in the channel at $T_2/T_1 = 1.01$ (left side) and $T_2/T_1 = 2$ (right side) for $Ri_\tau = 0,\ 18,\ 36,\ 60$ is shown in Fig. 7.25. The vorticity profiles do not look very different from the typical vorticity profiles. However, a peculiar transition from the hot region to the cold region is observed for higher Richardson numbers in the vicinity of the IGWs. The vorticity gradient gets steeper. This is because the eddies on either side of the interface can only scour the interface and cannot penetrate it. This results in lack of interaction between the eddies on either side. The interface acts as a wall and the eddies on one side are not influenced by the eddies on the opposite side. Thus, as the interface grows with increasing Richardson numbers, we observe steeper gradient in the vorticity fields at the interface.

The term, $\epsilon_{ijk}(\partial\rho/\partial x_j)(\partial p/\partial x_k)/\rho^2$, is called the baroclinic torque or the baroclinic production term. When the density gradients are not aligned to the pressure gradient, the lighter fluid accel-

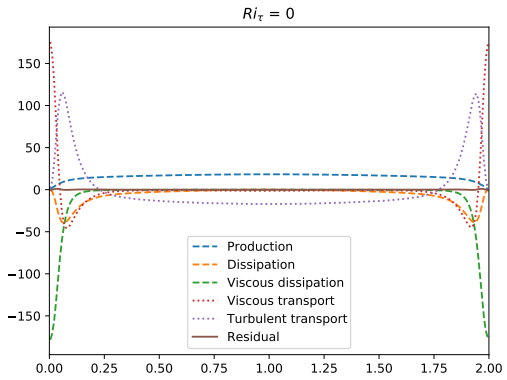

(a) MKE budget for $Ri_\tau = 0$ at $T_2/T_1 = 1.01$.

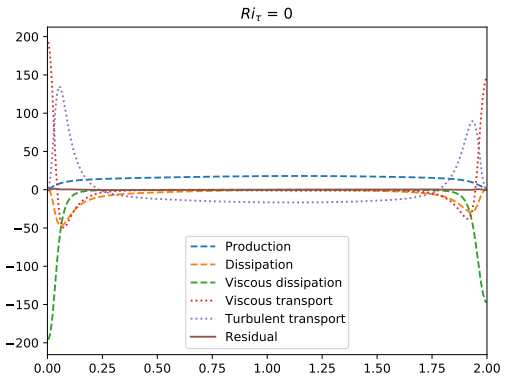

(b) MKE budget for $Ri_\tau = 0$ at $T_2/T_1 = 2$.

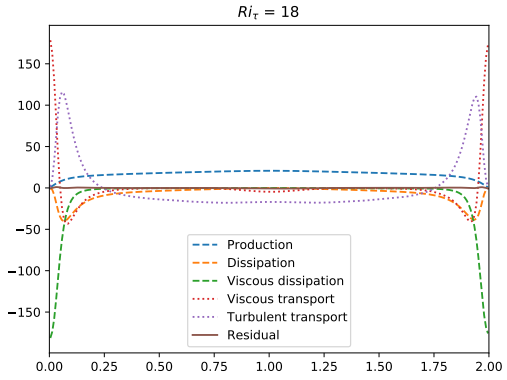

(c) MKE budget for $Ri_\tau = 18$ at $T_2/T_1 = 1.01$.

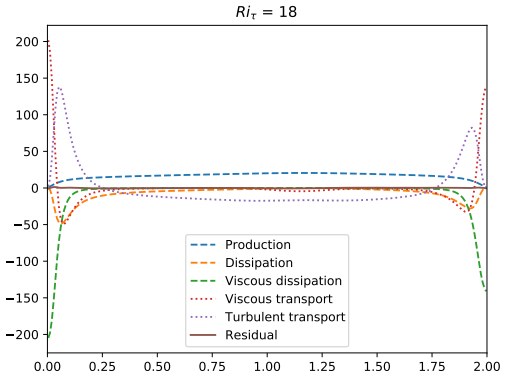

(d) MKE budget for $Ri_\tau = 18$ at $T_2/T_1 = 2$.

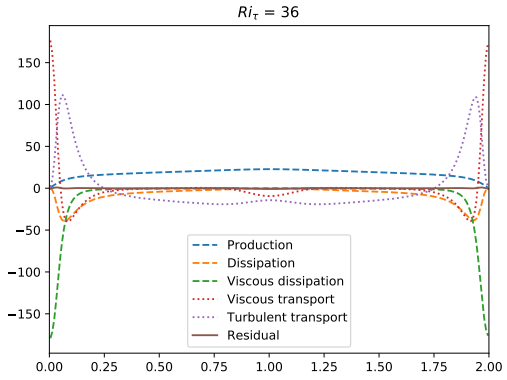

(e) MKE budget for $Ri_\tau = 36$ at $T_2/T_1 = 1.01$.

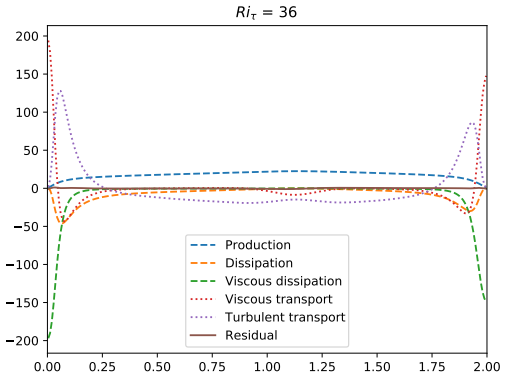

(f) MKE budget for $Ri_\tau = 36$ at $T_2/T_1 = 2$.

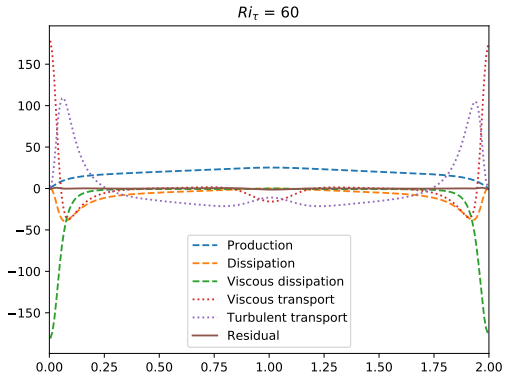

(g) MKE budget for $Ri_\tau = 60$ at $T_2/T_1 = 1.01$.

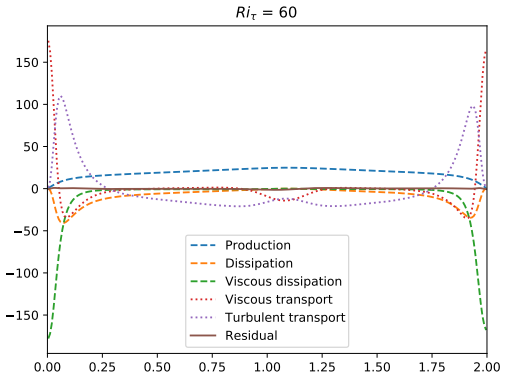

(h) MKE budget for $Ri_\tau = 60$ at $T_2/T_1 = 2$.

Figure 7.24: MKE budget for Case A, a representative case for Boussinesq approximation, and Case B, accounting for the NOB effects. (a, c, e, g) correspond to Case A and (b, d, f, h) correspond to Case B for $Ri_\tau = 0,\ 18,\ 36,\ 60$ respectively.

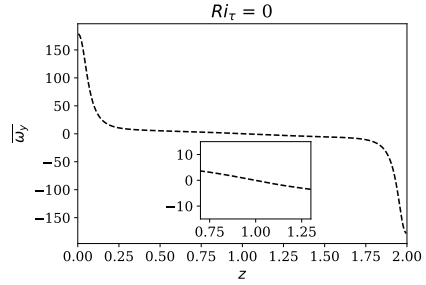

(a) Spanwise vorticity for $Ri_\tau = 0$ at $T_2/T_1 = 1.01$.

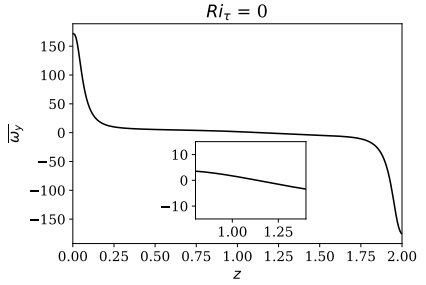

(b) Spanwise vorticity for $Ri_\tau = 0$ at $T_2/T_1 = 2$.

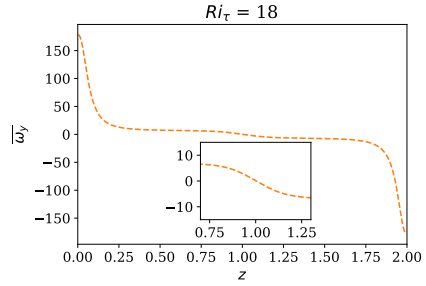

(c) Spanwise vorticity for $Ri_\tau = 18$ at $T_2/T_1 = 1.01$.

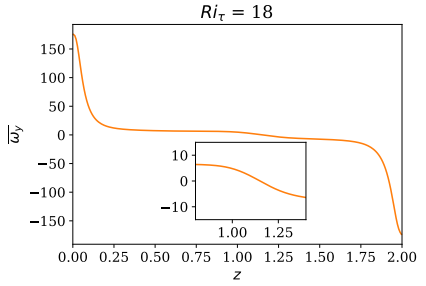

(d) Spanwise vorticity for $Ri_\tau = 18$ at $T_2/T_1 = 2$.

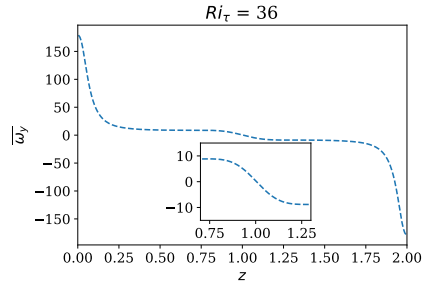

(e) Spanwise vorticity for $Ri_\tau = 36$ at $T_2/T_1 = 1.01$.

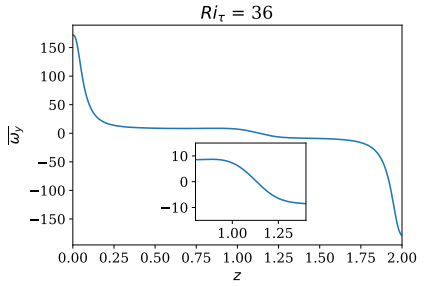

(f) Spanwise vorticity for $Ri_\tau = 36$ at $T_2/T_1 = 2$.

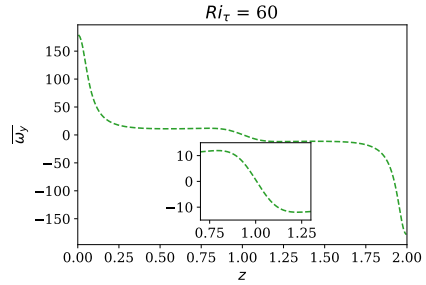

(g) Spanwise vorticity for $Ri_\tau = 60$ at $T_2/T_1 = 1.01$.

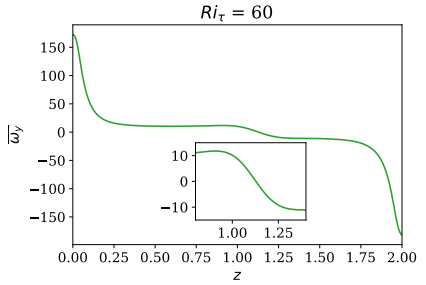

(h) Spanwise vorticity for $Ri_\tau = 60$ at $T_2/T_1 = 2$.

Figure 7.25: Spanwise vorticity profiles for Case A, a representative case for Boussinesq approximation, and Case B, accounting for the NOB effects. The inset shows the close-up view in the vicinity of the IGWs. (a, c, e, g) correspond to Case A and (b, d, f, h) correspond to Case B for $Ri_\tau = 0,\ 18,\ 36,\ 60$ respectively.

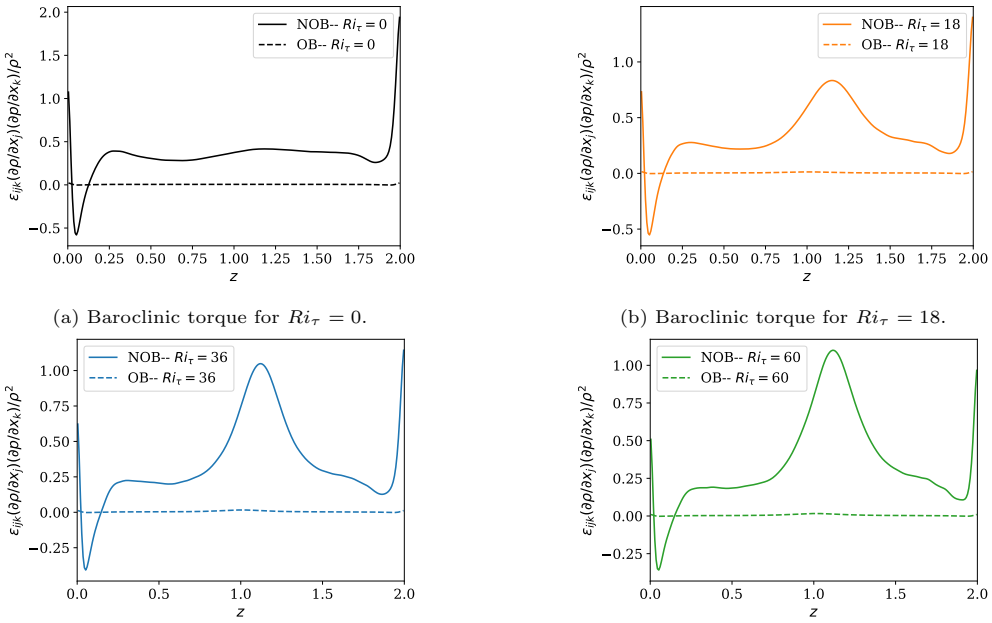

(a) Baroclinic torque for $Ri_\tau = 0$.

(b) Baroclinic torque for $Ri_\tau = 18$.

(c) Baroclinic torque for $Ri_\tau = 36$.

(d) Baroclinic torque for $Ri_\tau = 60$.

Figure 7.26: Baroclinic torque $(\epsilon_{ijk}(\partial\rho/\partial x_j)(\partial p/\partial x_k)/\rho^2)$ at $T_2/T_1 = 1.01$, a representative case for Boussinesq approximation (OB) and at $T_2/T_1 = 2$ accounting for the NOB effects (NOB). (a) $Ri_\tau = 0$. (b) $Ri_\tau = 18$. (c) $Ri_\tau = 36$. (d) $Ri_\tau = 60$.

erates faster than the heavier fluid resulting in the generation of vorticity. This term is non-zero in variable density flows. Since the term is proportional to the density gradient, the effect the term bears will be mostly around the thermocline. The variation of the baroclinic torque is shown in Fig. 7.26. The behavior in the proximity to the walls is not relevant as the density gradients in the region are due to boundary conditions imposed on the flow. Away from the walls though, for the case with negligible density variations, $T_2/T_1 = 1.01$, we see a flat line for the baroclinic term in the entire channel. But, for the case with relatively stronger density gradients, $T_2/T_1 = 2$, we see that the term is non-zero in the entire channel with a slight bump close to the IGWs, in the presence of gravity, because of the thermocline. And the size of the bump grows with the thickness of the thermocline (increasing Richardson numbers). This is expected as the density changes much more sharply in this region than anywhere else in the channel. However, the order of magnitude of the baroclinic term is much smaller than the order of the magnitude of the vorticity field in the channel and therefore will not have a significant impact on the vorticity transport equation.

Vortex stretching is probably the most important mechanism in turbulent flows. The energy is transferred to the smaller scales by the mechanism of vortex stretching. It is a mechanism to redistribute energy and is driven by the already existing vorticity. It cannot create vorticity. In the vorticity transport equation, Eq. (7.6.1), $\omega_j \partial u_i/\partial x_j$ represents the vortex stretching. The distribution of the vortex stretching term in the channel is shown in Fig. 7.27. Unsurprisingly we see vortex stretching to a large degree in close proximity to the walls as most of the vorticity is present there. To see the effect of gravity, we can look at the behavior of the term in the vicinity of the thermocline. A zoomed-in view at the location of the IGWs for the different cases is shown in Fig. 7.28. The vortex stretching term for the neutrally buoyant case is more or less linear as it changes from negative values on the cold side to positive values on the hot side. At higher Richardson numbers, as the interface grows, it is apparent that the lack of interaction of the flow field on either side of the interface affects the vortex stretching. The relatively larger gradients at the interface act upon the leftover eddies at the interface and recreate the behavior observed close to the walls, but at significantly lower orders of magnitudes.

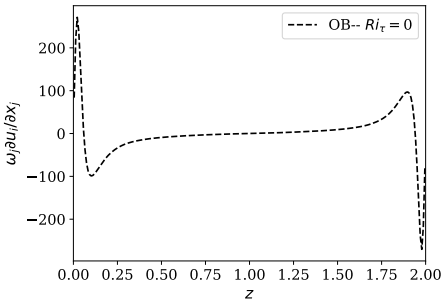

(a) Vortex stretching at $T_2/T_1 = 1.01$.

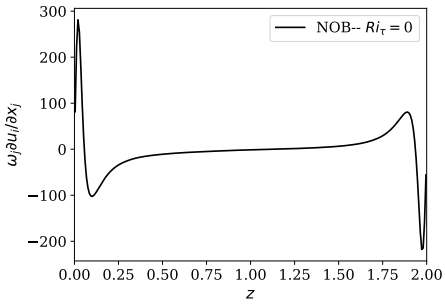

(b) Vortex stretching at $T_2/T_1 = 2$.

Figure 7.27: Vortex stretching ($\omega_j \partial u_i / \partial x_j$) distribution in the entire channel for the neutrally buoyant case ($Ri_\tau = 0$). (a) - Case A, a representative case for Boussinesq approximation (OB). (b) - Case B, accounting for the NOB effects (NOB).

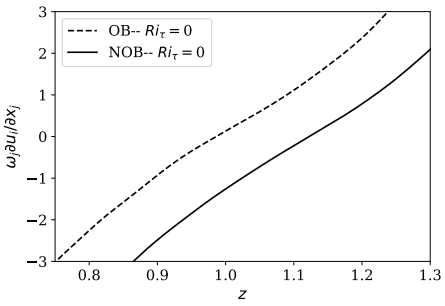

(a) Vortex stretching for $Ri_\tau = 0$.

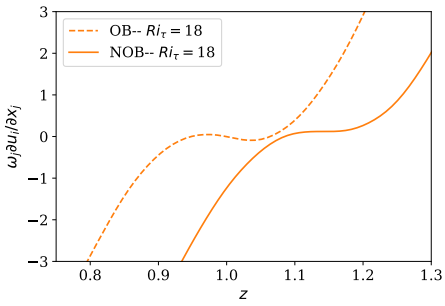

(b) Vortex stretching for $Ri_\tau = 18$.

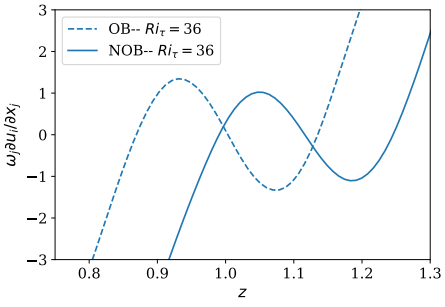

(c) Vortex stretching for $Ri_\tau = 36$.

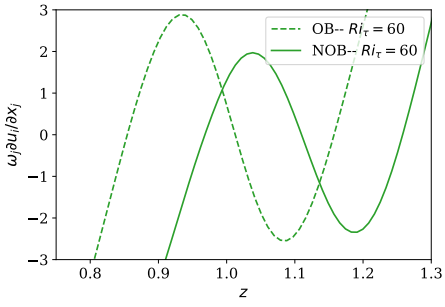

(d) Vortex stretching for $Ri_\tau = 60$.

Figure 7.28: Close up of the vortex stretching ($\omega_j \partial u_i / \partial x_j$) distribution in the vicinity of IGWs comparing Case A, a representative case for Boussinesq approximation (OB) and Case B, accounting for the NOB effects (NOB). (a) $Ri_\tau = 0$. (b) $Ri_\tau = 18$. (c) $Ri_\tau = 36$. (d) $Ri_\tau = 60$.

8

Conclusion

In the present work, we studied stably stratified turbulent flows with strong density gradients using direct numerical simulations. Previously, studies were mostly carried out for negligible density variations using the Boussinesq approximation. Garg et al. (2000) conducted the first set of DNS studies in the subject and reported complete relaminarization at $Ri_\tau = 60$. Armenio and Sarkar (2002) followed up with LES studies covering a comprehensive range of Richardson numbers, beyond $Ri_\tau = 60$, upto $Ri_\tau = 480$. Garcia-Villalba and Del Alamo (2011) presented DNS results of stratified turbulent flows at $Re_\tau = 550$, and Zonta et al. (2022) at $Re_\tau = 1000$.

In our work, we ventured beyond the Boussinesq approximation and used the low-Mach number approximation of the Navier-Stokes equations. The low-Mach number approximation decouples the thermodynamic pressure from the momentum equations, thereby accounting for density fluctuations due to temperature only. The pressure-splitting algorithm was incorporated to solve for the dynamic pressure from the variable coefficient Poisson equation. The numerical method was validated and a campaign of simulations covering $Ri_\tau = 0,\ 18,\ 36,\ 60$ was carried out for constant property flows and variable property flows at $Re_{\tau 0} = 180$. The evolution of the flow with variable properties for $Ri_\tau = 60$ was marked by frequent relaminarization and a transition back to turbulence. Simulations corresponding to higher Richardson numbers were conducted only for the flow to be fully laminarized due to the small computational box.

It was observed that the central region of the channel was severely affected by the buoyancy forces as the shear in the region is minimum. The buoyancy forces suppress the eddies and vertical mixing is hampered. As these eddies travel across layers of fluid of varying densities in the presence of gravity, they experience a restoring buoyancy force, and turbulent kinetic energy is converted to potential energy. In the core, the unmixed layers form a kind of thick interface or a thermocline and the restoring forces in the region are the highest, thus resulting in the formation of internal gravity waves. These waves are laminar structures devoid of turbulent fluctuations of consequence. The eddies that exist in the region are incapable of penetrating the interface and therefore the thermocline acts as a barrier for momentum and heat transport. In the region close to the walls, however, it was observed that the specified levels of stratification did not influence the flow. The shear dominates in this region, almost unopposed, and the turbulent fluctuations were found to be comparable with that of the neutrally buoyant case, especially when compared using the semi-local scales.

On comparing the turbulent flows with and without property variations we observed that the symmetry in the flow structure was lost when the temperature difference between walls became large. The flow was found to be more turbulent in the cold sub-channel in the case of flow with variable properties. Thus the location of the plane of zero stress is shifted away from the cold wall. The distance from the cold wall at which the plane occurs was computed and shown to be constant for given boundary conditions and thermodynamic properties. Although the effects of gravity were identical in both cases, the location at which the flow was affected the most was determined by

the plane of zero stress. So for variable property flows, the interface is formed not at the center, but closer to the hot wall. This was demonstrated through the stress budgets and the reduction of turbulent heat flux in the core region.

In addition, the frequency of the internal gravity waves was discussed. This is the buoyancy frequency. The gradient Richardson number, defined as the ratio of the buoyancy frequency and the local shear, varies in the channel as a function of distance from the wall. Armenio and Sarkar (2002); Garcia-Villalba and Del Alamo (2011) reported a sudden change in slope of the gradient Richardson number when $Ri_g \approx 0.2$ for the flows with Boussinesq approximation. This observation was consistent even for flows with variable properties.

Further, we looked at the macroscopic quantities in the flow. The coefficient of friction and the Nusselt number at the wall progressively decreased with increasing Richardson numbers, signifying the laminarizing tendency of stable stratification. The percentage drop in these quantities between turbulent flows for given two Richardson numbers was found to be more or less identical for constant and variable property flows. However, in variable property flows, the values are no longer symmetric at the walls as the flow is more turbulent at the cold wall owing to the variations in density and dynamic viscosity. Consequently, the Nusselt number and the coefficient of friction at the cold wall are higher.

Furthermore, we considered the mean kinetic energy budgets for stably stratified turbulent flows. We witnessed that the transport of the mean kinetic energy by turbulent stresses decreases locally where the thermocline is formed. This is compensated by the viscous stresses as we see that the energy transported by the viscous stresses increases correspondingly. Also, for the variable property flows, as the flow is more turbulent in the cold sub-channel, we see more production of turbulent kinetic energy and more viscous dissipation closer to the cold wall.

Since there exists a density gradient perpendicular to the pressure gradient, we expected that the baroclinic term influenced the spanwise vorticity. So we also plotted the profiles of spanwise vorticity, the baroclinic term, and the vortex stretching term. From the vorticity profiles, we saw that the gradient of vorticity near the thermocline increases as the eddies cannot penetrate across the interface and therefore are completely oblivious to the presence of eddies on the other side. As a result, a sharp gradient develops in the region. From the profiles of the baroclinic term, we saw that, although the effect of this term is distinctive, the order of magnitude is almost negligible in comparison to the order of magnitude of the vorticity at the walls. We probably have to raise the density gradients even further to observe any relevant contribution of this term. Finally, the vortex stretching term also showed very distinctive behavior in the vicinity of the thermocline but at much smaller orders of magnitude than its effect at the walls. Therefore, these effects can be overlooked.

9

Discussion

Stably stratified turbulent flows are an interesting class of flows that can be observed in many different settings ranging from atmospheric boundary layers to the flow in heat exchangers. The physics of weakly/moderately wall-bounded stratified flows is extensively studied and understood, especially when the property variations in the flow are small enough to be ignored. However, when it comes to flows with property variations and stronger density gradients, the amount of literature available seems to be wanting. The present work attempted to contribute to the existing understanding of wall-bounded stratified turbulent flows beyond the Oberbeck-Boussinesq assumptions.

From the DNS simulations at $Re_\tau = 180$ and $0 \leq Ri_\tau \leq 60$, inside a channel with considerable property variations, we observed that the effect of gravity is mostly identified in the central region of the channel, just like for the Boussinesq case. The difference between the two cases is the position of the interface between the hot and cold sub-channels, wherein the interface for the variable property case is closer to the hot wall. So although the effect seemed identical, the location where the effect was seen was different. The present study has shed some light on the stratified, variable property flows but there are a fair few challenges that require to be dealt with. Some of them are mentioned below.

1. In the present code, we assume calorically perfect fluid (C_p = constant). This is a reasonable assumption for several fluids but is not applicable to supercritical fluids. Many studies are being undertaken that involve supercritical fluids in thermal cycles as they provide an environmentally friendly alternative. These fluids undergo large changes in thermophysical properties, including C_p, even for very small temperature differences. As a result, even a hint of stable stratification could lead to complete relaminarization of the flow. It is not straightforward to construct the experimental setup to study turbulent flows with supercritical fluids. Therefore, it is necessary to simulate the flows with these fluids using DNS to better understand the limits of operation.

2. The present study was conducted at $Re_\tau = 180$. Although this is a starting point, the separation of scales at this Reynolds number is not sufficient to appreciate the effects of viscosity and buoyancy in isolation, within the same channel. With the framework put up in the current thesis, we can conduct DNS at higher Reynolds numbers, so that there is substantial scale separation. Zonta et al. (2012a) reports that the effect of variation of viscosity fades at increasing Reynolds numbers. It would be interesting to study the effect of variation of several properties at higher Reynolds numbers.

3. We use the ideal gas equation of state for computing density. Dynamic viscosity and thermal conductivity are expressed as functions of density such that the Reynolds number does not vary significantly from the hot wall to the cold wall. Since stably stratified turbulent flows are strongly influenced by buoyancy forces that depend to a great extent on the thermophysical

properties of the fluid (like density gradients), it would be of interest to simulate the flow with property variations that correspond to a real fluid.

Appendix A

Low-Mach Number Equations

A.1 Derivation of the low-Mach approximation

The conservation equations of mass, momentum, and energy in the non-dimensional form are; (McMurtry et al., 1986):

$$\frac{\partial \rho}{\partial t} + \nabla \cdot (\rho \mathbf{u}) = 0, \tag{A.1.1}$$

$$\frac{D\mathbf{u}}{Dt} = -\frac{1}{\gamma M^2}\nabla p + \frac{1}{Re}\nabla \cdot \tau, \tag{A.1.2}$$

$$\frac{DE}{Dt} = -\nabla \cdot ((\gamma - 1)p\mathbf{u}) + \frac{\gamma(\gamma-1)M^2}{Re}\nabla \cdot (\tau \cdot \mathbf{u}) - \frac{\gamma}{Re\,Pr}\nabla \cdot \mathbf{q}, \tag{A.1.3}$$

where,

$$E = T + \frac{\gamma(\gamma-1)M^2}{2}\mathbf{u}^2, \tag{A.1.4}$$

and the equation of state in non-dimensional form is

$$p = \rho T. \tag{A.1.5}$$

The velocity, length, density, and temperature are scaled with the reference values of U_0, L_0, ρ_0, and T_0. The pressure is scaled using a reference thermodynamic pressure $\rho_0 R T_0$, where R is the universal gas constant. M is the mach number which can be expressed as $M = U_0/\sqrt{\rho_0 R T_0}$. γ is the ratio of specific heat. The Reynolds number, $Re = \rho_0 U_0 L_0/\mu_0$ and, the Prandtl number, $Pr = \mu_0 C_{p0}/\lambda_0$ where μ_0 is the dynamic viscosity of the fluid, λ_0 is the thermal conductivity and

$$C_{p0} = \frac{\gamma R}{\gamma - 1} \tag{A.1.6}$$

is the specific heat capacity at constant pressure.

Since we are solving for low-Mach number flows or, more precisely, in the limit of vanishing Mach, we assume that $\gamma M^2 << 1$ and express the dependent variables as asymptotic expansions of γM^2 and then reduce the equations to leading order of γM^2. For example: we write pressure as $p = p^{(0)} + (\gamma M^2)p^{(1)} + (\gamma M^2)^2 p^{(2)} + \cdots$. Similarly, velocity and density, and temperature can be expanded similarly. By substituting the expansions in the above equations, we get,

$$\frac{\partial \rho^{(0)}}{\partial t} + \nabla \cdot (\rho^{(0)}\mathbf{u}^{(0)}) = 0, \tag{A.1.7}$$

$$\nabla p^{(0)} = 0, \tag{A.1.8}$$

$$\rho^{(0)} \frac{\mathrm{D}^{(0)}}{\mathrm{D}t} T^{(0)} = -(\gamma - 1) p^{(0)} \nabla \cdot \mathbf{u}^{(0)} - \frac{\gamma}{Pr\ Re} \nabla \cdot q^{(0)}, \tag{A.1.9}$$

$$p^{(0)} = \rho^{(0)} T^{(0)}. \tag{A.1.10}$$

Since the zeroth-order momentum equation does not contain any velocity terms, we include the first-order momentum equation as

$$\rho^{(0)} \frac{\mathrm{D}^{(0)}}{\mathrm{D}t} \mathbf{u}^{(0)} = -\nabla p^{(1)} + \frac{1}{Re} \nabla \cdot \tilde{\tau}^{(0)}. \tag{A.1.11}$$

Note that the *thermodynamic* pressure ($p^{(0)}$) does not vary in space but may vary in time and does not directly influence momentum transport, but rather the *dynamic* pressure ($p^{(1)}$) transports momentum. We assume that the variation in dynamic pressure is negligible and thermophysical properties are evaluated as a function of temperature only. In addition, we see that the viscous heating term from the energy equation drops out at low-Mach number limits (McMurtry et al., 1986). Thus, we have the equations for low-Mach number approximation.

If the equations are solved on the closed system then the variation of thermodynamic pressure becomes relevant. On taking the time derivative of Eq. (A.1.10), we get,

$$\frac{\mathrm{d}p^{(0)}}{\mathrm{d}t} = \rho^{(0)} \frac{\partial T^{(0)}}{\partial t} + T^{(0)} \frac{\partial \rho^{(0)}}{\partial t}.$$

Substituting Eq. (A.1.7) and Eq. (A.1.9) we get,

$$\frac{\mathrm{d}p^{(0)}}{\mathrm{d}t} = -\rho^{(0)} \mathbf{u}^{(0)} \cdot \nabla T^{(0)} - (\gamma - 1) p^{(0)} \nabla \cdot \mathbf{u}^{(0)} - \frac{\gamma}{Pr\ Re} \nabla \cdot q^{(0)} - T^{(0)}\ \nabla \cdot (\rho^{(0)} \mathbf{u}^{(0)}).$$

Grouping the first and last term on the RHS and simplifying, we will be left with an equation for the rate of change of thermodynamic pressure.

$$\frac{\mathrm{d}p^{(0)}}{\mathrm{d}t} = -(\gamma) p^{(0)} \nabla \cdot \mathbf{u}^{(0)} - \frac{\gamma}{Pr\ Re} \nabla \cdot q^{(0)}. \tag{A.1.12}$$

And substituting $p^{(0)} \nabla \cdot \mathbf{u}^{(0)}$ from Eq. (A.1.12) in Eq. (A.1.9), we get an energy conservation equation that can be used on a closed system that is

$$\rho^{(0)} \frac{\mathrm{D}^{(0)}}{\mathrm{D}t} T^{(0)} = \frac{\gamma - 1}{\gamma} \frac{\mathrm{d}p^{(0)}}{\mathrm{d}t} - \frac{1}{Pr\ Re} \nabla \cdot q^{(0)}. \tag{A.1.13}$$

Thus, the time derivative of thermodynamic pressure is accounted for in the governing equations of closed systems.

Note that, for the sake of simplicity, the equation was derived with the assumption that $C_p/C_{p0} = 1$. The whole process can be repeated for any given C_p, a flavor of which is shown in the next section.

A.2 Derivation of the rate of change of thermodynamic pressure and divergence of velocity

In this section, we will derive the constraint imposed on the divergence of velocity which is used in Eq .(4.2.10). To do so, we start by rewriting the Navier-Stokes equations in the limits of zero-Mach which is derived in the previous section,

$$\frac{\partial \rho}{\partial t} + \frac{\partial \rho u_j}{\partial x_j} = 0 \tag{A.2.1}$$

$$\rho\frac{\partial u_i}{\partial t}+\rho u_j\frac{\partial u_i}{\partial x_j}=-\frac{\partial p}{\partial x_i}+\frac{1}{Re_\tau}\frac{\partial \tau_{ij}}{\partial x_j} \tag{A.2.2}$$

$$\rho C_p\frac{\partial T}{\partial t}+\rho C_p u_j\frac{\partial T}{\partial x_j}=\frac{1}{Re_\tau\ Pr}\frac{\partial}{\partial x_j}\left(\lambda\frac{\partial T}{\partial x_j}\right)+\frac{\gamma-1}{\gamma}\frac{\mathrm{d}p_0}{\mathrm{d}t}+\frac{Q}{Re_\tau\ Pr} \tag{A.2.3}$$

$$p_0=\rho T \tag{A.2.4}$$

Note that the superscript denoting the order has been dropped and all variables, except pressure, are of zeroth order. Thermodynamic pressure is given by p_0 and the dynamic pressure by p. Q is the volumetric heat source.

Taking the time derivative of Eq.(A.2.4):

$$\frac{\mathrm{d}p_0(t)}{\mathrm{d}t}=T\frac{\partial\rho}{\partial t}+\rho\frac{\partial T}{\partial t} \tag{A.2.5}$$

Using Eqs. (A.2.1) and (A.2.3) and using that thermodynamic pressure is constant in space we get:

$$\frac{\mathrm{d}p_0(t)}{\mathrm{d}t}=-T\frac{\partial\rho u_j}{\partial x_j}-\rho u_j\frac{\partial T}{\partial x_j}+\frac{1}{Re_\tau\ Pr}\frac{1}{C_p}\frac{\partial}{\partial x_j}\left(\lambda\frac{\partial T}{\partial x_j}\right)+\frac{1}{C_p}\frac{\gamma-1}{\gamma}\frac{\mathrm{d}p_0(t)}{\mathrm{d}t}+\frac{1}{C_p}\frac{Q}{Re_\tau\ Pr}$$

$$\frac{\mathrm{d}p_0(t)}{\mathrm{d}t}=-\frac{\partial\rho T u_j}{\partial x_j}+\frac{1}{Re_\tau\ Pr}\frac{1}{C_p}\frac{\partial}{\partial x_j}\left(\lambda\frac{\partial T}{\partial x_j}\right)+\frac{1}{C_p}\frac{\gamma-1}{\gamma}\frac{\mathrm{d}p_0(t)}{\mathrm{d}t}+\frac{1}{C_p}\frac{Q}{Re_\tau\ Pr}$$

$$\frac{\mathrm{d}p_0(t)}{\mathrm{d}t}=-p_0\frac{\partial u_i}{\partial x_i}+\frac{1}{Re_\tau\ Pr}\frac{1}{C_p}\frac{\partial}{\partial x_j}\left(\lambda\frac{\partial T}{\partial x_j}\right)+\frac{1}{C_p}\frac{\gamma-1}{\gamma}\frac{\mathrm{d}p_0(t)}{\mathrm{d}t}+\frac{1}{C_p}\frac{Q}{Re_\tau\ Pr} \tag{A.2.6}$$

On rearranging the terms we get:

$$\frac{\partial u_i}{\partial x_i}=\frac{1}{p_0(t)C_p}\left[\frac{1}{Re_\tau\ Pr}\frac{\partial}{\partial x_j}\left(\lambda\frac{\partial T}{\partial x_j}\right)+\left(\frac{\gamma-1}{\gamma}-C_p\right)\frac{\mathrm{d}p_0(t)}{\mathrm{d}t}+\frac{Q}{Re_\tau\ Pr}\right] \tag{A.2.7}$$

We can integrate the equation over the whole control volume, p_0 and $\frac{\mathrm{d}p_0}{\mathrm{d}t}$ are spatially invariant and the volume integral of the divergence of velocity is zero. We get:

$$\frac{\mathrm{d}p_0(t)}{\mathrm{d}t}=\frac{1}{\int_V\left(\frac{\gamma-1}{\gamma}-C_p\right)dV}\left[-\frac{1}{Re_\tau\ Pr}\int_V\frac{\partial}{\partial x_j}\left(\lambda\frac{\partial T}{\partial x_j}\right)dV+p_0(t)\int_V u_i\frac{\partial C_p}{\partial x_i}dV-\frac{Q}{Re_\tau\ Pr}\ V\right] \tag{A.2.8}$$

The volume integral of the divergence of heat flux can be transformed into a surface integral and we get:

$$\frac{\mathrm{d}p_0(t)}{\mathrm{d}t}=\frac{1}{\int_V\left(\frac{\gamma-1}{\gamma}-C_p\right)dV}\left[-\frac{1}{Re_\tau\ Pr}\int_S\lambda\frac{\partial T}{\partial x_j}dS_j+p_0(t)\int_V u_i\frac{\partial C_p}{\partial x_i}dV-\frac{Q}{Re_\tau\ Pr}\ V\right] \tag{A.2.9}$$

This is the most general form of the equation.

However, in the present simplification is made by assuming the fluid to be calorifically perfect. If $C_p=1$ and is constant, then the equation is simplified and we get:

$$\frac{\mathrm{d}p_0(t)}{\mathrm{d}t}=\frac{\gamma}{V}\frac{1}{Re_\tau\ Pr}\int_S\lambda\frac{\partial T}{\partial x_j}dS_j+\gamma\ \frac{Q}{Re_\tau\ Pr} \tag{A.2.10}$$

Using this in Eq.(A.2.7), we have:

$$\frac{\partial u_i}{\partial x_i}=\frac{1}{p_0(t)}\ \frac{1}{Re_\tau\ Pr}\left[\frac{\partial}{\partial x_j}\left(\lambda\frac{\partial T}{\partial x_j}\right)-\frac{1}{V}\int_S\lambda\frac{\partial T}{\partial x_j}dS_j\right] \tag{A.2.11}$$

For a closed system, the amount of mass in the system, M_0, is constant. This condition yields an equation to compute thermodynamic pressure at each instant. By integrating Eq.(A.2.4) over the volume, we get an expression for $p_0(t)$,

$$p_0(t) = \frac{M_0}{\int_V \frac{1}{T} dV}. \tag{A.2.12}$$

Appendix B

WENO Scheme

A WENO (Weighted Essentially Non-Oscillatory) scheme is a high-resolution, non-linear scheme employed when solving for quantities that have steep gradients. In the presence of sharp transitions, linear methods would require a very fine mesh as they cannot provide non-oscillatory solutions higher than first order. To obtain smoother and more accurate solutions, free of wiggles, and use relatively fewer grid points at the same time, we look towards high-resolution schemes. In the present work, we use a third-order WENO scheme for the discretization of the advection terms in the energy transport equation.

In this section, we will use a one-dimensional energy transport equation as an example, but the same procedure is applied in all three directions in the code. The one-dimensional energy transport equation can be written as:

$$\frac{\partial T}{\partial t} + u\frac{\partial T}{\partial x} = RHS. \tag{B.0.1}$$

The RHS includes the source and the heat diffusion terms. The temperature values are stored at the center of each control volume, so naturally, the gradients are calculated at the face centers. The WENO scheme is used to approximate the value of the temperature derivative ($\frac{\partial T}{\partial x}$) at the faces of the control volume so that we can compute the temperature value at the cell center for the new time step. The process of carrying out the approximation is discussed here.

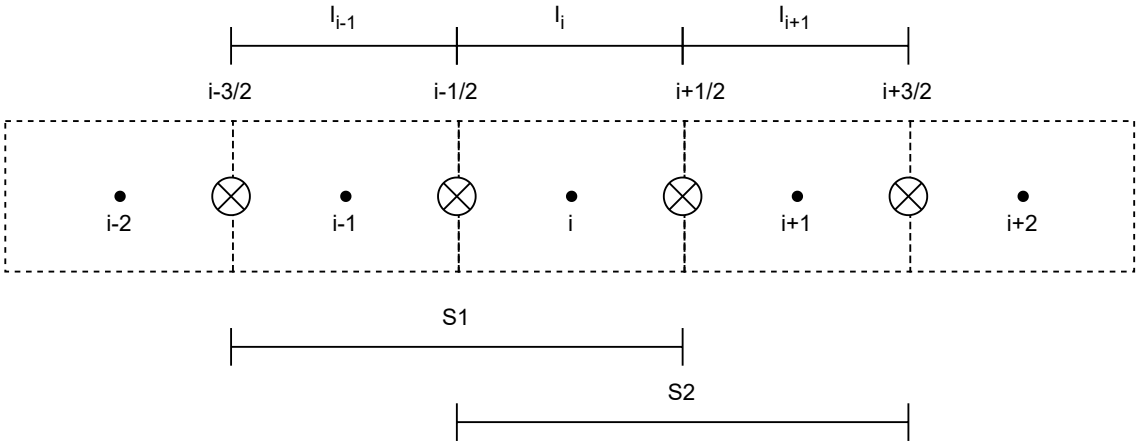

Figure B.1: Computational grid in the present work. .

The grid used in the present work is shown in Fig. B.1. The temperature values are stored at the cell centers indicated by dots and the velocity values are stored at the face centers marked

with $\otimes$. We can easily calculate temperature derivatives using first-order finite differences at the face centers. For example, at $x_{i-3/2}$, $\frac{\partial T}{\partial x} = (T_{i-1} - T_{i-2})/\Delta x$. Similarly, we can obtain accurate values for temperature derivatives at other face centers. With these values, the task is to now approximate the value for $\frac{\partial T}{\partial x}$ at x_i. For convenience, $\frac{\partial T}{\partial x}$ at x_i will be indicated as f_i in the rest of the section.

We have two stencils marked as S_1 and S_2. Each stencil has two sub-stencils, $S_1 = \{I_{i-1}, I_i\}$ and $S_2 = \{I_i, I_{i+1}\}$, with two points (where derivatives are known) in each sub-stencil. The choice of S_1 or S_2 depends on the direction of the flow at x_i. If the velocity, $u_i > 0$, then we choose S_1 as the derivative at x_i is influenced by the values to the left of it. And conversely, if $u_i < 0$, then we choose S_2.

Let's suppose $u_i > 0$. This implies we use the stencil S_1 that comprises two sub-stencils $S_1 = \{I_{i-1}, I_i\}$. We have 3 points where the derivative is known, $x_{i-3/2}$, $x_{i-1/2}$, $x_{i+1/2}$, and the value at x_i is to be approximated. In the third-order WENO scheme, the value is approximated using a first-order polynomial or a linear relation. The sub-stencil $I_{i-1} = \{x_{i-3/2},\ x_{i-1/2}\}$ (will be referred as sub-stencil 1) and $I_i = \{x_{i-1/2},\ x_{i+1/2}\}$ (will be referred as sub-stencil 2). The interpolated values at x_i using each sub-stencil is,

$$f_i^{(1)} = \frac{-f_{i-3/2} + 3f_{i-1/2}}{2}, \tag{B.0.2}$$

$$f_i^{(2)} = \frac{f_{i-1/2} + f_{i+1/2}}{2}. \tag{B.0.3}$$

The value f_i is approximated as a linear combination of the above two interpolated values and can be expressed as,

$$f_i = \sum_{k=1}^{2} \gamma_k f_i^{(k)}, \tag{B.0.4}$$

where γ_k are linear weights. For third order WENO scheme, $(\gamma_1, \gamma_2) = (1/3, 2/3)$. The linear weights are constants and indiscriminate to the oscillations. That is, there is no way to tell if there is a discontinuity in one of the sub-stencils and the interpolations are just weighed as per the linear weights.

To treat the discontinuities, the final approximation of f_i should be a combination of the interpolations weighted by the non-linear weights w_k. The nonlinear weights will be equal to the linear weights if the interpolations with both the sub-stencils are smooth. If there is a discontinuity in one of the sub-stencils, then the nonlinear weight for that would be close to 0, thus making the solution non-oscillatory. The choices for nonlinear weights presented in this section are given in Jiang and Shu (1996),

$$w_k = \frac{\tilde{w_k}}{\sum_{k=1}^{2} \tilde{w_k}}, \quad \tilde{w_k} = \frac{\gamma_k}{(\epsilon + \beta_k)^2}, \tag{B.0.5}$$

where $\epsilon = 10^{-6}$ is a small number added to avoid division by zero and β_k is the smoothness indicator. Large β_k implies that there exists a discontinuity in the sub-stencil, and would result in a nonlinear weight close to 0 for that sub-stencil. Conversely, low values of β_k correspond to smooth interpolation within the sub-stencil and thus assigning a higher weight to it for the approximation. The smoothness indicators for the third order scheme specifically are (Nunez, 2015),

$$\beta_1 = (f_{i-3/2} - f_{i-1/2})^2, \quad \beta_2 = (f_{i-1/2} - f_{i+1/2})^2. \tag{B.0.6}$$

The final approximation for f_i can be written as,

$$f_i = \sum_{k=1}^{2} w_k f_i^{(k)}. \tag{B.0.7}$$

Appendix C

Derivation of MKE and TKE Equations

Reynolds decomposition:

$$\gamma = \overline{\gamma} + \gamma'.$$

Favre decomposition:

$$\gamma = \tilde{\gamma} + \gamma'',$$

where,

$$\tilde{\gamma} = \frac{\overline{\rho\gamma}}{\overline{\gamma}} \quad \text{and} \quad \overline{\rho\gamma''} = 0.$$

Averaged governing equations: Velocity will be decomposed as Favre averaged velocity and the corresponding fluctuation,

$$u_i = \tilde{u_i} + u_i'',$$

while density will be decomposed in terms of a Reynolds average and fluctuation,

$$\rho = \overline{\rho} + \rho'.$$

Using these quantities in the governing equations and Reynolds averaging the whole equation would yield the final form of averaged equations.

Continuity equation:

$$\frac{\partial \overline{\rho}}{\partial t} + \frac{\partial \overline{\rho}\tilde{u_i}}{\partial x_i} = 0.$$

Momentum equation:

$$\overline{\rho}\frac{\partial \tilde{u_i}}{\partial t} + \overline{\rho}\tilde{u_j}\frac{\partial \tilde{u_i}}{\partial x_j} = -\frac{\partial \overline{p}}{\partial x_i} + \frac{\partial \overline{\tau_{ij}}}{\partial x_j} + \overline{\rho}g_i - \frac{\partial \overline{\rho u_i'' u_j''}}{\partial x_j},$$

where, $g_i = (0, 0, -g)$.

Kinetic energy of mean flow:

$$K = \frac{\tilde{u_i}\tilde{u_i}}{2}.$$

The mean kinetic energy equation is obtained by multiplying $\tilde{u_i}$ to the averaged form of momentum conservation equation,

$$\overline{\rho}\tilde{u_i}\frac{\partial \tilde{u_i}}{\partial t} + \overline{\rho}\tilde{u_i}\tilde{u_j}\frac{\partial \tilde{u_i}}{\partial x_j} = -\tilde{u_i}\frac{\partial \overline{p}}{\partial x_i} + \tilde{u_i}\frac{\partial \overline{\tau_{ij}}}{\partial x_j} + \tilde{u_i}\overline{\rho}g_i - \tilde{u_i}\frac{\partial \overline{\rho u_i'' u_j''}}{\partial x_j},$$

$$\overline{\rho}\frac{\partial K}{\partial t} + \overline{\rho}\tilde{u_j}\frac{\partial K}{\partial x_j} = -\tilde{u_i}\frac{\partial \overline{p}}{\partial x_i} + \frac{\partial \tilde{u_i}\overline{\tau_{ij}}}{\partial x_j} - \overline{\tau_{ij}\frac{\partial \tilde{u_i}}{\partial x_j}} + \tilde{u_i}\overline{\rho}g_i - \frac{\partial \tilde{u_i}\overline{\rho u_i'' u_j''}}{\partial x_j} + \overline{\rho u_i'' u_j''}\frac{\partial \tilde{u_i}}{\partial x_j},$$

$$\boxed{\overline{\rho}\frac{\partial K}{\partial t} + \overline{\rho}\tilde{u_j}\frac{\partial K}{\partial x_j} = -\tilde{u_i}\frac{\partial \overline{p}}{\partial x_i} + \frac{\partial}{\partial x_j}\left(\tilde{u_i}\overline{\tau_{ij}} - \tilde{u_i}\overline{\rho u_i'' u_j''}\right) + \tilde{u_i}\overline{\rho}g_i - \overline{\tau_{ij}\frac{\partial \tilde{u_i}}{\partial x_j}} + \overline{\rho u_i'' u_j''}\frac{\partial \tilde{u_i}}{\partial x_j}}.$$

Turbulent kinetic energy:

$$k = \frac{\overline{\rho u_i'' u_i''}}{2\overline{\rho}} = \frac{\widetilde{u_i'' u_i''}}{2}.$$

The turbulent kinetic energy equation is obtained by multiplying u_i'' to the momentum conservation equation and subsequently, Reynolds averaging the equation.

The momentum conservation equation,

$$\rho\frac{\partial u_i}{\partial t} + \rho u_j\frac{\partial u_i}{\partial x_j} = -\frac{\partial p}{\partial x_i} + \frac{\partial \tau_{ij}}{\partial x_j} + \rho g_i,$$

when multiplied with u_i'', we get,

$$\rho u_i''\frac{\partial u_i}{\partial t} + u_i''\ \rho u_j\frac{\partial u_i}{\partial x_j} = -u_i''\frac{\partial p}{\partial x_i} + u_i''\frac{\partial \tau_{ij}}{\partial x_j} + \rho u_i'' g_i.$$

Further, Favre decomposing the velocity, LHS can be rewritten as,

$$LHS : \rho u_i''\frac{\partial \tilde{u_i}}{\partial t} + \rho\frac{\partial}{\partial t}\left(\frac{u_i'' u_i''}{2}\right) + \rho u_j u_i''\frac{\partial \tilde{u_i}}{\partial x_j} + \rho u_j\frac{\partial}{\partial x_j}\left(\frac{u_i'' u_i''}{2}\right)$$

$$\implies \rho u_i''\frac{\partial \tilde{u_i}}{\partial t} + \frac{\partial}{\partial t}\left(\frac{\rho u_i'' u_i''}{2}\right) + \rho u_j u_i''\frac{\partial \tilde{u_i}}{\partial x_j} + \frac{\partial}{\partial x_j}\left(\frac{\rho u_j u_i'' u_i''}{2}\right) - \left(\frac{u_i'' u_i''}{2}\right)\cancel{\left[\frac{\partial \rho}{\partial t} + \frac{\partial \rho u_j}{\partial x_j}\right]}$$

$$\implies \rho u_i''\frac{\partial \tilde{u_i}}{\partial t} + \frac{\partial}{\partial t}\left(\frac{\rho u_i'' u_i''}{2}\right) + \rho u_i'\tilde{u_j}\frac{\partial \tilde{u_i}}{\partial x_j} + \rho\ u_j'' u_i''\frac{\partial \tilde{u_i}}{\partial x_j} + \frac{\partial}{\partial x_j}\left(\frac{\rho \tilde{u_j} u_i'' u_i''}{2}\right) + \frac{\partial}{\partial x_j}\left(\frac{\rho u_j'' u_i'' u_i''}{2}\right)$$

Now, applying Reynolds averaging to these terms and simplifying,

$$\cancel{\overline{\rho u_i''}\frac{\partial \tilde{u_i}}{\partial t}} + \frac{\partial}{\partial t}\left(\frac{\overline{\rho u_i'' u_i''}}{2}\right) + \cancel{\overline{\rho u_i''}\tilde{u_j}\frac{\partial \tilde{u_i}}{\partial x_j}} + \overline{\rho\ u_j'' u_i''}\frac{\partial \tilde{u_i}}{\partial x_j} + \frac{\partial}{\partial x_j}\left(\frac{\tilde{u_j}\ \overline{\rho u_i'' u_i''}}{2}\right) + \frac{\partial}{\partial x_j}\left(\frac{\overline{\rho u_j'' u_i'' u_i''}}{2}\right),$$

$$\implies LHS : \frac{\partial \overline{\rho}k}{\partial t} + \frac{\partial \overline{\rho}\tilde{u_j}k}{\partial x_j} + \overline{\rho\ u_j'' u_i''}\frac{\partial \tilde{u_i}}{\partial x_j} + \frac{\partial}{\partial x_j}\left(\frac{\overline{\rho u_j'' u_i'' u_i''}}{2}\right).$$

The turbulent kinetic energy can now be written as,

$$\frac{\partial \overline{\rho}k}{\partial t} + \frac{\partial \overline{\rho}\tilde{u_j}k}{\partial x_j} + \overline{\rho\ u_j'' u_i''}\frac{\partial \tilde{u_i}}{\partial x_j} + \frac{\partial}{\partial x_j}\left(\frac{\overline{\rho u_j'' u_i'' u_i''}}{2}\right) = -\overline{u_i''}\frac{\partial \overline{p}}{\partial x_i} - \frac{\partial \overline{u_i'' p'}}{\partial x_i} + \overline{p'\frac{\partial u_i''}{\partial x_i}} + \frac{\partial \overline{u_i''\tau_{ij}}}{\partial x_j} - \overline{\tau_{ij}\frac{\partial u_i''}{\partial x_j}} + \cancel{\overline{\rho u_i''}g_i}.$$

If we write in terms of production, transport and dissipation terms, it would look like,

$$\boxed{\frac{\partial \overline{\rho}k}{\partial t} + \frac{\partial \overline{\rho}\tilde{u_j}k}{\partial x_j} = -\overline{\rho\ u_j'' u_i''}\frac{\partial \tilde{u_i}}{\partial x_j} - \frac{\partial}{\partial x_j}\left[\frac{\overline{\rho u_j'' u_i'' u_i''}}{2} + \overline{u_j'' p'} - \overline{u_i''\tau_{ij}}\right] - \overline{u_i''}\frac{\partial \overline{p}}{\partial x_i} + \overline{p'\frac{\partial u_i''}{\partial x_i}} - \overline{\tau_{ij}\frac{\partial u_i''}{\partial x_j}}}.$$

Appendix D

Comparison of Case C with Cases A and B

In this section, the plots corresponding to $T_2/T_1 = 4$ are compared with cases A and B. At this temperature ratio, which is somewhat more severe, flows at $Ri_\tau = 0,\ 18$ were simulated. Due to limitations of time and resources, only these cases could be simulated, and are presented in the appendix as they were allowed to run for significantly less duration than the Cases A and B. However, the early results continue the trend observed in section 7.2.1. The mean profiles of velocity and temperature are shown in Fig. D.1. Normalization of velocity is done using the arithmetic mean of friction velocity, and temperature is normalized as $\theta = (T - T_1)/(T_2 - T_1)$. The variance of the velocity fluctuations scaled with the square of mean friction velocity and the semi-locally scaled variance are shown in Fig. D.2 and Fig. D.3 respectively. The RMS values of temperature fluctuations, normalized by the temperature difference between the walls, for Cases A, B and C are shown in Fig. D.4. Furthermore, turbulent momentum flux normalized with the semi-local friction velocity squared is compared in Fig. D.5 and turbulent heat flux normalized using product of semi-local friction velocity and friction temperature is presented in Fig. D.6b.

The trends observed in all the figures is recognizable as it is in line with our discussions in section 7.2.1. For the neutrally buoyant case, the turbulence at the hot wall seems to decrease progressively with increasing temperature ratios. This points to the fact that we can completely suppress turbulence on the hot side of the channel, even without buoyancy, if the temperature at the hot wall is significantly higher than the cold side. This cannot be predicted using the Boussinesq approximation. However, the process of weakening the turbulence is accelerated by the introduction of buoyancy. Furthermore, from our discussions on turbulent shear stress at the walls, we could have also predicted that the region of zero stress occurs further away from the hot wall at $T_2/T_1 = 4$ than for Case B, which can be confirmed from the figures.

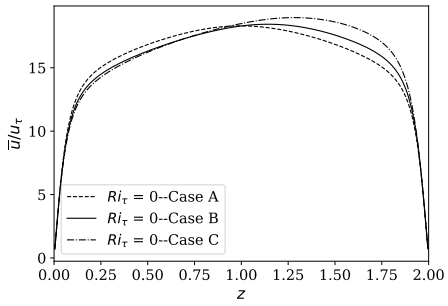

(a) Mean velocity profile for $Ri_\tau = 0$.

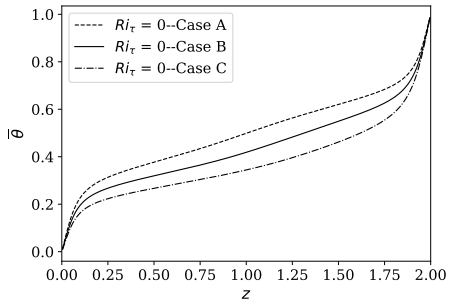

(b) Mean temperature profile for $Ri_\tau = 0$.

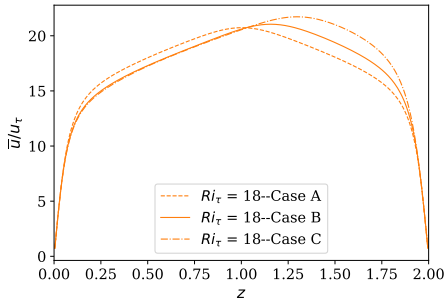

(c) Mean velocity profile for $Ri_\tau = 18$.

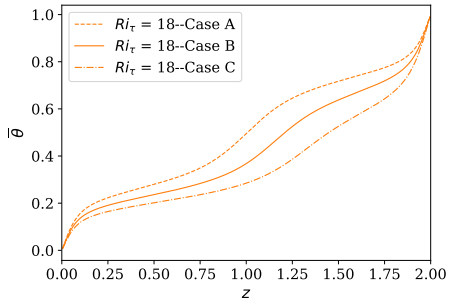

(d) Mean temperature profile for $Ri_\tau = 18$.

Figure D.1: Mean velocity and mean temperature profiles comparing Cases A, B and C. Mean velocity profile scaled with average friction velocity and mean temperature profile given in terms of θ, where $\theta = (T - T_1)/(T_2 - T_1)$. (a, c) compare the mean velocity profiles and (b, d) compare the mean temperature profiles for $Ri_\tau = 0, 18$ respectively.

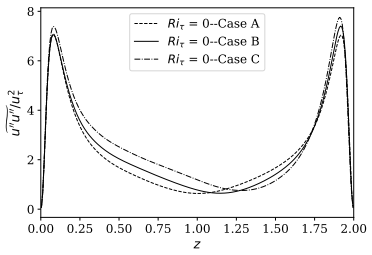

(a) $Ri_\tau = 0$.

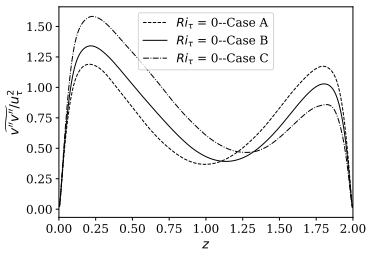

(b) $Ri_\tau = 0$.

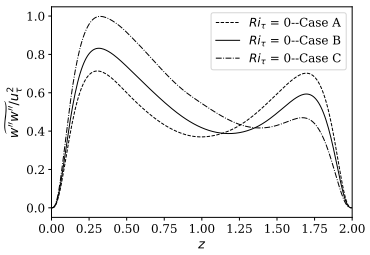

(c) $Ri_\tau = 0$.

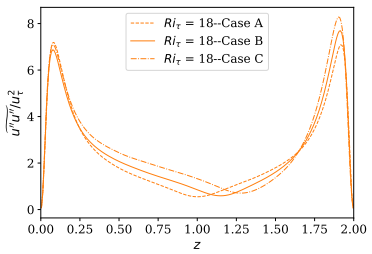

(d) $Ri_\tau = 18$.

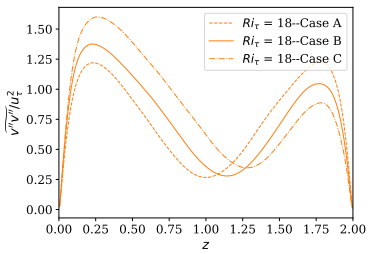

(e) $Ri_\tau = 18$.

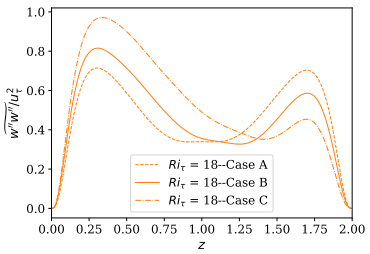

(f) $Ri_\tau = 18$.

Figure D.2: Variance of velocity fluctuations normalized with the square of the arithmetic mean of friction velocity for Cases A, B and C.(a, d) - streamwise velocity fluctuations, (b, e) - spanwise velocity fluctuations, (c, f) - wall-normal velocity fluctuations, for $Ri_\tau = 0,\ 18$ respectively.

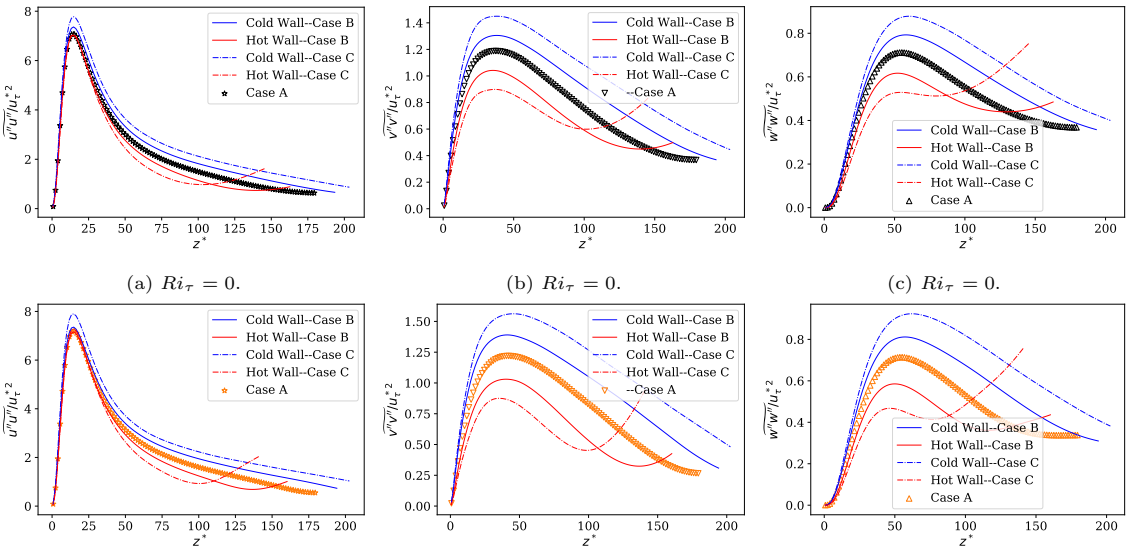

(a) $Ri_\tau = 0$. (b) $Ri_\tau = 0$. (c) $Ri_\tau = 0$.

(d) $Ri_\tau = 18$. (e) $Ri_\tau = 18$. (f) $Ri_\tau = 18$.

Figure D.3: Semi-locally scaled variance of velocity fluctuations comparing Cases A, B and C. Case A is indicated by symbols. For Case B and C, hot side (red lines) is scaled with respect to the hot wall and the cold side (blue lines) is scaled with respect to the cold wall. (a, d) - streamwise velocity fluctuations, (b, e) - spanwise velocity fluctuations, (c, f) - wall-normal velocity fluctuations, for $Ri_\tau = 0,\ 18$ respectively.

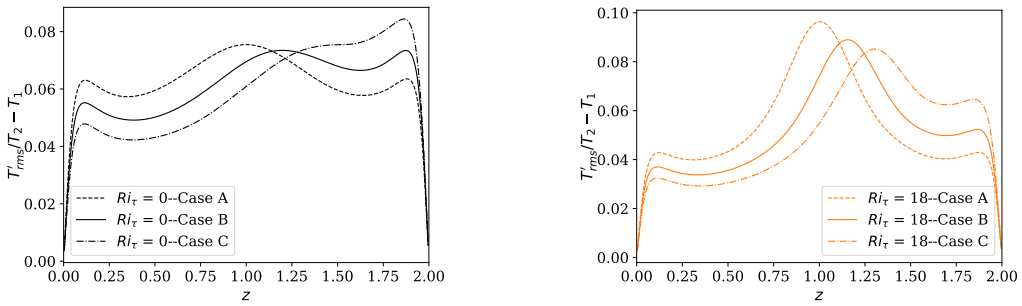

(a) $Ri_\tau = 0$. (b) $Ri_\tau = 18$.

Figure D.4: RMS of temperature fluctuation values comparing Cases A, B and C. The values are normalized with $T_2 - T_1$. (a) $Ri_\tau = 0$. (b) $Ri_\tau = 18$.

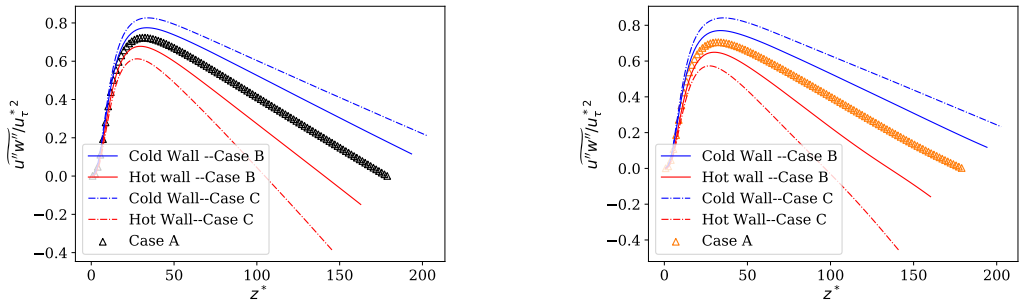

(a) $Ri_\tau = 0$. (b) $Ri_\tau = 18$.

Figure D.5: Variation of semi-locally scaled turbulent momentum flux. Symbols correspond to Case A. Lines (Red - Hot side, Blue - Cold side) correspond to Case B and C. (a) $Ri_\tau = 0$. (b) $Ri_\tau = 18$.

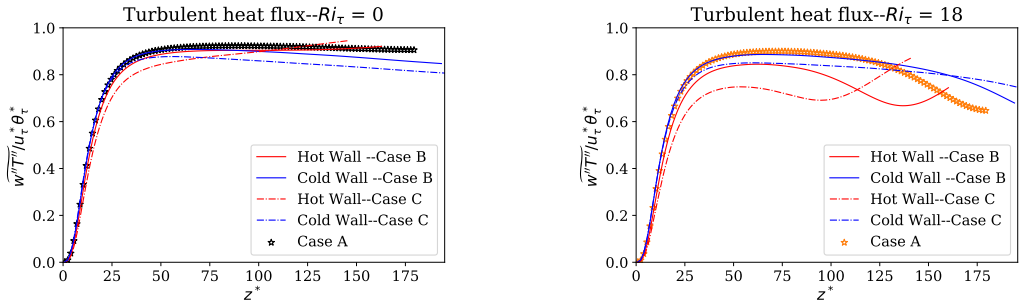

(a) $Ri_\tau = 0$.

(b) $Ri_\tau = 18$.

Figure D.6: Turbulent heat flux for different Richardson numbers. The markers correspond to the constant property Case A and lines to the variable property case (Cases B and C). Red lines correspond to the flux in the hot region and the blue lines to the cold region of variable property case. (a) $Ri_\tau = 0$. (b) $Ri_\tau = 18$.

Bibliography

V. Armenio and S. Sarkar. An investigation of stably stratified turbulent channel flow using large-eddy simulation. *Journal of fluid mechanics*, 459:1–42, 2002.

J. H. Bae, J. Y. Yoo, and H. Choi. Direct numerical simulation of turbulent supercritical flows with heat transfer. *Physics of fluids*, 17(10):105104, 2005.

J. H. Bae, J. Y. Yoo, and D. M. McEligot. Direct numerical simulation of heated co 2 flows at supercritical pressure in a vertical annulus at re= 8900. *Physics of Fluids*, 20(5):055108, 2008.

G. Brethouwer, Y. Duguet, and P. Schlatter. Turbulent–laminar coexistence in wall flows with coriolis, buoyancy or lorentz forces. *Journal of Fluid Mechanics*, 704:137–172, 2012.

X. Chu and E. Laurien. Flow stratification of supercritical co2 in a heated horizontal pipe. *The Journal of Supercritical Fluids*, 116:172–189, 2016. ISSN 0896-8446. doi: https://doi.org/10.1016/j.supflu.2016.05.003. URL https://www.sciencedirect.com/science/article/pii/S0896844616301048.

A. W. Cook and J. J. Riley. Direct numerical simulation of a turbulent reactive plume on a parallel computer. *Journal of Computational Physics*, 129(2):263–283, 1996. ISSN 0021-9991. doi: https://doi.org/10.1006/jcph.1996.0249. URL https://www.sciencedirect.com/science/article/pii/S0021999196902491.

P. Costa. A fft-based finite-difference solver for massively-parallel direct numerical simulations of turbulent flows. *Computers and Mathematics with Applications*, 76(8):1853–1862, 2018. ISSN 0898-1221. doi: https://doi.org/10.1016/j.camwa.2018.07.034. URL https://www.sciencedirect.com/science/article/pii/S089812211830405X.

A. Demou, C. Frantzis, and D. Grigoriadis. A low-mach methodology for efficient direct numerical simulations of variable property thermally driven flows. *International Journal of Heat and Mass Transfer*, 132:539–549, 2019. ISSN 0017-9310. doi: https://doi.org/10.1016/j.ijheatmasstransfer.2018.12.018. URL https://www.sciencedirect.com/science/article/pii/S0017931018338262.

E. Deusebio, C. Caulfield, and J. R. Taylor. The intermittency boundary in stratified plane couette flow. *Journal of Fluid Mechanics*, 781:298–329, 2015.

M. S. Dodd and A. Ferrante. A fast pressure-correction method for incompressible two-fluid flows. *Journal of Computational Physics*, 273:416–434, 2014. ISSN 0021-9991. doi: https://doi.org/10.1016/j.jcp.2014.05.024. URL https://www.sciencedirect.com/science/article/pii/S0021999114003702.

S. Dong and J. Shen. A time-stepping scheme involving constant coefficient matrices for phase-field simulations of two-phase incompressible flows with large density ratios. *Journal of Computational Physics*, 231(17):5788–5804, 2012.

V. Dostal, P. Hejzlar, and M. J. Driscoll. The supercritical carbon dioxide power cycle: Comparison to other advanced power cycles. *Nuclear Technology*, 154(3):283–301, 2006. doi: 10.13182/NT06-A3734. URL https://doi.org/10.13182/NT06-A3734.

O. Flores and J. Riley. Analysis of turbulence collapse in the stably stratified surface layer using direct numerical simulation. *Boundary-Layer Meteorology*, 139(2):241–259, 2011.

N. Franck. Numerical study of a channel flow with variable properties. 01 1998.

K. Gage and W. Reid. The stability of thermally stratified plane poiseuille flow. *Journal of Fluid Mechanics*, 33(1):21–32, 1968.

M. Garcia-Villalba and J. C. Del Alamo. Turbulence modification by stable stratification in channel flow. *Physics of Fluids*, 23(4):045104, 2011.

R. P. Garg, J. H. Ferziger, S. G. Monismith, and J. R. Koseff. Stably stratified turbulent channel flows. i. stratification regimes and turbulence suppression mechanism. *Physics of Fluids*, 12(10): 2569–2594, 2000.

T. Gerz and H. Yamazaki. Direct numerical simulation of buoyancy-driven turbulence in stably stratified fluid. *Journal of Fluid Mechanics*, 249:415–440, 1993.

T. Gerz, U. Schumann, and S. Elghobashi. Direct numerical simulation of stratified homogeneous turbulent shear flows. *Journal of Fluid Mechanics*, 200:563–594, 1989.

P. He. A high order finite difference solver for massively parallel simulations of stably stratified turbulent channel flows. *Computers & Fluids*, 127:161–173, 2016.

S. E. Holt, J. R. Koseff, and J. H. Ferziger. A numerical study of the evolution and structure of homogeneous stably stratified sheared turbulence. *Journal of Fluid Mechanics*, 237:499–539, 1992.

O. Iida, N. Kasagi, and Y. Nagano. Direct numerical simulation of turbulent channel flow under stable density stratification. *International journal of heat and mass transfer*, 45(8):1693–1703, 2002.

E. Itsweire, K. Helland, and C. Van Atta. The evolution of grid-generated turbulence in a stably stratified fluid. *Journal of Fluid Mechanics*, 162:299–338, 1986.

F. G. Jacobitz, S. Sarkar, and C. W. Van Atta. Direct numerical simulations of the turbulence evolution in a uniformly sheared and stably stratified flow. *Journal of Fluid Mechanics*, 342: 231–261, 1997.

G.-S. Jiang and C.-W. Shu. Efficient implementation of weighted eno schemes. *Journal of Computational Physics*, 126(1):202–228, 1996. ISSN 0021-9991. doi: https://doi.org/10.1006/jcph.1996.0130. URL `https://www.sciencedirect.com/science/article/pii/S0021999196901308`.

H.-J. Kaltenbach, T. Gerz, and U. Schumann. Large-eddy simulation of homogeneous turbulence and diffusion in stably stratified shear flow. *Journal of Fluid Mechanics*, 280:1–40, 1994.

B. Lessani and A. Zainali. Numerical investigation of stably stratified turbulent channel flow under non-boussinesq conditions. *Journal of turbulence*, (10):N8, 2009.

L. Mahrt. Stably stratified atmospheric boundary layers. *Annu. Rev. Fluid Mech*, 46(1):23–45, 2014.

A. Majda and J. Sethian. The derivation and numerical solution of the equations for zero mach number combustion. *Combustion Science and Technology*, 42(3-4):185–205, 1985. doi: 10.1080/00102208508960376. URL `https://doi.org/10.1080/00102208508960376`.

P. A. McMurtry, W.-H. Jou, J. Riley, and R. W. Metcalfe. Direct numerical simulations of a reacting mixing layer with chemical heat release. *AIAA Journal*, 24(6):962–970, 1986. doi: 10.2514/3.9371. URL `https://doi.org/10.2514/3.9371`.

O. Métais and J. R. Herring. Numerical simulations of freely evolving turbulence in stably stratified fluids. *Journal of Fluid Mechanics*, 202:117–148, 1989.

R. Moestam and L. Davidson. Numerical simulations of a thermocline in a pressure-driven flow between two infinite horizontal plates. *Physics of fluids*, 17(7):075109, 2005.

A. Monin and A. Obukhov. Basic laws of turbulent mixing in the surface layer of the atmosphere. pages 163–187, 1954.

H. N. Najm, P. S. Wyckoff, and O. M. Knio. A semi-implicit numerical scheme for reacting flow: I. stiff chemistry. *Journal of Computational Physics*, 143(2):381–402, 1998. ISSN 0021-9991. doi: https://doi.org/10.1006/jcph.1997.5856. URL `https://www.sciencedirect.com/science/article/pii/S0021999197958563`.

H. Nemati, A. Patel, B. J. Boersma, and R. Pecnik. Mean statistics of a heated turbulent pipe flow at supercritical pressure. *International Journal of Heat and Mass Transfer*, 83:741–752, 2015. ISSN 0017-9310. doi: https://doi.org/10.1016/j.ijheatmasstransfer.2014.12.039. URL `https://www.sciencedirect.com/science/article/pii/S0017931014011478`.

F. Nicoud. Conservative high-order finite-difference schemes for low-mach number flows. *Journal of Computational Physics*, 158(1):71–97, 2000.

F. Nieuwstadt. Direct numerical simulation of stable channel flow at large stability. *Boundary-layer meteorology*, 116(2):277–299, 2005.

J. Nunez. *High-Order Methods for Computational Astrophysics*. 10 2015. ISBN 9783843922937. doi: 10.18419/opus-3980.

R. V. Ozmidov. On the turbulent exchange in a stably stratified ocean. pages 853–860, 1965.

A. Patel, J. W. Peeters, B. J. Boersma, and R. Pecnik. Semi-local scaling and turbulence modulation in variable property turbulent channel flows. *Physics of Fluids*, 27(9):095101, 2015.

J. W. Peeters, R. Pecnik, M. Rohde, T. Van Der Hagen, and B. J. Boersma. Turbulence attenuation in simultaneously heated and cooled annular flows at supercritical pressure. *Journal of Fluid Mechanics*, 799:505–540, 2016.

S. S. Pitla, D. M. Robinson, E. A. Groll, and S. Ramadhyani. Heat transfer from supercritical carbon dioxide in tube flow: A critical review. *HVAC&R Research*, 4(3):281–301, 1998. doi: 10.1080/10789669.1998.10391405. URL `https://www.tandfonline.com/doi/abs/10.1080/10789669.1998.10391405`.

S. B. Pope. *Turbulent Flows*. Cambridge University Press, 2000.

J. J. Riley and S. M. DeBruynkops. Dynamics of turbulence strongly influenced by buoyancy. *Physics of Fluids*, 15(7):2047–2059, 2003.

J. Rohr, E. Itsweire, K. Helland, and C. Van Atta. Growth and decay of turbulence in a stably stratified shear flow. *Journal of Fluid Mechanics*, 195:77–111, 1988.

L. H. Shih, J. R. Koseff, J. H. Ferziger, and C. R. Rehmann. Scaling and parameterization of stratified homogeneous turbulent shear flow. *Journal of Fluid Mechanics*, 412:1–20, 2000.

C. Staquet and F. Godeferd. Statistical modelling and direct numerical simulations of decaying stably stratified turbulence. part 1. flow energetics. *Journal of Fluid Mechanics*, 360:295–340, 1998.

D. Stillinger, K. Helland, and C. Van Atta. Experiments on the transition of homogeneous turbulence to internal waves in a stratified fluid. *Journal of Fluid Mechanics*, 131:91–122, 1983.

N. Williamson, S. Armfield, M. Kirkpatrick, and S. Norris. Transition to stably stratified states in open channel flow with radiative surface heating. *Journal of Fluid Mechanics*, 766:528–555, 2015.

F. Zonta. Nusselt number and friction factor in thermally stratified turbulent channel flow under non-oberbeck–boussinesq conditions. *International journal of heat and fluid flow*, 44:489–494, 2013.

F. Zonta and A. Soldati. Stably stratified wall-bounded turbulence. *Applied Mechanics Reviews*, 70(4), 2018.

F. Zonta, C. Marchioli, and A. Soldati. Modulation of turbulence in forced convection by temperature-dependent viscosity. *Journal of Fluid Mechanics*, 697:150–174, 2012a.

F. Zonta, M. Onorato, and A. Soldati. Turbulence and internal waves in stably-stratified channel flow with temperature-dependent fluid properties. *Journal of fluid mechanics*, 697:175–203, 2012b.

F. Zonta, P. H. Sichani, and A. Soldati. Interaction between thermal stratification and turbulence in channel flow. *Journal of Fluid Mechanics*, 945:A3, 2022.